The influence of treatment with weak magnetic field pulses on the brittle–plastic transition temperature in zinc

O. I. Datsko and V. I. Alekseenko

Physicotechnical Institute, National Academy of Sciences of Ukraine, Donetsk

It is shown that the brittle–plastic transition temperature in zinc is reduced appreciably (in terms of internal friction and microhardness) as a result of magnetic treatment. © *1997 American Institute of Physics.* [S1063-7850(97)00502-8]

The problem of reducing the brittle–plastic transition temperature (T_p) is a key issue in the physics of strength and plasticity, and in physical metallurgy. This temperature can be reduced by altering the structure of the impurity-defect complexes by various methods such as alloying, heat treatment, and hydrostatic pressure. It is interesting to use treatment with weak magnetic field pulses for this purpose. The feasibility of this effect and the formulation of the problem are based on the following reasoning.

According to existing concepts,[1,2] the dislocation structure of brittle materials becomes highly mobile when the materials heated near T_p. It is hypothesized[3] that this effect is caused by a change in the nature of the interaction between dislocations and impurity atoms which are positioned at dislocations and block their movement. The feasibility of altering the structure of a material by suitable treatment has therefore attracted attention. It is assumed[4] that when materials in a nonequilibrium metastable state that contain crystal-structure defects exposed to a field, existing impurity-defect complexes are destroyed and new ones are formed, altering the physicomechanical properties of the material. It was shown in Ref. 5 that these impurity-defect complexes include dislocations interacting with impurity atoms. This reasoning suggests that treatment of materials possessing a brittle–plastic transition with a magnetic field may alter the nature of the interaction between the dislocations and the impurity atoms, and thus alter T_p.

We used a method of measuring the amplitude-dependent internal friction and the microhardness (H_v) since, as follows from Refs. 6 and 7, the low-frequency friction and the microhardness H_v are liable to change near T_p in polycrystalline zinc. Therefore the problem was to compare the temperature dependences of the friction and the microhardness H_v in the range 20–80 °C before and after treatment of the zinc.

The samples were rectangular parallelepipeds ($3 \times 3 \times 60$ mm) prepared by mechanical machining of a cast ingot. They had a coarse-grained structure with an average grain size of 200 μm. The samples were investigated both in their initial state and after annealing at 200 °C for 1.5 h.

The internal friction was measured with an inverted torsion pendulum (frequency around 1 Hz) at two different strain amplitudes, 4×10^{-5} and 9.2×10^{-5}, which caused the dislocations to become detached from their points of pinning. The material was heated at a rate of 0.5 and 1 K/min and the field treatment was carried out with a commercial OIMP-101 system. The microhardness was measured with a PMT-3 microhardness meter fitted with a special attachment for contact
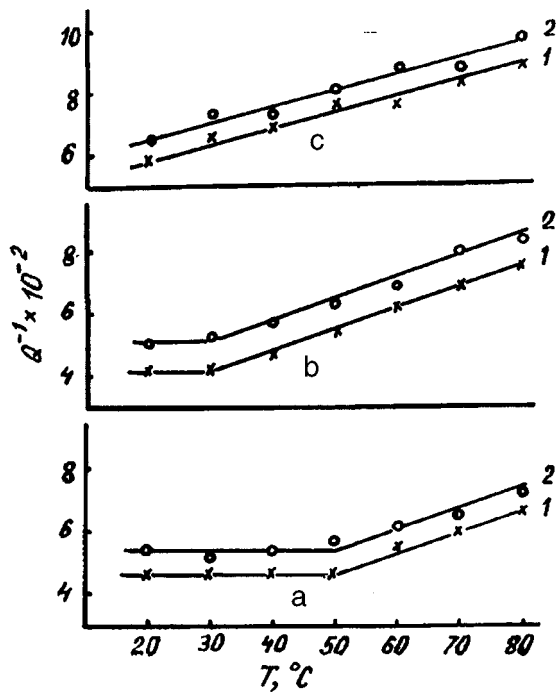

FIG. 1. Temperature dependence of the low-frequency internal friction of brittle polycrystalline zinc at two strain amplitudes: *1* — 4×10^{-5} and *2* — 9.2×10^{-5}; a — before exposure to the magnetic field, b — 24 h after exposure, and c — 5 days after exposure.
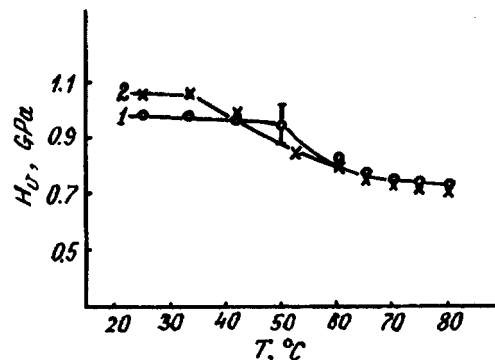

FIG. 2. Temperature dependence of the microhardness of brittle polycrystalline zinc: *1* — before exposure to the field and *2* — 24 h after exposure.

heating the sample. The components of the internal friction and OIMP-101 systems were integrated so that the heating, field treatment, and internal friction measurements could be performed without demounting the sample.

The results indicate that the temperature dependences of the internal friction and the microhardness H_v for the initial or annealed material exhibit a kink near 50 °C, which corresponds to the brittle–plastic transition (Figs. 1 and 2). This result completely agrees with the data presented in Refs. 6 and 7. After treatment it can be seen that the kink on the temperature curves of the internal friction and the microhardness H_v is shifted toward lower temperatures. With increasing time after the magnetic treatment, a further shift of the kink is observed. After 5 days, T_p tends toward room temperature.

It has therefore been found that when technical grade brittle polycrystalline zinc is treated with a pulsed magnetic field, the brittle–plastic transition temperature T_p may be reduced by several tens of degrees.

[1] A. A. Presnyakov, *Cold Brittleness* [in Russian], Nauka, Alma-Ata (1967).

[2] V. G. Bar'yakhtar and A. A. Galkin, Dokl. Akad. Nauk SSSR **227**, 1075 (1976) [Sov. Phys. Dokl. **21**, 194 (1976)].

[3] E. L. Savitskiĭ, K. B. Povarova, and P. V. Makarov, *Metallurgy of Tungsten* [in Russian], Metallurgiya, Moscow (1978), Chap. 4.

[4] S. N. Postnikov, V. P. Sidorov, A. V. Ilyakhinskiĭ *et al.*, *Applied Problems in the Strength and Plasticity, Statics and Dynamics of Deformable Systems* [in Russian], All-Union Inter-University Collection, Gorky University (1980), pp. 138–143.

[5] O. I. Datsko, V. I. Alekseenko, and A. D. Shakhova, Fiz. Tverd. Tela (St. Petersburg) **38**, 1799 (1996) [Phys. Solid State **38**, 992 (1996)].

[6] V. A. Beloshenko, O. I. Datsko, V. B. Primisler *et al.*, Zavod. Lab. **52**(2), 74 (1986).

[7] V. A. Beloshenko, O. I. Datsko, O. Kh. Melokhova *et al.*, Ukr. Fiz. Zh. **28**(1), 139 (1983).

Translated by R. M. Durham

Correlation between the phase composition of composite $YBa_2Cu_3O_{7-\delta}+x$MeO superconductors and their strength characteristics

A. T. Kozakov and S. I. Shevtsova

Scientific-Research Institute of Physics at the State University, Rostov-on-Don

Experimental results on the doping of $YBa_2Cu_3O_{7-\delta}$ superconducting ceramic with various metals (Ti, Zr, Ag, Hf, Ta, and W) are summarized. Some conclusions are drawn on the degree of chemical interaction between the metals and the main phase of the composite responsible for the superconducting properties of the material as a whole. An assessment is also made if the influence of doping on the strength characteristics, which vary in the composite as a result of different effects examined in this study. © *1997 American Institute of Physics.*
[S1063-7850(97)00602-2]

Enhanced brittleness and inferior strength properties are just some of the shortcomings restricting the use of high-temperature superconducting metal oxides as components in microelectronics and instrument manufacture. The strength characteristics of $YBa_2Cu_3O_{7-\delta}$ ceramic have been improved and its superconducting properties retained by doping with various metals.[1–4] In our previous studies[5–7] a correlation was reported between the strength properties of a $YBa_2Cu_3O_{7-\delta} + x$MeO system (Me = Zr, Hf, Ta) and the phase composition of Zr, Hf, and Ta.

The aim of the present paper is to classify various metals (Ti, Zr, Ag, Hf, Ta, and W) according to their positive and negative influence on the strength properties of $YBa_2Cu_3O_{7-\delta}$ ceramic using the experimental data, and to analyze the strengthening mechanisms.

Samples containing Ti and W were synthesized as described in Refs. 5–7 for Zr, Hf, and Ta, from a mixture of Y_2O_3, BaO, CuO, and MeO components at 970–980 °C for 12 h and were sintered under the same conditions in an oxygen atmosphere. Samples containing Ag were annealed from a mixture of powdered $YBa_2Cu_3O_{7-\delta}$ ceramic and Ag_2O at 900 °C for 24 h in air and in an O_2 atmosphere. When small amounts of the oxides TiO_2, ZrO_2, Ag_2O, HfO_2, Ta_2O_5, and WO_3 were added (on average $x < 10$–15 wt.%), the samples retained their superconducting properties.

The phase formation (by the phase we understand a spatial formation of uniform chemical composition[8]) was investigated with a Camebax-Micro microscope-microanalyzer using a statistical approach developed by us.[9] The average values of the microhardness were calculated for 30–50 impressions at a 100 g load. The measurement error was less than 10%.

Substitution in the main $YBa_2Cu_3O_{7-\delta}$ phase was only identified in Ag systems where approximately one copper atom in 20–30 was replaced by Ag and the remaining silver was concentrated in separate conglomerates with a low copper content (≈ 0.3 wt.%). The other added metals were detected, together with Y, Ba, and Cu, in spatial formations whose approximate composition regardless of x may be written for each system, respectively, as $YBa_3Ti_2O_{8.5}$, $Y_{0.05}Zr_{1.6}Ba_2Cu_{0.5}O_6$, $HfBaCuO_4$, $Ta_{0.5}Y_{0.5}Ba_2CuO_5$, and $Y_1B_{2.5}WCuO_{0.5}O_7$. (This notation is used for convenience: a spatially uniform formation, within the limits of the experiment $\cong 1\,\mu$m, may be either a chemical compound or an amorphous mixture). For all systems the volume fraction of the impurity phases CuO, Y_2BaCuO_5, $BaCuO_5$ (the latter was only observed in Hf-containing systems) and the phase containing the added metal tended to increase with increasing x. It is interesting to investigate the degree of stability of the main superconducting phase $YBa_2Cu_3O_{7-\delta}$ in interaction with the added metal oxides. The quantitative stability characteristic may be taken as the volume fraction of the main $YBa_2Cu_3O_{7-\delta}$ phase, which decreases with increasing x for all systems but at different rates (Fig. 1). For systems containing Ti and Ta, for example, it is predicted that the superconducting phase will be completely absent for $x \cong 10\%$ and in W-containing systems for $x \cong 20\%$. In all our samples of systems containing Hf, Zr, and Ag, the $YBa_2Cu_3O_{7-\delta}$ phase remains dominant, ensuring superconducting properties for fairly large x (Refs. 6 and 7). Thus, in terms of their degree of chemical interaction with the $YBa_2Cu_3O_{7-\delta}$ superconducting phase, the metals may be put in the order Ti > Ta > W > Hf > Zr > Ag.

For the series of $YBa_2Cu_3O_{7-\delta} + x$MeO composites studied, the strength characteristics are enhanced with increasing x (Fig. 2). This enhancement correlates with an increase in the volume fraction of the impurity phases [or a reduction in the volume of the superconducting phase (Fig. 1)] and also with their distribution over the microcrystallite boundaries of the main phase. An analysis of these data suggests that segregation of the phases containing the added metal and the CuO phase may be responsible for the enhanced strength. Several mechanisms responsible for strengthening ceramics may be considered. In the first,[10] which has been well developed for multicomponent metal systems, segregation at grain boundaries plays a major role in strengthening the material as a whole: the binding energy of the atoms per unit area determines the capacity of the segregating atoms to weaken or strength the grain boundaries. This mechanism may be investigated for the group IV metals Ti, Zr, and Hf. Since the binding energy density of these elements is higher than that of the Y, Ba, Cu, and O
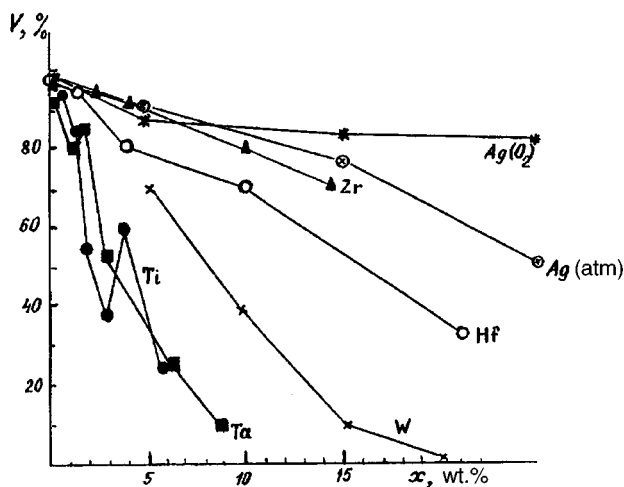
FIG. 1. Volume fraction of main $YBa_2Cu_3O_{7-\delta}$ phase in $YBa_2Cu_3O_{7-\delta}$ + xMeO composite versus degree of doping: MeO = TiO_2, ZrO_2, Ag_2O, HfO_2, Ta_2O_5, and WO_3. (The Ag composite was annealed in air and in O_2.)

atoms,[10] segregation of Ti, Zr, and Hf at grain boundaries of the main phase should enhance the strength characteristics of the ceramic. This strengthening mechanism is supported by the relative position of the strength curves for Ti, Zr, and Hf (Fig. 2), which correlates with the binding energy density: $[E(\text{Ti}) < E(\text{Zr}) < E(\text{Hf})]$.[10] This strengthening mechanism most likely predominates at low additive concentrations in $YBa_2Cu_3O_{7-\delta}$ + xMeO systems (Me = Ti, Hf) (no data are available for Zr or W in this range): the main increase in the strength characteristics is observed for small x when no large volumes of impurity phases are present.

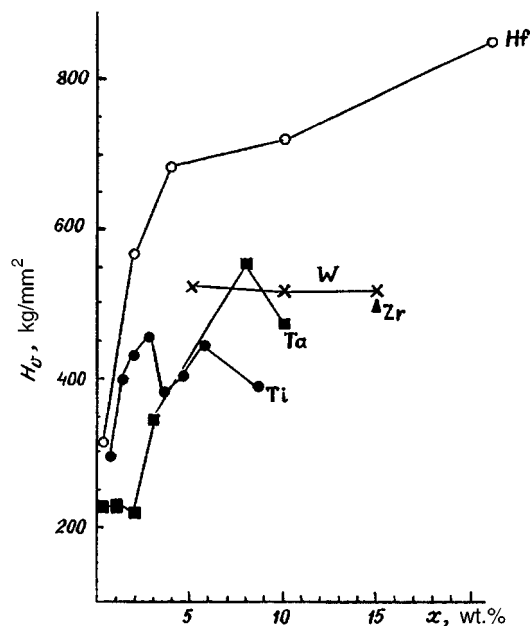Another strengthening mechanism, typical of multiphase systems and based on the properties of one of the phases to undergo structural changes under the action of local fields,[11,12] may well predominate for larger x. This results in the relaxation of local stresses near the stress concentrator and enhances the strength characteristics of the material. For this strengthening mechanism a correlation should be observed between H_v and the volume of one of the impurity phases. For example, an increase in H_v for Hf ($x \geq 4$ wt.%) is most likely caused by an increase in the volume fraction of the hafnium phase and the nonlinearity of $H_v = f(x)$ arises from a change in the distribution of the hafnium-containing phase[7] from a bulk to a grain-boundary distribution in the range $4 < x < 10$ wt.% (negligible increase in H_v) and back to a bulk distribution for $x > 10$ wt.%. A similar strengthening mechanism also applies to Ta ($x \geq 2$ wt.%) and may be caused by an increase in the volume of the tantalum and(or) CuO phases.[6]

CONCLUSIONS

Doping a $YBa_2Cu_3O_{7-\delta}$ superconductor with metals causes chemical decomposition. In terms of their chemical interaction with the superconducting phase (and resultant decrease in the fraction of this phase), the metals studied here may be placed in the following order: Ti > Ta > W > Hf > Zr > Ag.

The strength properties of the superconducting ceramic $YBa_2Cu_3O_{7-\delta}$ are enhanced by doping with HfO_2 (up to $\cong 20$ wt.%) and with TiO_2, Ta_2O_5, WO_3, and ZrO_2 (up to 10–15 wt.%). Different strengthening mechanisms may predominate in the composite depending on the degree of doping.

FIG. 2. Microhardness of $YBa_2Cu_3O_{7-\delta}$ + xMeO composite superconductor versus degree of doping. MeO = TiO_2, ZrO_2, Ag_2O, HfO_2, Ta_2O_5, and WO_3.

[1] R. Regnier, R. P. Gupta, and P. Truhot, J. Phys. C: Solid State Phys. **21**(14), 463 (1988).

[2] V. G. Bar'yakhtar, V. N. Varyukhin, and S. V. Strongin, Pis'ma Zh. Tekh. Fiz. **15**(5), 17 (1989) [Sov. Tech. Phys. Lett. **15**, 169 (1989)].

[3] V. G. Bar'yakhtar, V. N. Varyukhin, and S. V. Strongin, Dokl. Akad. Nauk Ukr. SSR Ser. A No. 3, 55 (1989).

[4] T. I. Panova, E. P. Savchenko, V. B. Glyshkova, A. V. Komarov, and É. S. Antroshchenko, Sverkhprovodimost' (KIAE) **5**, 914 (1992) [Superconductivity **5**, 919 (1992)].

[5] V. P. Varyukhin, A. T. Kozakov, V. A. Dem'yanchenko, and S. I. Shevtsova, Sverkhprovodimost' (KIAE) **2**(10), 26 (1989) [Superconductivity **2**(10), 30 (1989)].

[6] V. P. Varyukhin, A. T. Kozakov, S. I. Loboda, and V. A. Panasyuk, Dokl. Akad. Nauk Ukr. SSR Ser. Fiz.-Mat. Tekh. Nauki No. 4, 59 (1990)

[7] V. P. Varyukhin, A. T. Kozakov, S. I. Loboda, and V. A. Panasyuk, Pis'ma Zh. Tekh,. Fiz. **16**(11), 75 (1990) [Sov. Tech. Phys. Lett. **16**, 434 (1990)].

[8] L. O. Chernyavskiĭ, A. Ya. Royak, and L. N. Mazalov, Izv. SO Akad. Nauk SSSR Ser. Khim. **4**(12), 35 (1987).

[9] S. I. Shevtsova and A. T. Kozakov, Zavod. Lab. No. 9, 17 (1992).

[10] *Practical Surface Analysis: by Auger and X Ray Photoelectron Spectroscopy*, edited by D. Briggs and M.P. Seah (Wiley, New York, 1983) [MIR, Moscow, 1987]

[11] A. A. Bul'bich, Metallofizika **9**(4), 88 (1987).

[12] I. A. Bendelitin, S. V. Popova, and P. F. Vereshchagin, Geokhimiya, No. 6, 677 (1967).

Translated by R. M. Durham

Polarization recording of holograms in partially polarized recording light

B. N. Kilosanidze

Institute of Cybernetics, Academy of Sciences, Tbilisi, Georgia

A theoretical approach is considered for media whose scalar and anisotropic responses are of opposite sign. The nondiffracted beam, and the imaginary and real images formed by a polarization hologram are analyzed under these conditions. It is shown that the imaginary image has its polarization transformed compared with the object field while a pseudoscopic object field reconstructed in terms of polarization state and degree is formed in the real image. © *1997 American Institute of Physics.* [S1063-7850(97)00702-7]

The polarization-holographic recording and reconstruction of an object field by partially polarized light has been investigated using a modification described in Refs. 1–3 of the Jones vector matrix method[4,5] and the law governing the Weigert effect[6]. It has been shown that when polarization-sensitive media whose characteristics obey the conditions $\hat{s} - \hat{v}_L = 0$, $\hat{s} + \hat{v}_L \neq 0$, $\hat{v}_L - \hat{v}_G \neq 0$, $\hat{v}_L + \hat{v}_G = 0$ are used for recording, where $\hat{s}$, $\hat{v}_L$, and $\hat{v}_G$ are, respectively, the so-called scalar, anisotropic, and gyrotropic responses of the medium to the intensity of the polarized light, the partial polarization state of the object field may be reconstructed in the imaginary image. Media having these characteristics have been used in a polarization holography experiment.[1]

In the present paper we analyze polarization holographic recording in partially polarized light in a recording medium whose characteristics satisfy conditions differing from those considered above:

$$\hat{s} - \hat{v}_L \neq 0, \quad \hat{s} + \hat{v}_L \neq 0, \quad \hat{v}_L - \hat{v}_G \neq 0, \quad \hat{v}_L + \hat{v}_G = 0. \quad (1)$$

Let us consider a polarization hologram recorded by a partially elliptically polarized reference wave propagating along the z axis and an object wave formed by propagation of the reference wave through an arbitrary (anisotropic-gyrotropic) object. The modified Jones vector of the sum wave may be expressed in the form:[2]

$$\mathbf{E}_\Sigma = \mathbf{E}_{\text{ref}} + \mathbf{E}_{\text{ob}} = E_{AX}\exp i(\omega t + \varphi)[1 + \exp i\delta \cdot M_{\text{ob}}]\begin{pmatrix} 1 \\ i\varepsilon \end{pmatrix}$$

$$\oplus E_{BY}\exp i\left(\omega t + \psi - \frac{\pi}{2}\right)[1 + \exp i\delta \cdot M_{\text{ob}}]\begin{pmatrix} i\varepsilon \\ 1 \end{pmatrix}, \quad (2)$$

where $\varepsilon = E_{AY}/E_{AX} = E_{BX}/E_{BY}\,(0 \leqslant \varepsilon \leqslant 1)$, $\oplus$ denotes the incoherent summation of amplitudes using the rules put forward in Ref. 2, $E_{AX}\exp i\varphi$ is the complex amplitude of the component of one basis, and $E_{BY}\exp i\psi$ is the complex amplitude of the component of the other basis, orthogonal and incoherent to it,

$$M_{\text{ob}} = \begin{pmatrix} \hat{m}_{11}\hat{m}_{12} \\ \hat{m}_{21}\hat{m}_{22} \end{pmatrix}$$

is the complex Jones matrix of the object, and δ is the phase shift induced by the oblique propagation of the object wave.

Under the action of the field of the partially elliptically polarized sum wave (2), anisotropy and gyrotropy described by the Jones matrix[7] are induced in the recording medium

$$M \approx M_0 + M_{-1} + M_{+1}, \quad (3)$$

where

$$M_0 \approx \exp - 2i\varkappa d\hat{n}_0 \begin{pmatrix} (M_0)_{11} & (M_0)_{12} \\ (M_0)_{21} & (M_0)_{22} \end{pmatrix}, \quad (4)$$

$$(M_0)_{11,22} = 1 - \frac{i\varkappa d}{2\hat{n}_0}[(\hat{s} \pm \hat{v}_L)(E_{AX}^2 + \varepsilon^2 E_{BY}^2)$$
$$+ (\hat{s} \mp \hat{v}_L)(\varepsilon^2 E_{AX}^2 + E_{BY}^2)],$$

$$(M_0)_{12,21} = -\frac{i\varkappa d}{2\hat{n}_0}\{2i\varepsilon[(\hat{v}_L \pm \hat{v}_G)E_{AX}^2$$
$$+ (\hat{v}_L \mp \hat{v}_G)E_{BY}^2]\}; \quad (5)$$

$$M_{-1} \approx -\frac{i\varkappa d}{2\hat{n}_0}\exp - 2i\varkappa d\hat{n}_0$$
$$\times \exp i\delta \begin{pmatrix} (M_{-1})_{11} & (M_{-1})_{12} \\ (M_{-1})_{21} & (M_{-1})_{22} \end{pmatrix}, \quad (5)$$

$$(M_{-1})_{11,22} = (\hat{s} \pm \hat{v}_L)[(E_{AX}^2 + \varepsilon^2 E_{BY}^2)\hat{m}_{11}$$
$$+ i\varepsilon(E_{AX}^2 - E_{BY}^2)\hat{m}_{12}] + (\hat{s} \mp \hat{v}_L)$$
$$\times [-i\varepsilon(E_{AX}^2 - E_{BY}^2)\hat{m}_{21} + (\varepsilon^2 E_{AX}^2 + E_{BY}^2)\hat{m}_{22}],$$

$$(M_{-1})_{12,21} = (\hat{v}_L \mp \hat{v}_G)[-i\varepsilon(E_{AX}^2 - E_{BY}^2)\hat{m}_{11}$$
$$+ (\varepsilon^2 E_{AX}^2 + E_{BY}^2)\hat{m}_{12}] + \hat{v}_L \pm \hat{v}_G$$
$$\times [(E_{AX}^2 + \varepsilon^2 E_{BY}^2)\hat{m}_{21} + i\varepsilon(E_{AX}^2 - E_{BY}^2)\hat{m}_{22}];$$

$$M_{+1} \approx -\frac{i\varkappa d}{2\hat{n}_0}\exp - 2i\varkappa d\hat{n}_0 \cdot \exp$$
$$- i\delta \begin{pmatrix} (M_{+1})_{11} & (M_{+1})_{12} \\ (M_{+1})_{21} & (M_{+1})_{22} \end{pmatrix}, \quad (6)$$

$$(M_{+1})_{11,22} = (\hat{s} \pm \hat{v}_L)[(E_{AX}^2 + \varepsilon^2 E_{BY}^2)\hat{m}_{11}^*$$
$$- i\varepsilon(E_{AX}^2 - E_{BY}^2)\hat{m}_{12}^*] + (\hat{s} \mp \hat{v}_L)$$
$$\times [i\varepsilon(E_{AX}^2 - E_{BY}^2)\hat{m}_{21}^* + (\varepsilon^2 E_{AX}^2 + E_{BY}^2)\hat{m}_{22}^*],$$

$$(M_{+1})_{12,21} = (\hat{v}_L \pm \hat{v}_G)[i\varepsilon(E_{AX}^2 - E_{BY}^2)\hat{m}_{11}^*$$
$$+ (\varepsilon^2 E_{AX}^2 + E_{BY}^2)\hat{m}_{12}^*] + (\hat{v}_L \mp \hat{v}_G)$$
$$\times [(E_{AX}^2 + \varepsilon^2 E_{BY}^2)\hat{m}_{21}^* - i\varepsilon(E_{AX}^2 - E_{BY}^2)\hat{m}_{22}^*].$$

Here the matrix M_0 is responsible for the formation of the nondiffracted beam, while the matrices M_{-1} and M_{+1} are responsible for the formation of the imaginary and real images, respectively. (The matrix responsible for the formation of the convolution component is not considered here.) In Eqs. (4)–(6) we have $\varkappa = (2\pi/\lambda)$, d is the thickness of the recording medium, and $\hat{n}_0$ is the complex refractive index in the initial unilluminated state ($\hat{n}_0 = n_0 - in_0\tau_0$, n_0 is the refractive index, and τ_0 is the extinction coefficient).

Using condition (1) we obtain in expressions (4)–(6):

$$M_0 \approx \exp(-2i\varkappa d\hat{n}_0)\left[\begin{pmatrix} 1 & 0 \\ 0 & 1 \end{pmatrix} + \frac{i\varkappa d\hat{v}_L}{\hat{n}_0}P_0\right]; \tag{7}$$

$$M_{-1} \approx \frac{i\varkappa d\hat{v}_L}{\hat{n}_0}\exp(-2i\varkappa d\hat{n}_0)\exp i\delta \cdot P(ad_j M_{ob}); \tag{8}$$

$$M_{+1} \approx \frac{i\varkappa d\hat{v}_L}{\hat{n}_0}\exp(-2i\varkappa d\hat{n}_0)\exp(-i\delta)(ad_j M_{ob}^*)P, \tag{9}$$

where

$$P_0 = \begin{pmatrix} \varepsilon^2 E_{AX}^2 + E_{BY}^2 & -2i\varepsilon E_{BY}^2 \\ -2i\varepsilon E_{AX}^2 & E_{AX}^2 + \varepsilon^2 E_{BY}^2 \end{pmatrix},$$

$$P = \begin{pmatrix} \varepsilon^2 E_{AX}^2 + E_{BY}^2 & i\varepsilon(E_{AX}^2 - E_{BY}^2) \\ -i\varepsilon(E_{AX}^2 - E_{BY}^2) & E_{AX}^2 + \varepsilon^2 E_{BY}^2 \end{pmatrix};$$

$$(ad_j)M_{ob} = \begin{pmatrix} \hat{m}_{22} & -\hat{m}_{21} \\ -\hat{m}_{12} & \hat{m}_{11} \end{pmatrix} \text{ and }$$

$$(ad_j)M_{ob}^* = \begin{pmatrix} \hat{m}_{22}^* & -\hat{m}_{21}^* \\ -\hat{m}_{12}^* & \hat{m}_{11}^* \end{pmatrix}$$

are the so-called adjoint and adjoint-conjugate matrices of the object, respectively.[8]

In the image reconstruction process, the polarization hologram is illuminated by a reconstructing wave identical to the reference wave. The nondiffracted wave is then given by

$$\mathbf{E}_0 = M_0 \mathbf{E}_{ref} \approx \exp(-2i\varkappa d\hat{n}_0)$$
$$\times \left\{ E_{AX}\exp i(\omega t + \varphi)\left[\begin{pmatrix} 1 & 0 \\ 0 & 1 \end{pmatrix} + \frac{i\varkappa d\hat{v}_L}{\hat{n}_0}P_0\right]\begin{pmatrix} 1 \\ i\varepsilon \end{pmatrix} \right.$$
$$\left. \oplus E_{BY}\exp i\left(\omega t + \psi - \frac{\pi}{2}\right)\left[\begin{pmatrix} 1 & 0 \\ 0 & 1 \end{pmatrix} + \frac{i\varkappa d\hat{v}_L}{\hat{n}_0}P_0\right]\begin{pmatrix} i\varepsilon \\ 1 \end{pmatrix}\right\}. \tag{10}$$

For the imaginary and real images formed by the polarization hologram we obtain respectively

$$\mathbf{E}_{-1} = M_{-1}\mathbf{E}_{ref} \approx \frac{i\varkappa d\hat{v}_L}{\hat{n}_0}\exp(-2i\varkappa d\hat{n}_0)$$
$$\times \left\{ E_{AX}\exp i(\omega t + \varphi + \delta)P(ad_j M_{ob})\begin{pmatrix} 1 \\ i\varepsilon \end{pmatrix} \right.$$
$$\left. \oplus E_{BY}\exp i\left(\omega t + \psi - \frac{\pi}{2} + \delta\right)P(ad_j M_{ob})\begin{pmatrix} i\varepsilon \\ 1 \end{pmatrix}\right\}, \tag{11}$$

$$\mathbf{E}_{+1} = M_{+1}\mathbf{E}_{ref} \approx \frac{i\varkappa d\hat{v}_L}{\hat{n}_0}\exp(-2i\varkappa d\hat{n}_0)(1 + \varepsilon^2)$$
$$\times \left\{ E_{AX}E_{BY}^2\exp i(\omega t + \varphi - \delta)(ad_j M_{ob}^*)\begin{pmatrix} 1 \\ i\varepsilon \end{pmatrix} \right.$$
$$\left. \oplus E_{BY}E_{AX}^2\exp i\left(\omega t + \psi - \frac{\pi}{2} - \delta\right)(ad_j M_{ob}^*)\begin{pmatrix} i\varepsilon \\ 1 \end{pmatrix}\right\}. \tag{12}$$

It follows from Eq. (10) that the nondiffracted beam contains no information regarding the object. An analysis of Eq. (11) reveals that in the imaginary image the object field has its polarization irreversibly transformed. It is deduced from Eq. (12) however, that a pseudoscopic object field with its polarization state reconstructed is formed in the real image.

In conclusion, we note that this result may be used to develop novel polarization devices.

[1] Sh. D. Kakichashvili, *Polarization Holography* [in Russian], Leningrad (1989).
[2] Sh. D. Kakichashvili, Zh. Tekh. Fiz. **65**(7), 200 (1995) [Tech. Phys. **40**, 743 (1995)].
[3] Sh. D. Kakichashvili and B. N. Kilosanidze, Pis'ma Zh. Tekh. Fiz. **21**(23), 6 (1995) [Tech. Phys. Lett. **21**, 951 (1995)].
[4] R. C. Jones, J. Opt. Soc. Am. **31**, 488 (1941).
[5] H. Hurwits, Jr. and R. C. Jones, J. Opt. Soc. Am. **31**, 493 (1941).
[6] F. Weigert, Verhandl. Deutschen Physik. Ges. **21**, 479 (1919).
[7] Sh. D. Kakichashvili, Zh. Tekh. Fiz. **59**(2), 26 (1989) [Sov. Phys. Tech. Phys. **34**, 145 (1989)].
[8] V. V. Voevodin and Yu. A. Kuznetsov, *Matrices and Calculations* [in Russian], Moscow (1984).

Translated by R. M. Durham

Mixing of granular materials in a half-filled rotating drum

S. N. Dorogovtsev

A. F. Ioffe Physicotechnical Institute, St. Petersburg

The process of avalanche mixing of two fractions of granular material in a half-filled rotating drum is described accurately and it is shown that under these conditions, the fractions do not generally undergo complete mixing. © *1997 American Institute of Physics.*
[S1063-7850(97)00802-1]

Interspersion of granular materials in a rotating drum (the longitudinal axis of the cylinder is horizontal and the drum is not completely filled so that there is free space at the top) has recently been investigated intensively (see Refs. 1–4, for instance). The reason for this interest is the obvious correlation with problems involving the dispersal of a pile of sand[5] and the problem of self-organized criticality.[6–8]

A configuration suitable in principle for investigating analytically (see Ref. 9) the very complex problem of the mixing of fractions of granular material in a rotating drum was proposed in an experimental study[4] and this system will be considered here.

Our drum is planar so that it is more like a disk. There is thus no need to allow for mixing of granules along the axis of rotation of the drum. The gravitational field is directed perpendicular to the axis of rotation. The drum rotates adiabatically slowly and at each point in time the free surface is at the angle of repose to the horizontal (Fig. 1). (It follows from Ref. 4 that the free surface may be considered to be planar in this case.)

Let us recall exactly what avalanche mixing of granular materials is. Let us assume that granules (whose sizes are much smaller than the radius of the drum) can only become interspersed on reaching the free surface of the material as the drum rotates. Granules not reaching the free surface simply rotate with the drum, without being shifted relative to each other (Fig. 1). Thus the material is only mixed in avalanches which descend continuously from the free surface as the drum rotates. This mixing has been described as avalanche mixing[4] although in our view, it would be more accurate to call it mixing in avalanches.

It is assumed that the granules of different fractions only differ in color. Since the granules are small, we can introduce the concept of a concentration of a particular fraction at a given point in the drum. Thus the state of each separate point **x** of the material at a particular time t is described by $\rho(\mathbf{x},t)$, which is the concentration of the black fraction. For a pure black fraction we have $\rho=1$ and for a pure white fraction $\rho=0$. We assume that at zero time the white fraction is at the bottom and the black fraction at the top. It will be convenient to introduce the notation shown in Fig. 2a. We shall describe the volume of the black fraction by the subtended angle $\chi \leq \pi/2$. In this case, the relative proportion of the black fraction in the material is $[2\chi+\sin(2\chi)]/\pi$.

The answers do not contain either the angle of repose of the granular material or the drum radius. On the diagrams

showing the distribution of the fractions it is therefore convenient to map the free surface to the horizontal (Fig. 2) and assume that the drum radius is unity. The answers also do not depend on the speed of rotation of the drum so that we shall take the ''time'' t to imply the complete angle of rotation of the drum. To be specific, we shall assume that the drum rotates counterclockwise.

We show that when the drum is half-filled, mixing of the material only at the free surface does not result in complete mixing in the system. Let a pure fraction be located at *all points* on a certain radius vector of the drum. At the instant when this radius vector reaches the surface, the material pours onto the left half of the surface and the same pure fraction is again found in all its points! (Since the drum rotates adiabatically slowly, it may be assumed that the granules intersperse instantaneously at the free surface.) Then the entire radius vector with the pure fraction rotates with the drum until it again reaches the right half of the free surface. The entire process is then repeated with the period π, which is half the period of rotation of the drum.

Thus at any one time on a certain radius vector of the drum there must be a pure fraction which never disappears. In Fig. 2, which shows various distribution patterns of the fractions at successive moments in time, it is easy to see that the pure white fraction disappears at time $t=\pi-\chi$. Thus the above reasoning must apply to the black fraction.

The position of the radius vector may be defined by its angle of inclination from the right half of the free surface, i.e., the angle ψ. Figure 2 shows that on the left half of the free surface it will be found that

$$\rho(\psi=0, 0 \leq t \leq \chi) = \rho(\psi=0, \pi-\chi \leq t \leq \pi) = 1. \tag{1}$$

This pattern is repeated with the period π: $\rho(0,t+\pi)=\rho(0,t)$. Since no mixing takes place in the bulk of the material, the entire distribution of the fractions in the drum can easily be found from the known distribution of the concentration of the black fraction on the left half of the free surface. In particular, if the concentration is $\rho=$const along the radii (it is then meaningful to introduce $\rho(\psi,t)$), for $0 \leq \psi \leq \pi$ and $t \geq \psi$ we have

$$\rho(\psi,t) = \rho(0, t-\psi). \tag{2}$$

We must now make a very strong assumption. We shall assume that the material in the avalanches is mixed completely (Fig. 1: if this assumption is satisfied, after intersper-
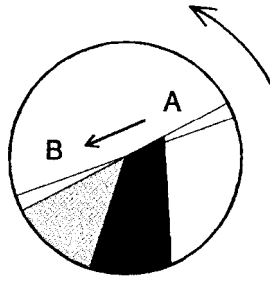
FIG. 1. Diagram showing avalanche mixing in a half-filled drum. When the rotation of the drum is infinitely small, granules of different fractions from sector *A* undergo mixing and pour into sector *B*. If the granules are in the bulk of the material, they rotate with the drum, without being shifted relative to each other. Regions of mixed material are shown by the gray color (here and in Fig. 2 the degree of mixing is not shown).
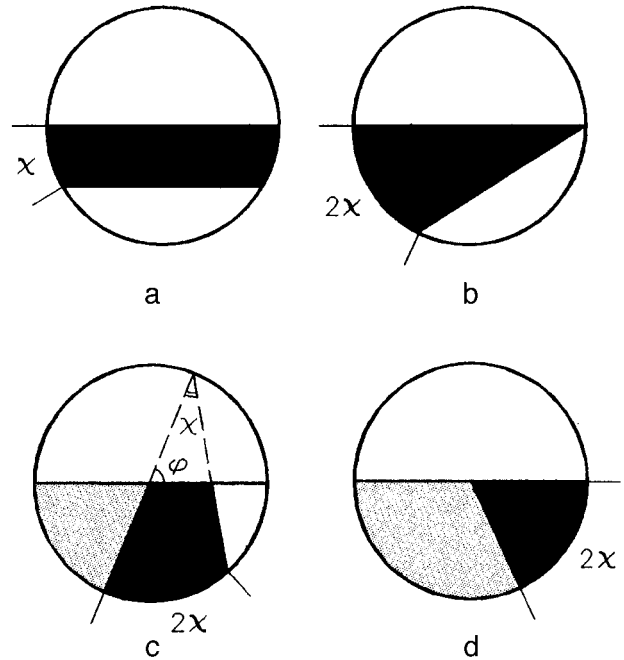

FIG. 2. Distribution of fractions in drum at various times. For convenience the friction angle is assumed to be zero and the free surface of the material is horizontal. *a* — position of fractions at zero time $t=0$. The angle characterizes the relative volume of the black fraction in the drum; *b* — $t=\chi$; *c* — $\chi<t<\pi-\chi$, $\varphi=t-\chi$; *d* — instant when pure white fraction disappears $t=\pi-\chi$.

sion the concentration ρ will be the same at all points in sector *B*). This assumption is logically taken as an initial approximation without going into details on the granule structure (such as agglomeration and sticking). In fact computer modeling[4] based on this assumption describes real experiments surprisingly accurately. It is then easy to see that after the time $t=\pi-\chi$ the concentration ρ is the same at all points on each individual radius vector. Thus after this time, the distribution $\rho(\psi,t)$ completely describes the state of the system.

We shall now find $\rho(0,t)$ for the interval $\chi\leqslant t\leqslant\pi-\chi$. Glancing at Fig. 2b, it is easy to understand that in this range

$$\frac{1}{2}\rho(0,t)=\frac{\partial S(t-\chi)}{\partial t}. \tag{3}$$

Here $S(\varphi)$ is the area of the triangle shown by the dashed line in Fig. 2c ($\varphi=t-\chi$) and the coefficient 1/2 appears on the left-hand side of this relation since the radius vector sweeps the area $\delta t/2$ when rotated through the small angle

δt. Standard formulas for the areas of triangles give $S(\varphi)=\frac{1}{2}\sin\varphi\sin\chi/\sin(\varphi+\chi)$. As a result we have

$$\rho(0,t)=\sin^2\chi/\sin^2 t. \tag{4}$$

Relations (1) and (4) together with the periodicity condition determine the complete behavior of the curve $\rho(0,t)$ (Fig. 3).
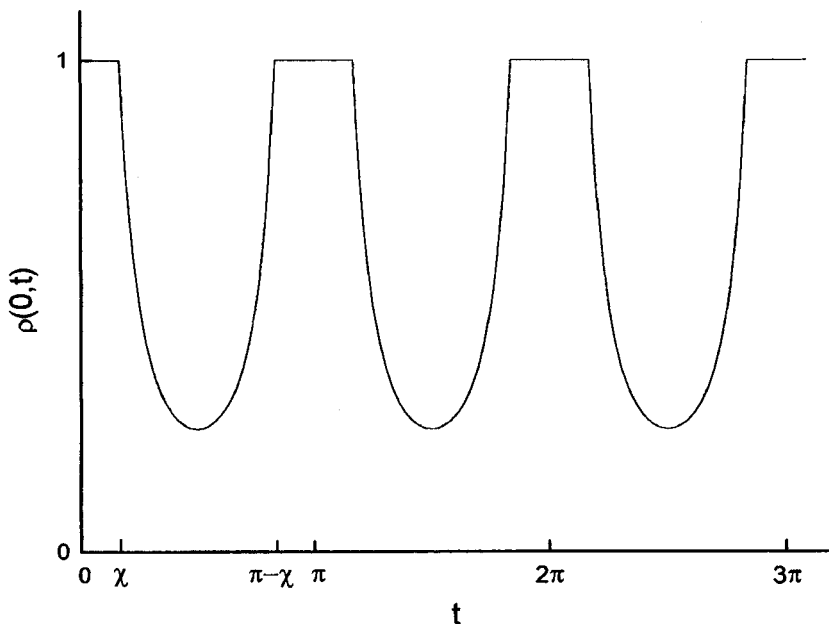

FIG. 3. Varying concentrations of black fraction on left half of free surface.

Our conclusions only refer to an exactly half-filled drum. In other cases, all the material (apart from that in the central part of the drum if it is more than half-full) is ultimately uniformly mixed.[9]

To conclude we stress that our conclusion that fractions of granular material do not undergo complete mixing in a half-filled rotating drum did not depend on the assumption that the granules are completely mixed in avalanches! Even without this very strong assumption, sections of pure black fraction $\rho = 1$ are repeated periodically on the curve $\rho(0,t)$ (Fig. 3). Our only assumption was that the material is completely mixed, by pouring from the free surface which enabled us to introduce $\rho(0,t)$ between these sections and thus determine its specific behavior.

The author would like to thank E. N. Antonov, S. A. Ktitorov, E. K. Kudinov, A. M. Monakhov, A. N. Samukhin, and Yu. A. Firsov for numerous useful discussions.

[1] H. M. Jaeger, C. H. Liu, and S. R. Nagel, Phys. Rev. Lett. **62**, 40 (1989).
[2] J. Rajchenbach, Phys. Rev. Lett. **65**, 2221 (1990).
[3] M. Bretz, J. B. Cunningham, P. L. Kurczynski, and F. Nori, Phys. Rev. Lett. **69**, 2431 (1992).
[4] G. Metcalfe, T. Shinbrot, J. J. McCarthy, and J. M. Ottino, Nature (London) **374**, 39 (1995).
[5] J. Rosendahl, M. Vekic, and J. E. Rutledge, Phys. Rev. Lett. **73**, 537 (1994).
[6] P. Bak, C. Tang, and K. Wiesenfeld, Phys. Rev. Lett. **59**, 381 (1989).
[7] P. Bak, C. Tang, and K. Wiesenfeld, Phys. Rev. A **38**, 364 (1988).
[8] C. Tang and P. Bak, Phys. Rev. Lett. **60**, 2347 (1988).
[9] S. N. Dorogovtsev, JETP Lett. **62**, 262 (1995).

Translated by R. M. Durham

Rate of energy dissipation of the thermal fluctuation field of the sample at the tip of a tunneling microscope

I. A. Dorofeev

Institute of Physics of Microstructures, Russian Academy of Sciences, Nizhniĭ Novgorod
(Submitted March 26, 1996)
Pis'ma Zh. Tekh. Fiz. **23**, 49–53 (February 12, 1997)

It is shown that the rate of energy dissipation of the thermal field of a sample at the tip of a microscope is inversely proportional to the cube of the distance between tip and sample. © *1997 American Institute of Physics.* [S1063-7850(97)00902-6]

The development of a mechanism for local modification of the surface of a solid usually involves calculating the temperature of the sample material for which various sources of energy release must be taken into account, such as those due to the Joule, Thomson, and Nottingham effects. If bodies in vacuum are separated by large distances, the energy transfer between them may be achieved by the radiative component of the thermal electromagnetic field. The rate of the energy exchange in this case is described by the Stefan–Boltzmann law. If the distances between the bodies are fairly small, so that the energy of the thermal fluctuation field is concentrated mainly in the quasistationary (evanescent) component of the field, the energy transfer will obey completely different laws. For instance, in a geometry typical of a tunneling microscope, where two solids are separated by a short distance d, much smaller than the thermal wavelength $\lambda_T = \hbar c/kT$, where c is the speed of light, k is the Boltzmann constant, and T is the temperature of the solid, we need to know these laws.

In the phenomenological theory[1] the fluctuating electromagnetic field is considered as the field generated by random nonelectromagnetic sources distributed in the material, whose existence is attributed to various fluctuations including quantum and thermal fluctuations. By applying reciprocity theory and the fluctuation dissipation theorem, the various energy characteristics of the random fields can be calculated by deriving suitable correlation functions. In our case, by determining the thermal noise induced at the tip of the needle by a heated sample, we can find the Joule losses. With this aim, we shall solve the problem of the thermal radiation of thin metal conductors having transverse dimensions much shorter than the wavelength. In this approximation the fluctuation current J induced by the thermal field of the surrounding bodies in a thin conductor is expressed as follows:

$$|\overline{I}|^2 = \frac{2}{\pi|\mathcal{E}_0|^2} \int \theta dQ_0, \tag{1}$$

where $\mathcal{E}_0 = ZI_0$ is the lumped integrated emf, Z is the total impedance of the tip, I_0 is the current excited by the lumped emf, $\theta(T) = \hbar\omega/2 + \hbar\omega/(\exp(\hbar\omega/kT)-1)$ is the average energy of the oscillator at temperature T, and dQ_0 are the Joule losses of the electromagnetic field of the oscillator in a volume element of the sample. Knowing Eq. (1), we can find the unknown thermal loss power at the tip using the formula

$$W_{ev} = 2 \int_0^\infty \mathrm{Re} Z|\overline{I}|^2 d\omega. \tag{2}$$

We shall assume that at a tip having the radius of curvature p, there is an oscillator at the distance $h = d+p$ from the surface of the half-space. The electric dipole moment of the oscillator is $\mathcal{L} = (I_0 p/i\omega)\mathbf{e}$, where i is the imaginary unit and $\mathbf{e}$ is the unit vector. The power loss of the electromagnetic field of an oscillator in a half-space filled with an isotropic conducting medium having the complex permittivity $\varepsilon_1 = \varepsilon_1' - i\varepsilon_1''$ was determined in Ref. 2, and for an arbitrarily oriented electric dipole is given by

$$Q_0 = \frac{\omega^2}{4c} \int_0^\infty \exp(-(q+q^*)h)\rho d\rho[i(|\mathcal{L}_x|^2 + |\mathcal{L}_y|^2)$$

$$\times(|q|^2 \mathcal{S}_\varepsilon/k^2 + \mathcal{S}_\mu) + 2|\mathcal{L}_z|^2 \rho^2 \mathcal{S}_\varepsilon/k^2], \tag{3}$$

where $\mathcal{S}_\varepsilon = k(q_1^*/\varepsilon_1^* - q_1/\varepsilon_1)/|q+q_1/\varepsilon_1|^2$, $\mathcal{S}_\mu$ is obtained by substituting μ_1 for ε_1, c is the speed of light, $q = (\rho^2 - k^2)^{1/2}$, and $q_1 = (\rho^2 - k_1^2)^{1/2}$.

Let us consider the case where the dipole is oriented along the z axis. The case of arbitrary orientation is analyzed similarly. For short distances, when $kh \ll 1$, the wave component of the field may be neglected and only the quasistationary field is taken into account, corresponding to $\rho > k$. Repeating calculations similar to those performed in Ref. 2, we find that up to terms of order $(kh)^{-2}$, $Q_0 = I_0^2 p^2 \varepsilon_1''/2\omega h^3 |1+\varepsilon_1|^2$. The total impedance of a tip of
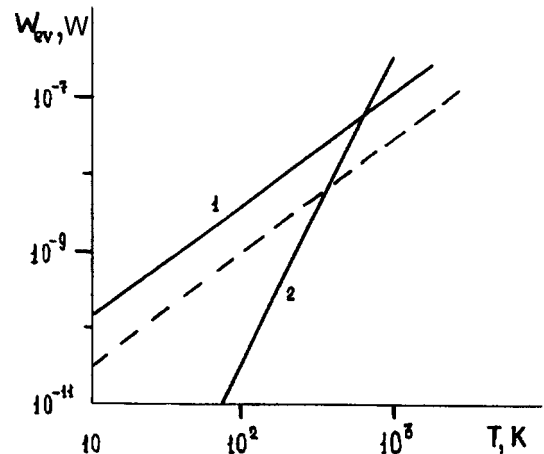

FIG. 1.

approximate size p is written as $Z=(1-i)(\omega/2\pi\sigma c^2)^{1/2}$ (Ref. 4). Assuming $\varepsilon_1 = 1 - i4\pi\sigma/\omega$, and substituting Eq. (1) and the expression for Q_0 into Eq. (2), we finally obtain

$$W_{ev} = \frac{\hbar\sigma c p^2}{8(2\pi^3)^2 h^3} \int_0^\infty \frac{x^{1/2}dx}{[\exp(\alpha x)-1](1+x^2/4\pi^2)}, \quad (4)$$

where $x = \omega/\sigma$ and $\alpha = \hbar\sigma/kT$.

Thus the Joule power loss is found to be inversely proportional to the cube of h. The estimate of W_{ev} will obviously be more accurate, the smaller the tip (the value of p).

It should be noted that W_{ev} has the meaning of the difference between the power generated at the tip by the fluctuation field of a sample at the temperature T_1 and the power released in the sample by dissipation of the fluctuation field of the tip at the temperature T_2. Thus Eq. (4) does not contain the zero-point vibrational energy generated by the entire space because any energy flux from these vibrations in any direction is completely canceled by an opposite flux.

The authors of Ref. 3 solved a similar problem in the one-dimensional case where two half-spaces are separated by a certain distance d in our notation. The power transferred by evanescent waves per unit surface area from one half-space at temperature T_1 to another at temperature T_2 is expressed in the form

$$W'_{ev} = \frac{\hbar\sigma^2}{\pi^2 d^2} \int_0^\infty \frac{[\exp(\alpha_2 x)-\exp(\alpha_1 x)]x\,dx}{[\exp(\alpha_1 x)-1][\exp(\alpha_2 x)-1]}$$

$$\times \int_0^\infty \frac{y\exp(-y)dy}{1+x^2/\pi^2+16\pi^2(1-\exp(-y))^2/x^2-8(1-\exp(-y))}.$$
$$(5)$$

It can be seen from the results obtained in Ref. 3 that in the one-dimensional case, the dissipated power is inversely pro-

portional to the square of the distance between the planar surfaces. Assuming that the effective receiving area of the tip is of the order of πp^2, we obtain $W_{ev} = W'_{ev}\pi p^2$.

Numerical calculations were made for the case $T_2 = 0$, $\Delta T = T_1 - T_2 = T$, which has the same meaning as the energy exchange mechanism being studied. Figure 1 gives the results of the calculations using formulas (4) and (5) for the case $d = 10^{-7}$ cm when the electrical conductivity of the tip and sample materials is $\lambda = 2\times10^{16}$ s^{-1}, which corresponds to tungsten. Curve 1 was calculated using formula (4) and curve 2 using formula (5). The dashed curve was calculated using formula (4) for the electrical conductivity of gold ($\lambda = 3.5\times10^{17}$ s^{-1}). The calculations using both formulas indicate that the transferred power is several orders of magnitude higher than that predicted by the Stefan–Boltzmann law.

Note that the formulas for the rate of energy dissipation of a fluctuation field were derived under the assumption of δ-correlated random sources in the medium. Allowance for the finite correlation length yields a different the dependence on the interelectrode gap, at any rate for distances comparable with the correlation length.

[1] S. M. Rytov, *Theory of Electric Fluctuations and Thermal Radiation* [in Russian], USSR Academy of Sciences Press, Moscow (1953).
[2] M. L. Levin and S. M. Rytov, *Theory of Equilibrium Thermal Fluctuations in Electrodynamics* [in Russian], Nauka, Moscow (1967).
[3] J. J. Loomis and H. J. Maris, Phys. Rev. B **50**, 18 517 (1994).
[4] L. A. Vaĭnshteĭn, *Electromagnetic Waves* [in Russian], Sov. Radio, Moscow (1957).

Translated by R. M. Durham

Some aspects of recording an acoustic wave in a liquid by a fiber-mounted piezoelectric transducer

A. V. Belikov, A. V. Erofeev, Yu. A. Sinel'nik, and Yu. V. Sudenkov

State Institute of Precise Mechanics and Optics, St. Petersburg;
St. Petersburg State University

The main characteristics of a piezoelectric transducer mounted on an optical fiber and used to measure the acoustic signals induced by interaction between the radiation and the material are described. Results of an investigation of a laser-induced acoustic signal in a liquid are presented. © *1997 American Institute of Physics.* [S1063-7850(97)01002-1]

The widespread application of lasers with fiber-optic systems of radiation delivery in modern physics, engineering, and medicine brings with it the need to develop new systems for monitoring and controlling this radiation. In order to control laser damage to materials, information is required on the dynamics of the processes producing this damage. An obvious example of laser-induced effects in a material is the formation of an acoustic wave.[1]. In many cases, an analysis of the amplitude and frequency characteristics of a laser-induced acoustic wave provides information on the actual damage process (the damage efficiency, depth of the damaged layer, and so forth). Acoustic waves are conventionally recorded by microphones[2] distributed in the medium (water, air) surrounding the interaction site, but when fiber-optic delivery systems are used such measurements are beset with severe technical difficulties. In the present paper we describe the main characteristics of a piezoelectric transducer mounted on an optical fiber and used to measure the acoustic signals induced by interaction between the radiation and the material. Results of an investigation of a laser-induced acoustic signal in a liquid are presented.

We made an experimental investigation of the characteristics of a laser-induced acoustic signal produced by the interaction of YAG:Nd ($\lambda = 1.06$ μm) laser radiation and an aqueous dye solution (India ink). The laser energy density was varied in the range 10–160 J/cm^2 with a pulse repetition frequency of 10 Hz. The energy and duration of the acoustic response recorded by the transducer were determined experimentally as a function of the dye concentration in the aqueous solution at constant laser radiation energy. The output end of the fiber was inserted in a vessel containing an aqueous solution of the dye (India ink). The depth of immersion of the fiber end was around 30 mm (from the surface). In all cases the volume of water was 50 ml. The dye concentration in the solution was varied between 0.01% and 0.2%. The fiber transducer was mounted nearer to the output end of the fiber (around 50 mm) to minimize attenuation of the acoustic wave as it propagates through the fiber material. A quartz–quartz optical fiber with a light-guiding core diameter of 500 ± 20 μm was used. For further processing the signals from the transducers were fed to an S9-8+KOP oscilloscope connected to a PC/AT 486-120.

The operating principle of the acoustooptic transducer used to measure the parameters of an acoustic signal induced by interaction between laser radiation and a material (gas, liquid, or solid) is based on recording the dynamic deformations generated in an optical fiber in contact with the material. In this case, the optical fiber to which the transducer was fixed was both a light guide and a sound guide for the acoustic wave generated in the liquid (India ink) as a result of laser irradiation at the interaction point. The interaction point was the point of contact between the far end of the fiber and the liquid. Experiments to determine the distance (h) between
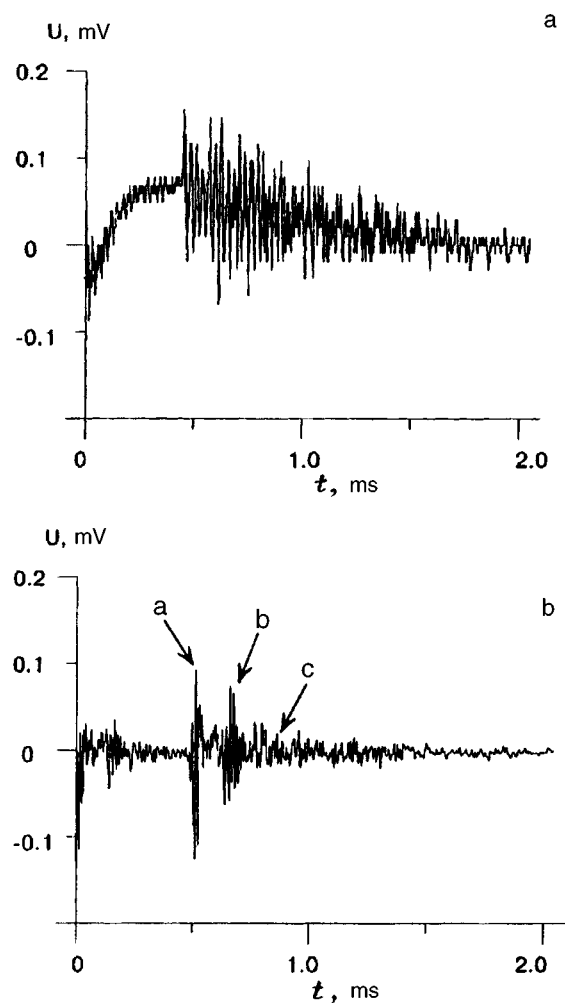

FIG. 1. Oscilloscope traces of laser-induced acoustic signal: a — YAG:Nd, 1.06 μm, 125 J/cm^2, concentration 0.008; b — YAG:Nd, 1.06 μm, 125 J/cm^2, concentration 0.9.

the interaction point and the transducer attachment point for which the signal-to-noise ratio exceeded 10, showed that this distance was about 50 mm. An increase in h caused this ratio to deteriorate.

Typical oscilloscope traces for various dye concentrations show that when the energy density of the 1.06 μm radiation is around 125 J/cm^2, the formation of acoustic vibrations (as a result of microexplosions accompanying the absorption of light by dye particles) in the aqueous solution of India ink is a threshold process and begins to be observed reliably above a concentration (c) of around 0.004–0.008. A typical signal recorded by the transducer in this case is shown in Fig. 1a. It can be seen that this signal is a superposition of two signals, a low-frequency and a high-frequency one. The low-frequency signal is due to the pyroelectric signal produced by light scattering in the fiber material and carries information on the laser radiation energy. This statement is supported by the fact that the signal shape and amplitude do not vary with dye concentration, and the parameters depend clearly on the laser radiation energy. The high-frequency (acoustic) signal is due to the piezoelectric response and characterizes the interaction between the laser radiation and the material, as is indicated by the dependence of its parameters on the dye concentration. An increase in the dye concentration enhances the amplitude of the acoustic signal and alters its frequency spectrum. The time resolution may be estimated as:

$$\tau \approx \frac{l}{V}, \tag{1}$$

where l is a linear dimension (the transducer–fiber contact length) and V is the speed of sound in the fiber.

In our case the resolution is $\tau \approx 10^{-6}$ s. A typical signal for concentrations close to 1 is shown in Fig. 1b. It can be seen that the transducer records the acoustic response not only from the interaction point (a), but also from the surface of the liquid (b) and the walls of the vessel (c).

Figure 2 shows typical behavior of the laser-induced (YAG:Nd, 1.06 μm) acoustic signal energy as a function of the dye (India ink) concentration. The minimum near a con-

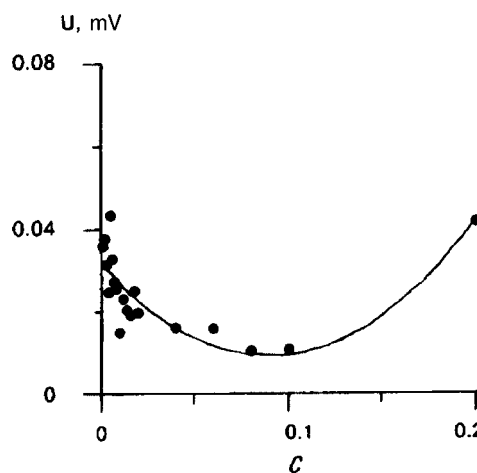FIG. 2. Energy of laser-induced acoustic signal versus concentration of India ink dye for YAG:Nd, 1.06 μm.

centration of 0.1 is most likely caused by competition between two mechanisms for formation of the acoustic wave: one is associated with heating and expansion of the Indian ink particles in the laser pulse field and dominates at low concentrations while the other is due to microexplosions of Indian ink particles and interaction between heated particles.

As a result of these investigations, we were therefore able to develop a miniature, sensitive, spectrally selective acoustooptic fiber transducer capable of recording simultaneously both the laser radiation (pulse) energy and the signal accompanying the interaction between the laser radiation and the material in a band of up to 1 MHz. This transducer was used as the basis to develop a feedback system incorporating a transducer, an analog-to-digital converter, a computer, a digital-to-analog converter, and devices to alter the energy (power) and time structure of the laser radiation.

[1] V. E. Gusev and A. A. Karabutov, *Laser Optoacoustics* (Bristol, 1993).
[2] A. V. Belikov, A. G. Novikov, and A. V. Scrypnik, Proc. SPIE **2623**, 109 (1995).

Translated by R. M. Durham

A new fiber acoustic laser-energy detector

A. V. Belikov, A. V. Erofeev, A. V. Skripnik, Yu. A. Sinel'nik, and Yu. V. Sudenkov

State Institute of Precise Mechanics and Optics, St. Petersburg, St. Petersburg State University

A novel detector capable of measuring the energy of pulsed laser radiation coupled into an optical fiber and the acoustic signals induced by interaction between this radiation and matter is described. Results of a study of the capabilities of this optoacoustic detector are presented. © *1997 American Institute of Physics.* [S1063-7850(97)01102-6]

The development of integrated optics and the widespread application of lasers with fiber-optic systems for delivering the radiation in modern physics, engineering, and medicine has brought with it the need to develop new radiation monitoring and control systems, or feedback systems. In the vast majority of cases, it is sufficient to regulate the average radiation power to control processes of laser damage to materials.[1] The control criterion in this case may be taken as the excess of the laser energy above a certain threshold that causes changes in the state of the object (such as damage, modification, and so forth).[2] The laser radiation energy (power) is conventionally measured by calorimetric or optoelectronic techniques,[3] but when fiber-optic delivery systems are used, these methods of measurement encounter major technical difficulties. Here we describe a novel detector capable of measuring the energy of pulsed laser radiation coupled into an optical fiber and the acoustic signals induced by the interaction of this radiation with matter. Results of a study of the capabilities of this optoacoustic detector are presented.

The profile and amplitude of the pyroelectric signal from the detector were investigated experimentally as functions of the energy and wavelength of the laser radiation transferred along different types of optical fiber. Radiation from YAG:Nd (λ=1.06 μm and λ=1.44 μm), YAG:Cr;TmHo (λ=2.088 μm), and YAG:Er (λ=2.94 μm) lasers was passed through an optical system of mirrors and was focused by a CaF$_2$ lens onto the input end of the fiber. The laser energy density was varied in the range 10–160 J/cm^2 at a pulse repetition frequency of 10 Hz. A plane-parallel plate directed some of the radiation to a calorimetric energy meter which recorded the power (energy) of the laser radiation incident at the input end of the waveguide. The laser energy thus measured was used to calculate the efficiency of coupling the laser radiation into the fiber. An acoustooptic fiber transducer was attached at a point around 20 mm from the inlet end of the fiber. An additional calorimetric energy meter recorded the laser radiation energy after passage through the fiber. The correspondence between the amplitude of the signal from the acoustooptic fiber transducer and the laser radiation energy after passage through the fiber was investigated experimentally. We used hollow fibers, quartz fibers, and germanate (Ge-glass) fibers with a light-guiding core diameter of 500±20 μm. For processing the signals from the detectors were fed to an S9-8+KOP oscilloscope connected to a PC/AT 486-120.

The operating principle of the detector when used to measure the energy characteristics of laser radiation is based on the linearity of the relation between the light scattered in the optical material and the recorded pyroelectric signal ex-
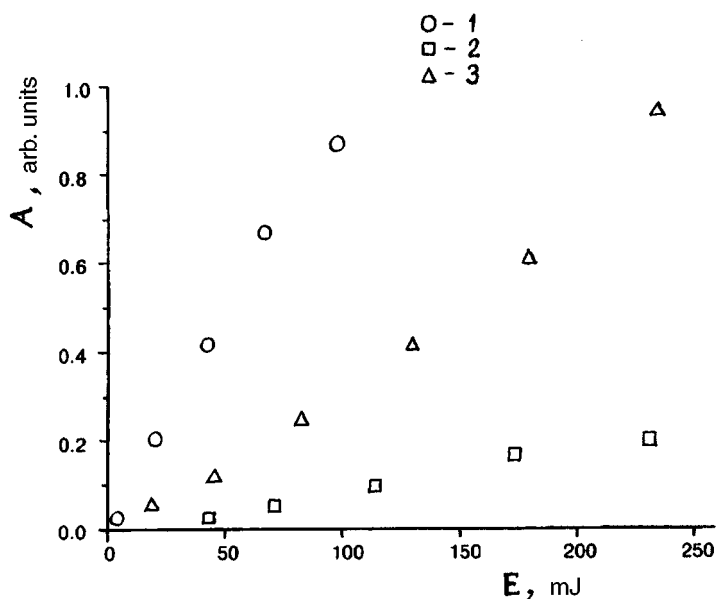

FIG. 1. Relative amplitude of signal from acoustooptic fiber detector as a function of the energy of various lasers after passage through a quartz–quartz fiber. Wavelength: *1* — 1.44 μm, *2* — 0.88 μm, and *3* — 2.94 μm.
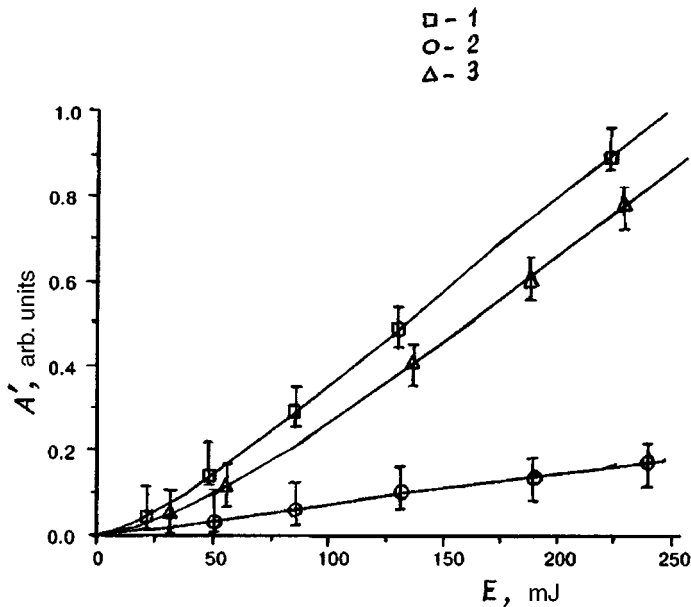
FIG. 2. Relative amplitude of signal from acoustooptic detector as a function of YAG:Er laser radiation energy after passage through different optical fibers: *1* — quartz fiber, *2* — hollow fiber, and *3* — Ge-glass.

cited by the scattered wave. The signal from the detector is the result of integrating the spiky structure of the laser pulse, as is evidenced by the fact that the time when the detector signal reaches a maximum coincides with the end of the laser pulse ($t \approx 100$–200 μs). The signal can then be processed by a peak detector and a quantity proportional to the laser pulse energy thus determined. In the course of the present study, we were particularly interested in the universality of this acoustooptic fiber transducer for optical fibers of various types and for different radiation wavelengths.

Figure 1 gives the amplitude of the signal from the acoustooptic fiber transducer mounted on a quartz fiber as a function of the energy incident at the input end of the fiber for laser radiation of different wavelengths. Figure 2 shows the relation between the amplitude of the pyroelectric signal from the acoustooptic transducer and the radiation energy of a submillisecond YAG:Er pulsed laser after passage through quartz–quartz, hollow, and Ge-glass optical fibers.

These dependences suggest that the calibration characteristic of the acoustooptic fiber transducer is linear over the entire range of laser energies used.

The dependence plotted in Fig. 1 confirms that the amplitude of the signal recorded by the detector clearly depends on the laser wavelength, which suggests that this detector is wavelength selective. The selectivity is caused by a difference in the scattering coefficient of quartz at different wavelengths. Note that the maximum signal was observed for the 1.44 μm wavelength, which can be described by the following wavelength dependence of the scattering intensity:

$$I_{\text{scat}} \approx \frac{1}{\lambda^k}, \tag{1}$$

where I_{scat} is the amplitude of the signal scattered in the optical fiber, λ is the wavelength of the laser radiation, and k is an empirical factor. The curves plotted in Fig. 2 illustrate that differences in the amplitude of the recorded signal are observed for fibers of different type. An analysis of the struc-

ture of these fibers revealed that this effect may occur because the scattering of 2.94 μm light is greater for quartz–quartz and Ge-glass fibers (about the same for these two) and weaker for hollow fibers (although this does not include the losses in the fiber).

We draw attention to the fact that investigations of the sensitivity threshold of the acoustooptic detector have shown that the sensitivity does not depend on the laser pulse length and is around 1 mJ for all the laser sources studied.

In summary, an acoustic detector mounted on a fiber which carries laser radiation to an interaction site has been developed and studied for the first time. The detector can be used

- to measure the energy of laser radiation that has passed through the fiber;

- to measure the coefficient of coupling the laser radiation into the fiber;

- to measure the energy of the laser-induced acoustic wave;

- to measure the frequency of the laser-induced acoustic wave;

- to determine the onset of degradation of the fiber properties;

- to investigate the thermal and acoustic characteristics of various systems.

[1] M. J. Weber, *Handbook of Laser Science and Technology* (CRC Press, 1991).

[2] A. V. Belikov, A. G. Novikov, and A. V. Scrypnik, Proc. SPIE **2623**, 109 (1995).

[3] N. V. Karlov, *Lectures on Quantum Electronics* [in Russian], Nauka, Moscow (1988).

[4] V. E. Gusev and A. A. Karabutov, *Laser Optoacoustics* (Bristol, 1993).

Translated by R. M. Durham

114   Tech. Phys. Lett. **23** (2), February 1997

Belikov *et al.*   114

Diffraction of light by agglomerates in a layer of magnetic fluid situated in a magnetic field parallel to the plane of the layer

D. A. Usanov, A. V. Skripal', and S. A. Ermolaev

Saratov State University

Previously unknown behavior observed when laser radiation propagates through a layer of magnetic fluid with and without an external magnetic field are established for the first time and their physical nature is explained. © *1997 American Institute of Physics.*
[S1063-7850(97)01202-0]

The strongest diffraction of light has been observed when an external magnetic field is oriented at right angles to the boundaries of a plane layer of magnetic fluid.[1] In this case, the action of a static magnetic field directed along the laser beam produces a characteristic diffraction scattering pattern comprising one or several rings.[2,3] However, no description has been given of the diffraction pattern obtained when the external magnetic field is oriented along a plane layer of magnetic fluid or how this pattern changes with the magnitude and direction of the magnetic field situated in this plane.

The pattern of light diffraction by agglomerates of a magnetic fluid was observed experimentally for this particular case using the apparatus shown schematically in Fig. 1. Radiation from a laser *1* at 0.6328 μm in a 3-mm diameter beam was directed onto a plane layer of magnetic fluid consisting of water and magnetite particles coated with sodium oleate with a solid-phase concentration $\varphi = 0.1$, positioned between two glass plates *2*. After passing through the layer of magnetic fluid, the light beam shaped as the diagram *9* was observed on a screen *5* and recorded by a photodetector *6* and an automatic plotter *7*. When a magnetic field was applied to the magnetic fluid using the poles of an electromagnet *3* and a power supply *4*, the beam was transformed into a strip of light *8* whose longitudinal axis was perpendicular to the magnetic field **B**. The light intensity in the strip increased with increasing magnetic field. When the direction of the applied magnetic field was rotated in the plane of the

layer, as shown by the dashed line, the longitudinal axis of the strip was observed to rotate in the direction of the magnetic field.

The light intensity in the strip was perceived as uniform. This diffraction pattern corresponds to the case where the light passes through a system of nontransparent filaments arranged perpendicular to the direction of propagation. In our case, ordered ferroparticles function as these filaments. Distinguishing features of this particular case are the quasiperiodic discontinuity of the ferroparticle filaments and their lack of strict spatial periodicity. As a consequence of this quasiperiodicity, intensity maxima and minima should be observed within the light strip. This supposition was checked out experimentally. Figure 2(a) gives the voltage on the photodiode as a function of its position along the coordinate axis perpendicular to the direction of the applied field. It can be seen from Fig. 2(a) that a typical diffraction pattern of alter-

FIG. 2. Normalized voltage on photodiode versus its position along coordinate axis perpendicular to the magnetic field: a — when light propagates through the layer of magnetic fluid and b — when it propagates through the dried layer of ferroparticles.
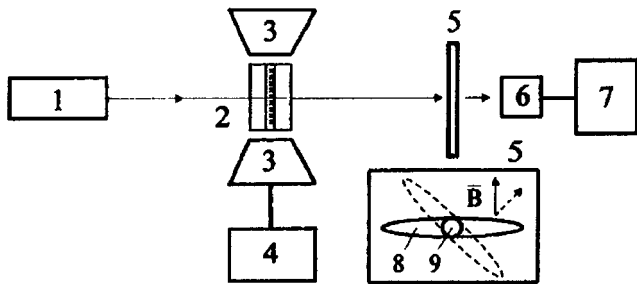

FIG. 1. Schematic diagram of apparatus: *1* — laser, *2* — layer of magnetic fluid between two glass plates, *3* — poles of electromagnet, *4* — power supply for electromagnet, *5* — screen, *6* — photodetector, *7* — automatic plotter, *8* — shape of light beam in magnetic field, *9* — shape of light beam without magnetic field (the dashed line indicates the direction of rotation of the light strip when the direction of the applied magnetic field is rotated).
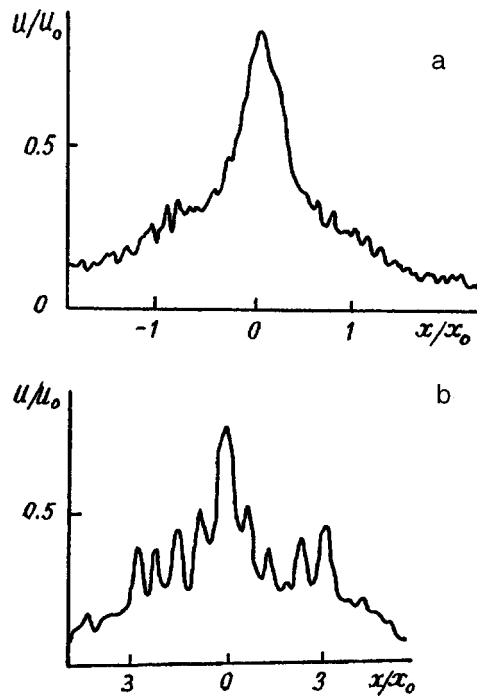
nating scattered-light intensity peaks and troughs is observed.

A layer of magnetic fluid deposited on a glass substrate was dried in a static magnetic field in order to confirm the assumption that filaments of ferroparticles formed in the magnetic field and oriented in the direction of this field are responsible for the typical diffraction pattern observed. After being passed through the glass plate containing the dried layer of ferroparticles, the light beam was also transformed into a narrow strip of light, even in the absence of the magnetic field. When the plate with the dried layer of ferroparticles was rotated in the plane perpendicular to the direction of propagation of the light, the axis of the strip rotated in the same direction as the plate. Figure 2(b) shows the diffraction pattern obtained when a sample of the dried magnetic structure was illuminated with He–Ne laser radiation. The thickness of the fluid layer measured with an MII-4 microinterferometer was 1.5 μm.

It has therefore been shown that when light is scattered by a thin layer of magnetic fluid in a magnetic field oriented along the boundaries of the plane layer, a strip of light having alternating intensity maxima and minima is formed, typical of the diffraction by a quasiperiodic grating. When the direction of the applied magnetic field is rotated in the plane of the layer, the longitudinal axis of the strip is observed to rotate in the same direction as the magnetic field.

[1] J. C. Bacri and D. Salin, J. Phys. (Paris) **41**, L771 (1982).
[2] Yu. I. Dikanskiĭ and A. O. Tsebers, Magn. Gidrodinam. No. 2, 47 (1990).
[3] W. E. L. Haas and J. E. Adams, Appl. Phys. Lett. **27**, 571 (1975).

Translated by R. M. Durham

Some features of the kinetics of high-speed penetration in brittle media

A. S. Vlasov, Yu. A. Emel'yanov, E. L. Zil'berbrand, A. A. Kozhushko, A. I. Kozachuk, G. S. Pugachev, and A. B. Sinani

A. F. Ioffe Physicotechnical Institute, Russian Academy of Sciences, St. Petersburg

The kinetics of the high-speed penetration of deformable rods into ceramics has been investigated. It is established that penetration takes place by a two-stage process. In the first stage the penetration velocity increases with increasing damage to the ceramic. The second stage corresponds to quasisteady penetration into a medium devoid of strength. It is shown that the first stage determines the high level of resistance of ceramics to high-intensity impact loading. © *1997 American Institute of Physics.* [S1063-7850(97)01302-5]

Extremely hard brittle materials (especially ceramics) have recently been investigated intensively because of the prospects for using these materials to protect against high-velocity impact.[1,2] To understand the behavior of ceramics under these conditions, it is important to study the time evolution of the penetration of an impacting body. This is because the resistance of brittle materials to penetration should depend strongly on time, unlike that of plastic materials. Existing studies[3–5] provide qualitative confirmation of this behavior but cannot be used to establish any general laws governing the change in the penetration parameters over the entire process.

The aim of the present study was to investigate the kinetics of penetration of deformable metal rods into ceramics of different composition with a high degree of time resolution over the entire interaction process.

The investigation was carried out using a four-frame pulsed x-ray system with an exposure of $\sim$0.1 μs (working voltage 400–450 kV). Data were obtained experimentally on the position of the rod in the ceramic at specific fixed time points to within 0.1 μs. By differentiating the position-time curves obtained, we were able to determine the time dependence of the penetration velocity, which uniquely characterizes the resistance to penetration.[6]

The ceramics were subjected to impact by soft steel and plastic tungsten alloy rods (3 mm in diameter and 30 mm long) at velocities between 1300 and 1600 m/s.

The experiments were carried out using samples made of silicate glass, boron carbide (B_4C), silicon carbide (SiC), a 70/30 mixture of aluminum nitride and titanium nitride (AlN/TiN), and aluminum oxide (Al_2O_3). The samples were 100 mm thick and had transverse dimensions of 20×20 mm and 40×40 mm. Different transverse dimensions were used in order to investigate the influence of damage from the side surfaces. The thickness of the samples eliminated any influence due to damage at the rear free surface throughout the interaction process.

Figure 1 gives the penetration velocity U as a function of the time t after impact for AlN/TiN (*1*), Al_2O_3 (*2*), B_4C (*3*), SiC (*4*), and silicate glass (*5*) under impact by a steel rod at a velocity of 1600 m/s. These dependences show common behavior for the various materials studied: three characteristic sections can be identified on all the curves $U(t)$.

The first (descending) branch of the curve corresponds to the transition from the mass velocity, determined by the impact adiabatic curves of the interacting bodies,[7] to the penetration velocity. In other words, this branch describes the transition from shock wave displacement of the contact surface to actual penetration.

The second section corresponds to penetration at varying velocity. Here the velocity changes from a certain minimum at the onset of penetration to a nearly constant value.

The third section corresponds to constant-velocity penetration.

The actual penetration process can therefore be arbitrarily divided into two stages: a first, low-velocity penetration stage and a second, quasisteady penetration stage.

The effective penetration resistance can be estimated from the data on the penetration velocity. By this we understand the resistance due to the strength of the material, supplementing the inertial penetration resistance. The effective penetration resistance can be calculated using the familiar Alekseevskiĭ–Tate equation[8,9]

$$\rho_1 U^2/2 + R = \rho_2(V-U)^2/2 + Y,$$

where ρ_1 and ρ_2 are the density of the medium and the striker, respectively, V is the impact velocity, U is the penetration velocity, and R and Y are strength parameters of the medium and the striker, respectively.

Calculations using this system are fairly standard[4,5] but we appreciate that they are rather approximate. Strictly speaking, the above equation only applies to penetration into plastic media as opposed to penetration into a disintegrating brittle medium. Nevertheless, even an estimate of the change in the effective resistance with time may give some indication of the kinetics of brittle damage during penetration.

Figure 2 gives the effective resistance $R-Y$ as a function of the time t after impact for Al_2O_3 under impact by a steel rod at a velocity of 1600 m/s. These data suggest that the effective resistance decreases progressively. A comparison between Figs. 1 and 2 indicates that the material possesses the highest resistance at the first, low-velocity stage of the interaction. The first stage terminates when the strength of the material is exhausted. In the second, quasisteady stage the effective resistance falls to a negligibly low level and the penetration velocity is close to the constant value calculated
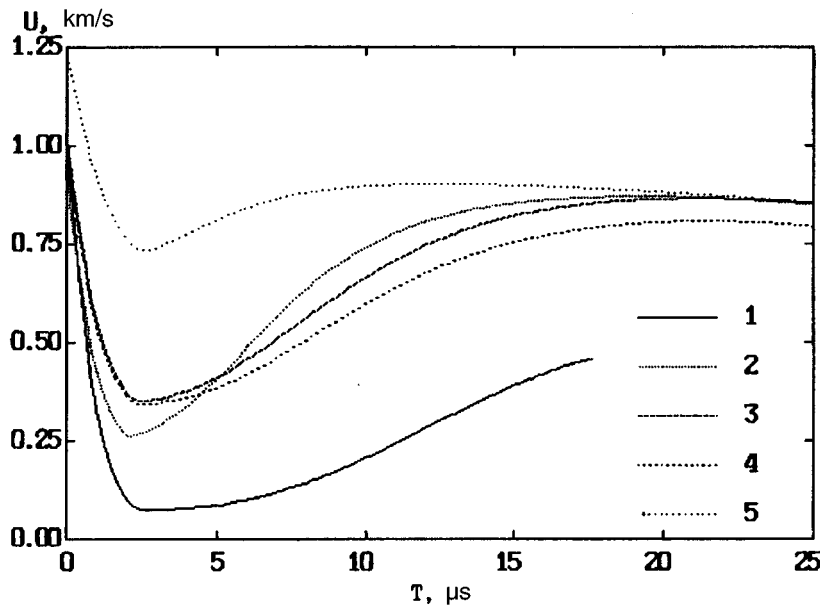
FIG. 1.

using the hydrodynamic model.[6] In other words, the penetration resistance is inertial and is determined only by the density of the interacting bodies.

This change in the penetration resistance of brittle media can logically be related to their damage kinetics. Two limiting cases can be identified in the interaction between brittle media and a striker: the first is deformation of the striker at the surface of the undamaged ceramic under conditions similar to deformation at a ''rigid wall'' ($U=0$), and the second is motion in a medium devoid of strength. In the real process, a gradual transition takes place from the first to the second regime, causing a progressive drop in the penetration resistance. From this it can be seen that the high strength of ceramics under impact is determined by the first, low-velocity penetration stage, and specifically by its duration and minimum penetration velocity.

The duration of this stage and the minimum penetration velocity for a given obstacle material depend strongly on the sample geometry and on the pressure at the contact surface, which is determined by the impact velocity and by the density of the striker.

These experimental data show that as the transverse dimensions of the sample are reduced, the duration of the low-velocity penetration stage becomes shorter. The sample is damaged more intensively under the action of tensile stress waves propagating from the free side surfaces. The time of arrival of these waves at the contact surface naturally depends on the size of the sample. The minimum penetration velocity does not vary as the transverse dimensions of the sample decrease. This is because in the selected sample geometry the tensile stress wave does not reach the contact
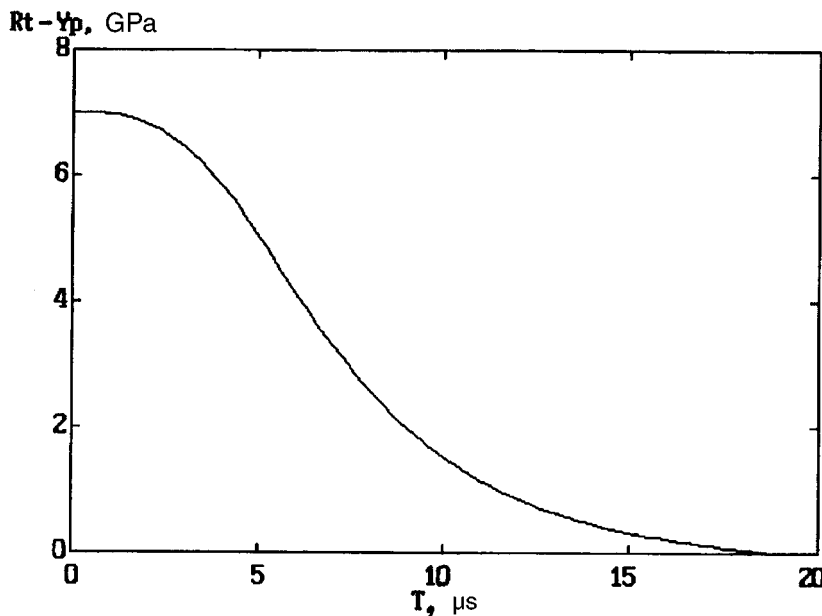

FIG. 2.

surface before the minimum penetration velocity is established.

These data indicate that as the impact velocity and the density of the striker are increased, the minimum penetration velocity increases and the low-velocity penetration stage becomes shorter. This is because of the increased shock-wave load on the material which accelerates the initiation and evolution of brittle fracture in the sample.

It can be seen from Fig. 1 that the penetration kinetics differ substantially for different samples. In particular, the low-velocity penetration stage (high resistance) is less clearly defined in glass, which has the lowest strength, hardness, and fracture viscosity. Further studies are required to examine the correlation between the physicomechanical characteristics and the parameters of the penetration process for ceramics.

In conclusion, the kinetics of the penetration of deformable rods in ceramics has therefore been investigated comprehensively over the entire interaction process. It has thus been possible to show for the first time that high-speed penetration in brittle materials involves a two-stage process. The first stage involves low-velocity penetration, the velocity increasing as the damage to the ceramic increases, and the second stage consists of quasisteady penetration in a medium devoid of strength. A high level of penetration resistance is observed in the first stage and this is the stage that determines the high efficiency of ceramics as a construction material under intense dynamic loading.

[1] S. Bless, Z. Rosenberg, and B. Yoon, Int. J. Impact Eng. **5**, 165 (1987).
[2] J. Stemberg, J. Appl. Phys. **65**, 3417 (1989).
[3] E. L. Zil'berbrand, N. A. Zlatin, A. A. Kozhushko, V. I. Polozenko, G. S. Pugachev, and A. B. Sinani, Zh. Tekh. Fiz. **59**(10), 54 (1989) [Sov. Phys. Tech. Phys. **34**, 1123 (1989)].
[4] G. E. Hauver, W. A. Gooch, P. H. Netherwood, R. F. Benck, W. J. Perciballi, and M. S. Burkins, Proc. 13th Int. Symposium on Ballistics, Stockholm, 1992, pp. 257–264.
[5] D. Orphal, R. Franzen, A. Piekutowski, and M. Forrestall, Int. J. Impact. Eng. **18**, 355 (1996).
[6] M. A. Lavrent'ev, Usp. Mat. Nauk. **12**(4), 41 (1957).
[7] Ya. B. Zel'dovich and Yu. P. Raizer, *Physics of Shock Waves and High-Temperature Hydrodynamic Phenomena*, Vols. 1 and 2, transl., of 1st Russ. ed. (Academic Press, New York, 1966, 1967) [Russ. original, 2nd ed., Nauka, Moscow, 1966].
[8] V. P. Alekseevskiĭ, Fiz. Goreniya. Vyzryva **2**, 99 (1966).
[9] A. Tate, J. Mech. Phys. Solids **15**, 387 (1967).

Translated by R. M. Durham

Coupled vertical microcavities

M. A. Kaliteevskiĭ

A. F. Ioffe Physicotechnical Institute, Russian Academy of Sciences, St. Petersburg
(Submitted November 18, 1996)
Pis'ma Zh. Tekh. Fiz. **23**, 74–78 (February 12, 1997)

A design is proposed for a device consisting of two optically coupled vertical microcavities. It is shown that interaction between two localized optical modes in the coupled microcavities induces mode splitting. The feasibility of using this design to develop optoelectronic devices is analyzed. © *1997 American Institute of Physics.* [S1063-7850(97)01402-X]

It is common knowledge that if two oscillators of arbitrary type, having the same resonant frequencies, are coupled by some type of interaction, the resultant system will possess two resonant frequencies positioned symmetrically about the resonant frequency of the noncoupled oscillators and the splitting of the resonant frequencies will increase as the strength of the coupling interaction is increased.

One manifestation of this effect, known as Rabi splitting and Rabi oscillations, was observed in semiconductor systems at the beginning of the nineties[1–3] in a study of the interaction between localized optical modes and excitons in semiconductor quantum-well microcavities. This observation acted as the stimulus for numerous theoretical and experimental studies on this topic. Another reason for the interest in semiconductor cavities is that they are used to develop vertical-cavity emitting lasers.[7]

A typical microcavity consists of a cavity bounded by two Bragg reflectors. The reflectivity (transmission) spectra of these structures exhibit structure *d* in the form of narrow deep troughs (peaks) whose spectral position matches that of the localized optical modes of the microcavity.

Although considerable attention has been paid worldwide to the study of microcavities and their potential for developing various optoelectronic devices utilizing Rabi splitting and Rabi oscillations, there are no reports of the construction or development of such devices. The main reason for this is the very specific conditions needed for the efficient manifestation of exciton effects (i.e., the need to maintain low temperatures) and also the fact that the required exciton parameters (such as the oscillator strength) cannot be varied widely.

All these difficulties can be surmounted by developing an experimental structure in which the localized optical mode interacts with another localized optical mode rather than with an exciton. A design capable of implementing this idea is shown in Fig. 1. This device consists of two microcavities having a single common central mirror (BR). Cavities *1* and *2* are positioned on either side of the central mirror. The structure is bounded on the outer sides by mirrors BR1 and BR2.

Coupling between the first and second cavities will be most efficient if their natural frequencies are matched.

We shall analyze the optical properties of such a structure. Curve *1* in Fig. 2 gives the transmission spectrum calculated by the method of transfer matrices[8] for a single free microcavity whose mirrors (reflection coefficient 0.99) are formed by twelve pairs of quarter-wave layers having refractive indices of 3.0 and 4.0, respectively. The microcavity has a refractive index of 4.0 and its thickness corresponds to the wavelength of light in the material (known as a
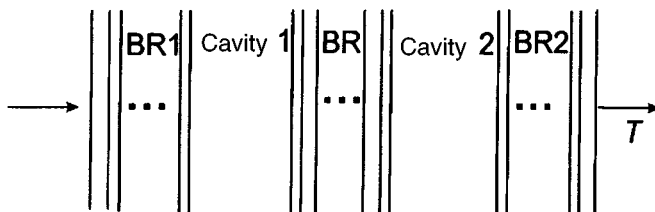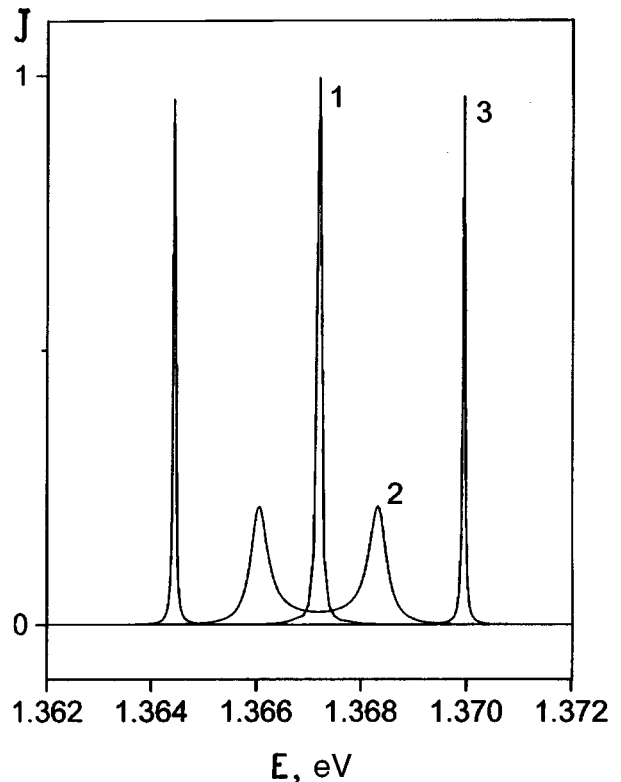

FIG. 2. Calculated transmission spectra for: *1* — single free cavity, *2* — coupled microcavities for which common mirror has a reflection coefficient of 0.9993, and *3* — coupled microcavities for which common mirror has a reflection coefficient of 0.996.

FIG. 1. Diagram of structure.

λ-resonator). The media bounding the microcavity had unity refractive indices. The cavity parameters were selected so that they were similar to those of the structures studied experimentally. It can be seen that the transmission spectrum has a single peak.

Curves *2* and *3* give the transmission spectra for the coupled microcavities. In both cases the outer mirrors consisted of twelve pairs of layers (reflection coefficient 0.999) For case *2* the common mirror was formed by fifteen pairs of layers (reflection coefficient 0.9993) and for case *3* it was formed by twelve pairs of layers (reflection coefficient 0.996). The cavity parameters in the coupled microcavity systems were the same as those for the free cavity. The media bounding the structure had refractive indices of unity.

It can be seen that the transmission spectra for the systems of coupled microcavities each have two peaks positioned symmetrically relative to the natural mode of the free microcavity. The mode splitting depends on the reflection coefficient of the common mirror and decreases as this coefficient increases. By altering the parameters of the common mirror, the mode splitting can be varied quite appreciably.

The mode splitting may induce beats in the optical signal emitted by the coupled microcavity system at a frequency coinciding with the mode splitting. For case *2* the splitting is 3 meV, which corresponds to a beat frequency of 0.6 THz and for case *3*, it is 5 meV corresponding to 1 THz. If an active medium is inserted into one of the cavities, the structure will operate as a laser whose emission is modulated at the beat frequency, so that this structure may be used to generate electromagnetic radiation in the terahertz range.

In addition, this design of coupled microcavity system allows separate electrical control of each cavity, which extends the scope for using the proposed structure in various optoelectronics applications.

[1] C. Weisbouch, M. Nishioka, A. Ishikawa, and Y. Arakawa, Phys. Rev. Lett. **69**, 3314 (1992).

[2] R. Houdre, R. P. Stanley, U. Oesterle, M. Ilgems, and C. Weisbouch, Phys. Rev. B **49**, 16 761 (1994).

[3] J. Tignon, P. Voisin, C. Delande, M. Voos, R. Houdre, U. Oesterle, and R. P. Stanley, Phys. Rev. Lett. **74**, 3967 (1995).

[4] A. V. Kavokin and M. A. Kaliteevski, Solid State Commun. **95**, 859 (1995).

[5] E. L. Ivchenko, M. A. Kaliteevski, A. V. Kavokin, and N. A. Nesvihzskii, J. Opt. Soc. Am. **13**, 327 (1996).

[6] V. Savona, L. C. Andreani, P. Schwendimann, and A. Quatropani, Solid State Commun. **93**, 733 (1995).

[7] J. L. Jewell, J. P. Haribson, A. Scherer, Y. H. Lee, and L. T. Florez, IEEE J. Quantum Electron. **27**, 1332 (1991).

[8] M. Born and E. Wolf, *Principles of Optics*, 4th ed. (Pergamon Press, Oxford, 1969) [Russ. transl. Nauka, Moscow 1973].

Diffraction of light by a pseudodeep holographic grating

S. Ya. Gorelik

Institute of Precise Mechanics and Optics, St. Petersburg (Technical University)

Results are presented of a theoretical and experimental study of the recording of pseudodeep holograms. A mathematical model is proposed for the diffraction of light by a pseudodeep hologram structure. An experimental confirmation of the theory has been presented in *Pis'ma v Zhurnal Technicheskoĭ Fiziki [Tech. Phys. Lett.].* © *1997 American Institute of Physics.*
[S1063-7850(97)01502-4]

A method of recording and reconstructing images using pseudodeep holograms has already been proposed[1,2] and a graphical method to construct the image reconstructed by this type of hologram has been suggested.[3] In the present paper we propose a mathematical model of the diffraction of light by a pseudodeep holographic grating.

Let us consider the interference that takes place between two plane waves, an object wave S and a reference wave R, whose complex amplitudes are described by the functions $S = \exp[-jk(y \sin \Theta_0 + z \cos \Theta_0)]$ and $R = \exp[-jk(y \sin \Theta_r + z \cos \Theta_r)]$, where $\sin \Theta_0$, $\cos \Theta_0$, $\sin \Theta_r$, and $\cos \Theta_r$ are the direction cosines of the object and reference waves, respectively, $k = 2\pi n/\lambda$ is the modulus of their wave vectors, λ is the wavelength in vacuum, and n is the refractive index of the medium in which they propagate. In the plane $z = x \cot \beta$ of a photographic plate inclined at the angle β to the YZ horizontal plane (Fig. 1(a)), the complex amplitudes of these waves will be given by

$$S = \exp[-jk(y \sin \Theta_0 + x \cot \beta \cos \Theta_0)],$$
$$R = \exp[-jk(y \sin \Theta_r + x \cot \beta \cos \Theta_r)], \quad (1)$$

and the intensity distribution of the standing wave produced by the interference of the waves (1) will be given by

$$I = 2 + \exp\{-jk[y(\sin \Theta_0 - \sin \Theta_r) + x \cot \beta(\cos \Theta_0 - \cos \Theta_r)]\} + \exp\{jk[y(\sin(\Theta_0 - \sin \Theta_r) + x \cot \beta(\cos \Theta_0 - \cos \Theta_r)]\}. \quad (2)$$

In expressions (1) and (2) the factors multiplying x and y in the exponents are the spatial frequencies along the x and y axes of the gratings, which are the projections of the traces of the intersection of the equal-intensity planes of the object, reference, and standing waves with the plane of the photographic plate on the $z = 0$ plane (Fig. 1(b)). Note that these are always the spatial frequencies referred to subsequently.

Let us now consider the reconstruction of the object wave by this grating. Assume the grating to be illuminated at the reconstruction stage by a wave whose wave vector lies in the YZ plane and whose direction of propagation differs from that for the recording process by $\Delta \Theta_r$. By direct substitution, it is easy to establish that the spatial frequencies of the reconstructing wave along both the y and x axes will differ from those of the reference wave in the recording process. As a result, the diffraction angles are altered in both the horizontal and the vertical planes. A similar pattern will be observed if the wavelength of the reconstructing light is altered.

It is easy to show that if, in the reconstruction stage, the spatial frequency along the y axis changes by

$$\Delta \varphi = \sin \Theta_r(\mu \cos \Delta \Theta_r - 1) + \mu \sin \Delta \Theta_r \cos \Theta_r, \quad (3)$$

where $\mu = \lambda/(\lambda + \Delta\lambda)$, then the change $\Delta \Theta_0$ in the diffraction angle in the horizontal plane may be determined from the expression

$$\sin(\Theta_0 + \Delta \Theta_0) = \sin \Theta_0 + \Delta \varphi. \quad (4)$$

This change causes the spatial frequency of the reconstructed wave along the x axis to change by

$$\Delta \Psi_0 = \cot \beta[\cos \Theta_0(\mu \cos \Delta \Theta_0 - 1) - \mu \sin \Delta \Theta_0 \sin \Theta_0]. \quad (5)$$

However, a change in the direction of propagation of the reconstructing wave also alters its spatial frequency along the x axis by $\Delta \Psi_r$, which is determined from expression (5) by replacing ''0'' with ''r.'' According to the fundamental diffraction equation however, the difference in the spatial frequencies of the reconstructing and reconstructed waves should remain constant. It is easily shown that this condition can be satisfied if the diffraction angle in the vertical plane changes by

$$\Delta \beta \approx \Delta \Psi_0 - \Delta \Psi_r \approx (\Theta_r - \Theta_0)\Delta \Theta_r \cot \beta, \quad (6)$$
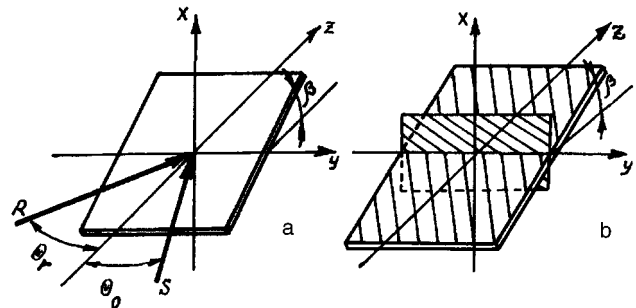

FIG. 1. Diagram showing the recording of a pseudodeep transmission hologram (a) and result of the projection of the traces of intersection of the equal-intensity planes of the wave with the plane of the photographic plate onto the $z = 0$ plane (b).

and in general, the complex amplitude of the reconstructed wave can be described by

$$S_{out} = \exp\{ -jk[y \, \sin(\Theta_0 + \Delta\Theta_0)$$
$$+ x \, \cot(\beta + \Delta\beta)\cos(\Theta_0 + \Delta\Theta_0)]\}. \qquad (7)$$

The conditions for vanishing of the reconstructed wave are determined on the basis of the following reasoning.

1. $\Delta\beta = \beta$. In this case, the reconstructed wave propagates in the plane of the photographic plate.

2. $\Delta\beta = -\beta$. If this condition is satisfied, the function $\cot(\beta + \Delta\beta)$ undergoes a discontinuity and the direction of propagation of the reconstructed wave consequently becomes indeterminate.

If both the direction of propagation and the incident wavelength are altered during reconstruction so that the condition $\Delta\varphi = 0$ is satisfied, the reconstructed wave will obviously propagate in the horizontal plane. Consequently, when an extended nonmonochromatic source is used for reconstruction, noise which cannot be eliminated by a filtering exit slit,[2] is superposed on the reconstructed image.

It is easy to show that the result of interference of the S and R waves recorded in the plane $z = x \cot \beta$ will match (in the sense of its projection on the $z = 0$ plane) the result of interference of certain waves S_1 and R_1 recorded in the plane $z = -x \cot \beta$. The waves S_1 and R_1 should be determined as follows: S_1 constructs the real image of the object and propagates in the direction defined by the angle Θ_r, while R_1 is the reference wave whose direction of propagation is defined by the angle Θ_0. From this reasoning it is clear that because of the difference in the spatial frequencies of the waves R and R_1, when the pseudodeep grating is illuminated by wave R, the reconstructed wave S_1 will propagate outside the horizontal plane.

It is easy to see from expressions (1) and (2) that a reflection grating can also be recorded on a thin pseudodeep hologram and all these conclusions should still apply to this grating. This is confirmed by experiments in which a reflection grating was recorded on FP-R photographic plates using
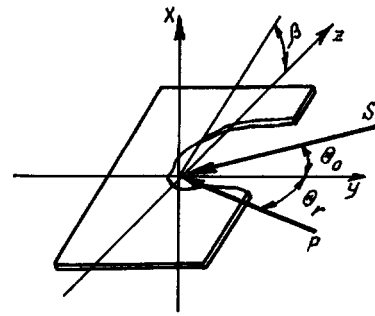

FIG. 2. Diagram showing the recording a pseudodeep reflection hologram in a symmetric dual-beam system.

a symmetric dual-beam system (Fig. 2). The spatial frequency of the grating was governed by the resolution of the plates and was around 1500 mm^{-1} in air. The radiation source was a $\lambda = 0.4416$ μm He–Cd laser and the angle of inclination β of the plate was around 20° from the horizontal plane.

In summary, it has been shown that the object and reference waves, as well as the standing wave formed as a result of their interference, may be represented as equivalent waves whose spatial frequencies are determined by the projections of the traces of intersection of their equal-intensity planes with the plane of the photographic plate onto the $z = 0$ plane of an equivalent vertical grating. The characteristics of the diffraction of waves by a pseudodeep grating are caused by changes in these spatial frequencies as the reconstruction conditions change.

[1] Yu. N. Denisyuk, Pis'ma Zh. Tekh. Fiz. **15**(8), 84 (1989) [Sov. Tech. Phys. Lett. **15**, 323 (1989)].

[2] Yu. N. Denisyuk, Pis'ma Zh. Tekh. Fiz. **18**(2), 15 (1992) [Sov. Tech. Phys. Lett. **18**, 31 (1992)].

[3] Yu. N. Denisyuk and N. M. Ganzherli, Zh. Tekh. Fiz. **60**(11), 154 (1990) [Sov. Phys. Tech. Phys. **35**, 1321 (1990)].

Translated by R. M. Durham

Temperature-concentration dependence of the correlation length of concentration fluctuations in liquid binary systems

E. V. Kalashnikov and A. G. Ambrok

Institute of Problems of Machine Science, Russian Academy of Sciences

An analysis is made of the correlation length of the concentration fluctuations in liquid binary systems over a wide range of temperature and composition. A quantitative relationship is obtained between the correlation length, the concentration, and the temperature. It is shown that the correlation length is determined by regions of different thermodynamic stability of a homogeneous solution, bounded by binodal and spinodal curves. © *1997 American Institute of Physics.* [S1063-7850(97)01602-9]

The correlation length of the density fluctuations describes the interatomic interaction characteristics and behavior of a system. It is a unique measure of the spatial independence of the fluctuations.[1] On transition from a single-component to a binary system, concentration fluctuations begin to play an important role. However, the temperature–concentration dependence of the concentration correlation length ξ is unknown over a wide range of temperature and composition. This indeterminacy of ξ (over a wide range of temperature and composition) means that we cannot assess how the thermodynamic state of a melt influences its transition to a solid. In particular, the approximation of statistically independent concentration fluctuations is usually used when analyzing liquid–solid phase-transition problems.[2] This corresponds to a correlation length comparable with the interatomic spacings,[1] and similar properties of the binary melts regardless of the interatomic interact ion characteristics.

In many binary systems however (in eutectics, for instance[3,4]), at specific temperatures and compositions the liquid state is characterized by a nonuniform concentration structure of the melt. It may be postulated that this concentration nonuniformity is the result of strong correlations between the concentration fluctuations in the melt.[4] This behavior of the melt suggests that the correlation length of the concentration fluctuations will depend on the initial composition of the melt and its temperature.

In order to assess how the correlations of the fluctuations in the liquid system influence the liquid–solid transition, especially vitrification (or amorphization) at various compositions and temperatures[5] and crystallization,[6] it is important to know the temperature–concentration dependence of the concentration correlation length ξ in a binary liquid system.

In order to identify this dependence of ξ, we bear in mind that strong correlations of the fluctuations are typical of critical phenomena.[7] It is known from the theory of interphase critical phenomena[1] that the correlation length of the fluctuations is equal to the "thickness" or concentration profile of the surface layer. For a more detailed analysis of the surface (or interface) the authors of Refs. 8 and 9 developed an approach to calculate the number of monatomic layers forming the surface layer and to take into account instability of a uniform random distribution of atoms of both components in terms of monatomic layers.

The aim of the present paper is to determine the correlation length as a function of composition and temperature, allowing for instabilities in the formation of the interface.

In Refs. 8 and 9 the thickness of the surface layer was defined as the number of monatomic layers t with the concentration $x^{(t)}$ differing from the average bulk concentration x. Since the thickness of the surface layer in a single-component system is equal to the density correlation length,[1]
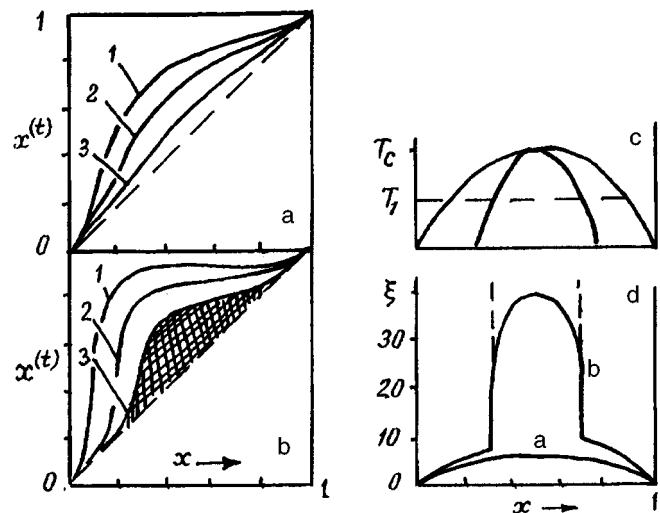

FIG. 1. Distribution of the concentration $x^{(t)}$ of component B over the monatomic layers t and of the correlation length ξ as a function of the concentration x of the same component in the bulk of the system: a–c for various temperatures: a — for $T > T_c$ and b — for $T_1 = T < T_c$. The concentrations are given in atomic fractions: $0 \leqslant x \leqslant 1$; the numbers of monatomic layers t are indicated by the numbers: $t = 1, 2, 3, \ldots$. The shaded areas of the figures correspond to the number of monatomic layers from which the system may be composed. c — boundaries of different thermodynamic stability of the component distribution over the monatomic layers:[8] K — decay cupola, S — spinodal curve; Y, M, L — stable, metastable, and labile states of the uniform distribution of components in terms of monatomic layers; T_c — critical temperatures, $T_1 < T_c$. d — correlation length: curve a corresponds to $T > T_c$, curve b corresponds to $T = T_1 < T_c$, and the dashed line corresponds to an unbounded number of monatomic layers.
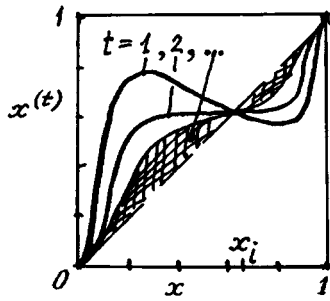
FIG. 2. Distribution of the concentration $x^{(t)}$ of component B over the monatomic layers t as a function of the concentration x of the same component in the bulk for a system with inversion of the distribution at $x = x_i$ for $T < T_c$.

for a binary system the correlation length of the concentration fluctuations is

$$t \approx \xi.$$

In Ref. 8 illustrations are given for a model with a fixed number of monatomic layers. In this paper we present results of calculations for a model with an unbounded number of monatomic layers. Specifically, when an interface (surface) is formed (Figs. 1a and 1b) at temperatures T below the critical temperature T_c, regions of different thermodynamic stability are formed within the random distribution of atoms of both components over the monatomic layers (Fig. 1c). These regions are bounded by decaying cupola curves and by a spinodal curve and are determined by the ratio of the interchange energy (composed of the interaction energies of like and unlike atoms) to the temperature. As can be seen from Figs. 1c and 1d, in the region of stable states of the uniform distribution of components ($T > T_c$), the correlation length ξ is fairly small: $\xi \approx$ 1–3 monatomic layers.

The number of monatomic layers increases as the temperature approaches the critical temperature and falls below it. In the stable and metastable regions the number of monatomic layers increases slowly: two or three monolayers in the stable region and three or four in the metastable region. At corresponding temperatures in the labile region (bounded by the spinodal curve), the value of ξ increases abruptly and is equal to the number of all the monatomic layers assumed in the model. (As an example for comparison, for a model with $t = 40$ monatomic layers the correlation length is $\xi = 40$, Fig. 1d). In fact an unbounded increase in the number

of monatomic layers in the model causes an unbounded increase in their number in the labile region. Thus the correlation length ξ becomes equal to the linear dimensions of the system. In other words, the difference between the surface layer and the bulk disappears. In the range of compositions and temperatures bounded by the spinodal curve, the system is coherent, i.e., completely coupled, and behaves as a single entity.

An interesting situation arises in a system exhibiting inverse behavior of the concentration in the monatomic layers (Fig. 2), which occurs when the surface energies of the pure components are similar. In this case, regardless of temperature, the component distribution over the monolayers of the surface region becomes inverted for the composition x_i. The temperature-concentration dependence of t appears to break down into two intervals. However, the change in the thickness of the surface layer for each concentration interval is identical.

By applying the concept of the instability of a homogeneous solution and studying the surface properties, it has thus been possible to determine the temperature–concentration regions of different behavior of the correlation length in a binary system. In the range of compositions bounded by the spinodal curve, the ''thickness'' of the interface as a quantity characterizing the surface disappears. The system, from being strongly inhomogeneous, becomes coupled, or coherent, and the correlation length becomes equal to the linear dimension of the system.

[1] J. S. Rowlinson and B. Widom, *Molecular Theory of Capillarity* (Clarendon Press, Oxford, 1982) [Russ. transl., Mir, Moscow, 1986].

[2] A. A. Chernov, E. I. Givargizov, Kh. S. Bagdasarov, L. N. Dem'yanets, V. A. Kuznetsov, and A. N. Lobachev, *Modern Crystallography* [in Russian], Vol. 3, Nauka, Moscow (1980).

[3] V. M. Zalkin, *Nature of Eutectic Alloys and the Contact Melting Effect* [in Russian], Metallurgiya, Moscow (1987).

[4] E. V. Kalashnikov, Rasplavy No. 3, 40 (1990).

[5] Yu. S. Tver'yanivich, E. V. Kalashnikov, O. V. Il'chenko, and A. G. Ambrok, Fiz. Khim. Stekla **22**, 291 (1996).

[6] S. A. Kukushkin and D. A. Grigor'ev, Fiz. Tverd. Tela (St. Petersburg) **38**, 1262 (1996) [Phys. Solid State **38**, 698 (1996)].

[7] A. Z. Patashinskiĭ and V. L. Pokrovskiĭ, *Fluctuation Theory of Phase Transitions* (Pergamon Press, Oxford, 1979) [Russ. original, Nauka, Moscow, 1975].

[8] A. G. Ambrok, S. N. Golyandin, and E. V. Kalashnikov, Poverkhnost' No. 4, 137 (1989).

[9] A. G. Ambrok and E. V. Kalashnikov, *Crystal Growth* [in Russian], Vol. 18, Nauka, Moscow (1990), pp. 5–17.

Translated by R. M. Durham

Mechanically-induced electrical effects in natural dielectrics

V. S. Kuksenko and Kh. F. Makhmudov

A. F. Ioffe Physicotechnical Institute, Russian Academy of Sciences, St. Petersburg

An investigation is made of the generation and relaxation of an electric field in natural dielectrics exposed to mechanical loading and applied electric potentials. It is shown that these processes are identical. © *1997 American Institute of Physics.* [S1063-7850(97)01702-3]

It has been established that when dielectrics are subjected to mechanical loading, electric fields are generated in them.[1,2] This phenomenon is well known for piezoelectrics. In Refs. 3 and 4 the generation of electric fields accompanying the deformation of ionic crystals is attributed to the motion of charged dislocations. The treatment of these effects is more complex for dielectrics which do not exhibit the piezoelectric effect and in which the motion of dislocations can be neglected. Such materials especially include various natural dielectrics.

However, mechanically-induced electrical effects in natural materials (rocks) are interesting for practical purposes. It is known that earthquakes are preceded by electromagnetic effects whose nature has not been fully explained. In the present paper we attempt to make a combined study of the electrical polarization observed when dielectrics are subjected to mechanical loading and when weak electric potentials are applied to these samples. The main specimen employed in our investigation was marble, which does not exhibit the piezoelectric effect. The samples were subjected to loading in the range where the motion of dislocations can be neglected.

METHOD OF MEASUREMENT AND EXPERIMENTAL RESULTS

The samples were cut from natural marble in the form of $25 \times 25 \times 40$ mm prisms. The experimental apparatus is shown schematically in Fig. 1. The induced electric potential was measured by a noncontact method using a high-sensitivity electrometer (a dc amplifier with a high input resistance $> 10^{14} \Omega$). The recording element was a probe (Pr) in the form of a 5 mm diameter disk shielded on three sides to reduce noise. The main parameters of the electrometer were: frequency band $f = 10^5 - 10^6$ Hz, time for leakage of induced charge through electrometer entrance slit $\tau = 2 \times 10^4$ s, sensitivity $U_{min} = 0.05$ mV, and zero drift ~ 0.2 sV/min.

The real behavior of the leakage of the induced charge is extremely important in our experiments, as will be shown subsequently. To determine this we carried out the following experiment. The measuring probe was positioned at a distance of 1.5 mm above a metal plate, parallel to the plate. The plate was first grounded and the zero drift was measured for some time. A potential of ~ 2 V was then applied to the plate at time t_1 (Fig. 2). The jump indicated that an induced charge q had appeared at the recording probe of the electrometer and its flow was measured continuously. The half-life for the decay was ~ 15 min, close to the calculated value. It should be noted that the induced charge appeared almost instantaneously at the measuring probe. For our measurements it was sufficient to note that the rise time was ~ 0.1 s and the decay was negligible over 1–2 min.

We shall now discuss the direct measurements on the samples. In the electrical polarization experiment the sample (S) was mounted on a grounded platform and a copper electrode was clamped to the upper face of the sample (Fig. 1). The measuring probe of the electrometer was positioned close to the side surface of the sample, at a distance of 1.5 mm. The electrode was initially grounded and then a 2 V
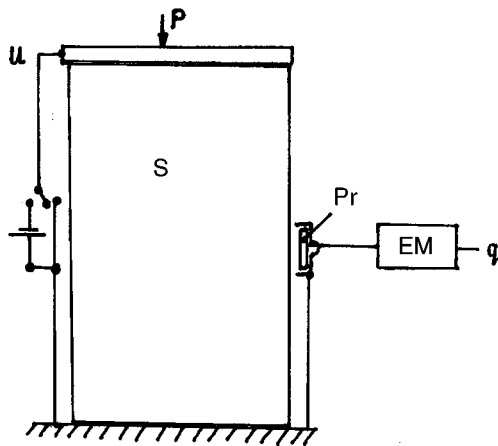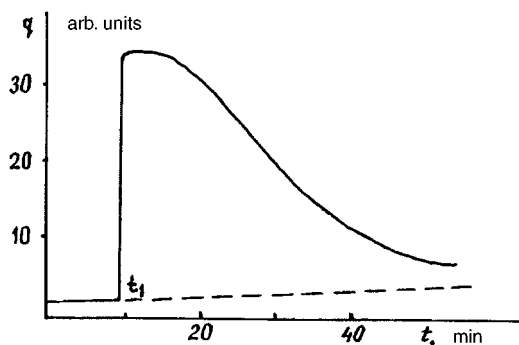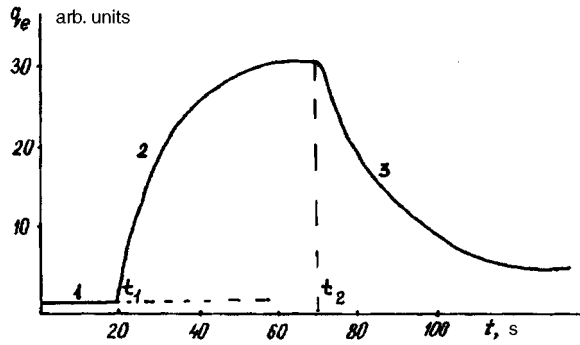
FIG. 1. System for noncontact measurement of the electrification of a sample using a probe (Pr) when a dc voltage (U) is applied to the sample (S) and the sample is subjected to a uniaxial compressive load (P).

FIG. 2. Flow of charge in electrometer.

FIG. 3. Time behavior of induced charge (q_e) when an electric potential $U = 2$ V is applied to the sample.

FIG. 5. Relative time dependence of induced charge: *1* — on application of electric potential and *2* — under mechanical loading.

potential was applied at time t_1 (Fig. 3). The charge induced at the probe increased until it saturated (curve *2* in Fig. 3). When both electrodes were then grounded, the charge relaxed (curve *3* in Fig. 3) and the rise and decay time of the induced charge was the same in both cases.

We shall now consider the electrification of the sample under mechanical loading. As in the first case, the recording probe was placed parallel to the side face of the sample at a distance of 1.5 mm from the surface (Fig. 1) and the zero
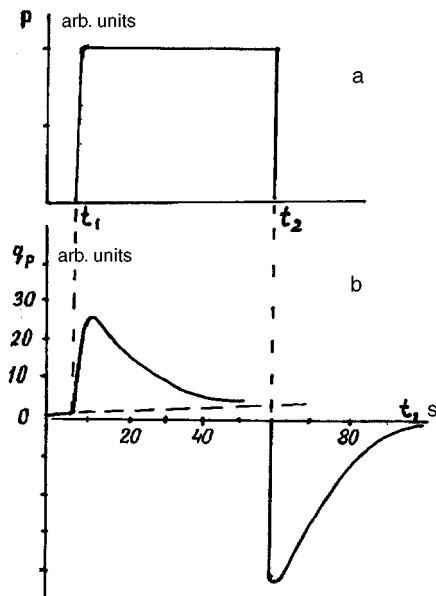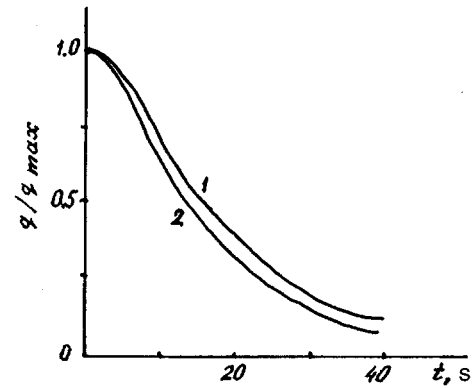
drift was measured for some time. At time t_1 (Fig. 4a) a uniaxial compressive load (P) was applied to the sample and was kept constant for some time. An induced charge (q_p) appeared at the recording probe and then relaxed. When the induced charge had almost disappeared, at time t_2, the load was removed. An induced charge of opposite polarity appeared at the probe and then relaxed with the same half-decay time as that observed after loading.

We shall now compare the relaxation of the induced charge under mechanical loading (unloading) (Fig. 5, curve *1*) and under application of an electric potential (Fig. 5, curve *2*). For purposes of clarity the value of the induced charge (q) is normalized to its maximum in both cases. It can be seen that the decay of the charge is almost identical in both cases. This particularly suggests that the physical nature of the charge carriers causing the relaxation of the electric field is the same under mechanical loading and under an applied electric potential. To a first approximation the relaxation of the induced charge may be described by first-order kinetics. We subsequently propose to investigate the relaxation of the induced charge at different temperatures, which will allow us to estimate the activation energy of the process and discuss the nature of the charge carriers more precisely.

FIG. 4. Sample loading diagram (a) and time variation of induced charge at probe (b).

[1] É. I. Parkhomenko, *Electrification Effects in Rocks* [in Russian], Nauka, Moscow (1968).
[2] V. S. Kuksenko, R. Sh. Kil'keev, and M. I. Miroshnichenko, Dokl. Akad. Nauk. SSSR **250**, 481 (1981).
[3] A. N. Kulichenko and B. I. Smirnov, Fiz. Tverd. Tela (Leningrad) **26**, 11 3294 (1984) [Sov. Phys. Solid State **26**, 1980 (1984)].
[4] V. I. Nikolaev, N. A. Pertsev, and B. I. Smirnov, Fiz. Tverd. Tela (Leningrad) **33**, 93 (1991) [Sov. Phys. Solid State **33**, 51 (1991)].

Translated by R. M. Durham

127   Tech. Phys. Lett. **23** (2), February 1997

V. S. Kuksenko and Kh. F. Makhmudov   127

Properties of the electron channel in single GaInAsSb/p-InAs heterostructures

T. I. Voronina, T. S. Lagunov, M. P. Mikhaĭlova, K. D. Moiseev, S. A. Obukhov, A. E. Rozov, and Yu. P. Yakovlev

A. F. Ioffe Physicotechnical Institute, Russian Academy of Sciences, St. Petersburg

An investigation is carried out on the properties of the electron channel in a broken-gap isotypic type II GaInAsSb/p-InAs heterostructure and their dependence on the doping level of the quaternary solid solution with a donor (Te) and an acceptor (Zn). The Hall mobility decreases (by more than two orders of magnitude) with increasing acceptor concentration. The Shubnikov-de Haas oscillations are observed at low temperatures ($T = 1.5$–20 K) and the electron effective mass is determined ($m_n = 0.026m_0$), along with some other parameters of the heterostructure. © *1997 American Institute of Physics.* [S1063-7850(97)01802-8]

Heterostructures based on solid solutions of GaInAsSb on the isoperiodic substrates GaSb and InAs are the subjects of intense study as prospective materials for infrared sources and photodetectors in the range 2–5 μm.[1-6]

It has previously been determined that the system p-GaIn$_x$AsSb$_y$/p-GaSb ($x,y < 0.2$) are stepped type II heterostructures, while the system p-GaIn$_x$AsSb$_y$/p-InAs ($x,y < 0.2$) is a broken-gap type II heterostructure with an offset of about 60–100 meV between the conduction band and the valence band of the quaternary heterostructure.[7] As a result of the overflow of electrons from the valence band of the wide-gap solid solution into the InAs conduction band of, electron and hole channels are formed at the heteroboundary of this structure. The presence of these channels to large measure governs the transport properties of these heterostructures.

In Ref. 8 we observed for the first time a high electron Hall mobility ($u_H = 50\,000$–$70\,000$ cm^2/V·s) in the isotypic heterostructures p-GaIn$_x$AsSb$_y$/p-InAs ($x \sim 0.17, y \sim 0.22$) with undoped layers of the solid solution, which was explained by the existence of an n-channel at the heteroboundary. The doped solid solutions of this composition always had p-type conduction with a hole concentration $p_{77} = 2 \times 10^{16}$ cm^{-3} and a mobility $u_H = 2000$ cm^2/V·s.

In this paper we describe our studies of the properties of the electron channel and their dependence on the doping level of the solid solution with tellurium and zinc, which were introduced into the flux in amounts 10^{-4}–10^{-2} at.%. The quaternary solid solutions in the Ga$_{1-x}$In$_x$As$_{1-y}$Sb$_y$ ($x = 0.17$, $y = 0.22$) heterostructures were grown by liquid-phase epitaxy to a thickness of 2 μm on high-resistivity p-InAs(100) substrates and had a hole concentration $p_{77} = 2 \times 10^{16}$ cm^{-3} and a conductivity $\sigma = 0.1$ S/cm. Measurements were made of the Hall coefficient R, the electrical conductivity σ, and the Hall mobility u_H. Also studied were the longitudinal and transverse magnetoresistance (the Shubnikov–de Haas effect) at low temperatures ($T = 1.5$–20 K) in moderate magnetic fields up to 50 kOe. Rectangular samples were cut from the GaInAsSb/p-InAs epitaxial structures and six indium contacts were alloyed into the surface of the solid solution.

In Fig. 1 we present the Hall mobility measured for these samples as a function of the amount of impurity introduced into the solid solution. With light doping of the solid solution (Te $< 10^{-3}$ at.%, Zn $< 4 \times 10^{-3}$ at.%) the Hall mobility remained high ($u_H = 40\,000$–$50\,000$ cm^2/V·s) as in the layers of undoped solid solutions. At higher tellurium doping levels (Te $> 10^{-3}$ at.%) the mobility decreased smoothly to $u_H = 10\,000$ cm^2/V·s, and for heavy doping with zinc, (Zn $> 4 \times 10^{-3}$ at.%), the mobility fell off very abruptly, by more than an order of magnitude.

It is interesting that in the samples heavily doped with tellurium or zinc the Hall mobility ($u_H = R\sigma$) was found to depend on the magnetic field (Fig. 2). In the samples with a high concentration of tellurium, the mobility fell at low fields ($H < 5$ kOe), while for $H > 5$ kOe it tended to a constant value $u_H \approx 5000$ cm^2/V·s, which is comparable with the mobility in epitaxial layers of a solid solution of similar composition doped with tellurium.[9] The dependence of the mobility on the magnetic field indicates as a rule that two kinds of carriers take part in the conduction.[10] In the case of heavy tellurium doping, these are probably the high-mobility electrons in the channel and current carriers (in addition to the electrons) with a lower mobility in the epitaxial layer, which as a result of overcompensation by donors becomes an n-type material with a mobility $u_H \sim 5000$ cm^2/V·s.

When the solid solution is heavily doped with an acceptor (Zn $> 4 \times 10^{-3}$ at.%) the falloff in the mobility with increasing field is associated with a sharp decrease in the Hall coefficient to the point where it reverses sign (Fig. 2, sample 5). This dependence may observed in the simultaneously participation in the conductivity of two kinds of charge carriers, which differ not only in their mobility, but also in their sign.[9] We suggest that in addition to an electron channel in the heterostructure a hole channel also begins to appear, and that the role of the electron channel in controlling the conductivity decreases. This may be explained by a decrease in the electron density in the channel due to the trapping of the carriers in potential relief wells at the heteroboundary. The decrease in the mobility may be due also to the mutual compensating effect of the electrons and the holes at the heteroboundary.

In undoped and lightly doped samples, where the high electron mobility is observed at $T = 77$ K, these mobility val-
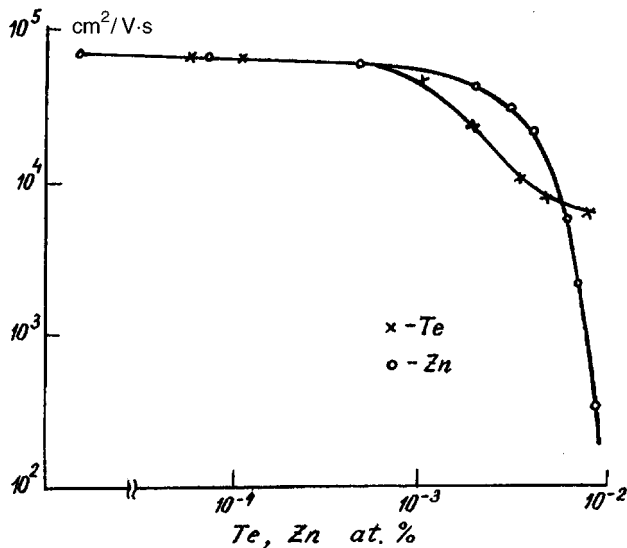
FIG. 1. Hall mobility in GaInAsSb/p-InAs structures versus the impurity concentration (tellurium and zinc) in the solid solution.

ues are retained down to helium temperatures. This behavior in the mobility is characteristic of structures in which the carrier scattering mechanism is governed only by the perfection of the quantum well (scattering by nonuniformities in the heteroboundary).

At $T = 1.5$–20 K magnetoresistance oscillations are observed in these samples (the Shubnikov–de Haas effect) in magnetic fields up to 50 kOe. From the temperature dependence of the oscillation amplitude we were able to determine the effective mass of the charge carriers ($m^* = 0.026m_0$), which is equal to the effective mass of the electrons in n-InAs—$m^* = 0.026m_0$. This result shows that the n-channel is located on the p-InAs side. The small effective mass can be explained by the large width of the quantum well on the InAs side (more than 150 Å), which leads to a lower electron trapping energy and a low effective mass.[11]

From the oscillation period we also found the two-dimensional electron concentration in the channel to be $N_S \sim 10^{11}$ cm^{-2} and a well width of ~ 400 Å. The Dingle temperature was found to be $T = 7$–10 K at $T = 4.2$ K, which corresponds to a broadening of the quantum levels by 2–3 meV.

In summary, the experimental results that we have obtained support the supposition that in broken-gap type II GaInAsSb/p-InAs heterostructures an n-channel is formed at the boundary with the InAs side, with a high mobility that is retained with light doping of the epitaxial layer either with donors (tellurium) or with acceptors (zinc). At high acceptor doping levels the solid solution exhibits a sharp falloff in the mobility in the structure, due both to the depletion of the n-channel through trapping of the carriers in potential relief wells, and as the result of the mutual compensation of electrons and holes at the heteroboundary itself.
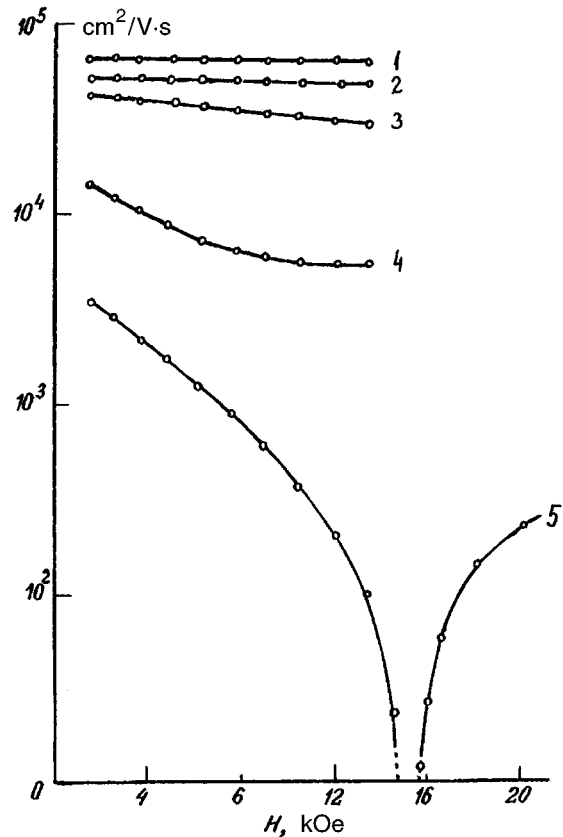

FIG. 2. Hall mobility in the GaInAsSb/p-InAs structures versus the magnetic field strength: 1 — undoped solid solution; $2, 4$ — solid solution doped with zinc; $3, 5$ — solid solution doped with tellurium.

[1] A. N. Baranov, B. E. Dzhurtanov, A. N. Imekov, A. A. Rogachev, Yu. M. Shcherbakov, and Yu. P. Yakovlev, Fiz. Tekh. Poluprovodn. **20**, 2217 (1986) [Sov. Phys. Semicond. **20**, 1385 (1986)].

[2] H. K. Choi, G. W. Turner, and S. L. Eglash, Appl. Phys. Left. **64**, 2474 (1994).

[3] Yu. P. Yakovlev, A. N. Baranov, A. N. Imenkov, and M. P. Mikhailova, SPIE **1510**, 120 (1991).

[4] K. D. Moiseev, M. P. Mikhaĭlova, O. G. Ershov, and Yu. P. Yakovlev, Fiz. Tekh. Poluprovodn. **30**, 389 (1996) [Semiconductors **30**, 223 (1996)].

[5] X. Gong, H. Kan, T. Yamaguchi, I. Suzuki, M. Aogama, M. Kumagawa, N. L. Rowell, A. Wang, and R. Rinfret, Jpn. J. Appl. Phys. **33**, 1740 (1994).

[6] M. P. Mikhailova, and A. N. Titkov, Semicond. Sci. Tech. **9**, 1279 (1994).

[7] M. P. Mikhaĭlova, I. A. Andreev, T. I. Voronina, T. S. Lagunova, K. D. Moiseev, and Yu. P. Yakovlev, Fiz. Tekh. Poluprovdn. **29** 678 (1995) [Semiconductors **29**, 353 (1995)].

[8] T. I. Voronina, T. S. Lagunova, M. P. Mikhaĭlova, K. D. Moiseev, and Yu. P. Yakovlev, Fiz. Tekh. Poluprovodn. **30**, 985 (1996) [Semiconductors **30**, 523 (1996)].

[9] T. I. Voronina, B. E. Dzhurtanov, T. S. Lagunova, and Yu. P. Yakovlev, Fiz. Tekh. Poluprovodn. **25**, 283 (1991) [Sov. Phys. Semicond. **25**, 171 (1991)].

[10] C. Hilsum and A. C. Rose-Innes, *Semiconducting III–IV Compounds* (Pergamon Press, Oxford, 1961) [Russ. transl., IL, Moscow, 1963)].

[11] H. J. von Bardeleben, J. G. Jia, M. G. Manasren, and C. E. Stuz, Appl. Phys. Lett. **62**, 60 (1993).

Translated by J. R. Anderson

129   Tech. Phys. Lett. **23** (2), February 1997

Voronina *et al.*   129

Operation of an electron interferometer with photon illumination of the biprism tip

A. N. Ageev, Yu. M. Voronin, I. P. Demenchonok, and Yu. V. Chentsov

A. F. Ioffe Physicotechnical Institute, Russian Academy of Sciences, St. Petersburg

A study is made of electron diffraction by an optical fiber, which plays the role of the electrode of a Fresnel–Mollenstedt biprism. Irradiation of the electrode with the radiation from a low-power laser causes a change in the diffraction pattern. A tentative explanation for this effect is proposed. © *1997 American Institute of Physics.* [S1063-7850(97)01902-2]

During experiments on the electronic Fresnel–Mollenstedt biprism,[1] which were carried out for the purpose of investigating the magnetic vector potential of a light beam,[2] it was found that under certain conditions the central electrode of the biprism became charged by fast electrons and leakage of the charge under laser illumination.

The electronic biprism was placed in the chamber of an electron microscope between the intermediate and the projection lenses (Fig. 1). The electron energy was 75 keV, and the current density in the region of the biprism was controlled between 10^{-1} and 10^{-6} A/cm^2.

The central electrode of the biprism was a tip *3* made from a single-mode optical fiber by local heating and fast drawing. The diameter of the thinnest part of the tip was 0.5–2.0 μm with a vertex angle of 5–10°. The potential of the tip was supplied by an external source U, and to create surface electrical conductivity a layer of chromium 10–50 nm thick was vacuum-deposited on the tip.

The tip was irradiated with the light from a 5 mW He–Ne laser. To increase the energy density the light was focused by a 9×0.2 microscope objective *1* to a point 1–2 μm in diameter. The tip was placed at the focal point of the objective, and the accuracy of its location was monitored by the optical diffraction pattern of the tip projected on the monitor screen *2*.

A dark electron projection of the tip *5* was observed on the screen of the electron microscope *4* at a magnification of 500 (Fig. 2), which was provided by a projection lens. Photographic film *6* was placed over the screen and was exposed when the screen was lifted out of the way.

During the electron irradiation, particularly with a high current density, the metallization layer near the apex of the tip was sometimes damaged. When the electrons impinged on the glass it charged up, and the destruction of the conducting layer made it difficult for the charge to leak off. The potential at the apex of the tip was set independently of the potential applied to the external source, and in the first approximation the charge was proportional to the current density of the electron beam.

The magnitude and sign of the potential on the tip relative to the potential on the chamber walls could be assessed from the shape and dimensions of the electron projection. When the tip had a potential different from the wall potential it would distort the trajectories of the electrons, which affected the size and shape of the projection. A negative potential would repel the electrons, and a positive potential

attract them, so that the size of the projection correspondingly increased or decreased. For high positive potentials the fluxes of electrons passing the two sides of the tip would merge, and a band of enhanced brightness would appear on the screen (Fig. 2a,c). The length of the projection was markedly reduced (Fig. 2c), and near the apex appeared a pattern similar to part of the image of the caustic.

It can be seen from the pattern of the electron projection that the tip is always charged positively; i.e., the secondary emission coefficient is greater than unity. Evidently, this is explained by the grazing incidence of the electrons on the side surfaces of the tip.

When the tip was illuminated by a laser the induced charge leaked out to the metallized part of the tip by virtue of the induced photoconductivity to equalize the potential along the length of the tip. This is indicated by the electron projection pattern (Fig. 2b,d). The change in the size of the projection can be seen quite well in Fig. 2e, where the photograph shows the projection when the tip is not illuminated and when it is. In the dark the magnitude and distribution of the charge along the fiber are largely determined by the magnitude and distribution of the electric current density.

The charge leakage that occurs with illumination could be controlled by placing the tip directly at the fine focus of the laser beam, since the tip did not charge up when the placement was optimum.
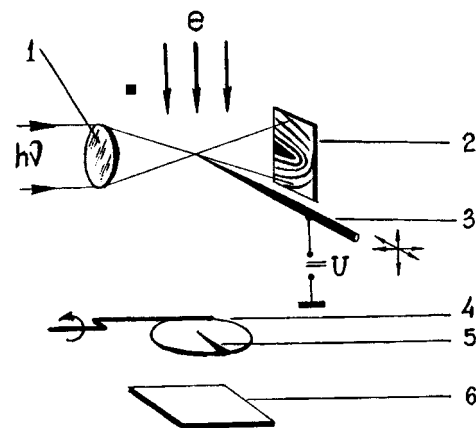

FIG. 1. Diagram of how the tip is irradiated by electrons and light: *1* — microscope objective, *2* — monitor screen for the light, *3* — central electrode-tip, *4* — luminescent screen, *5* — dark projection of the tip, *6* — photographic film.
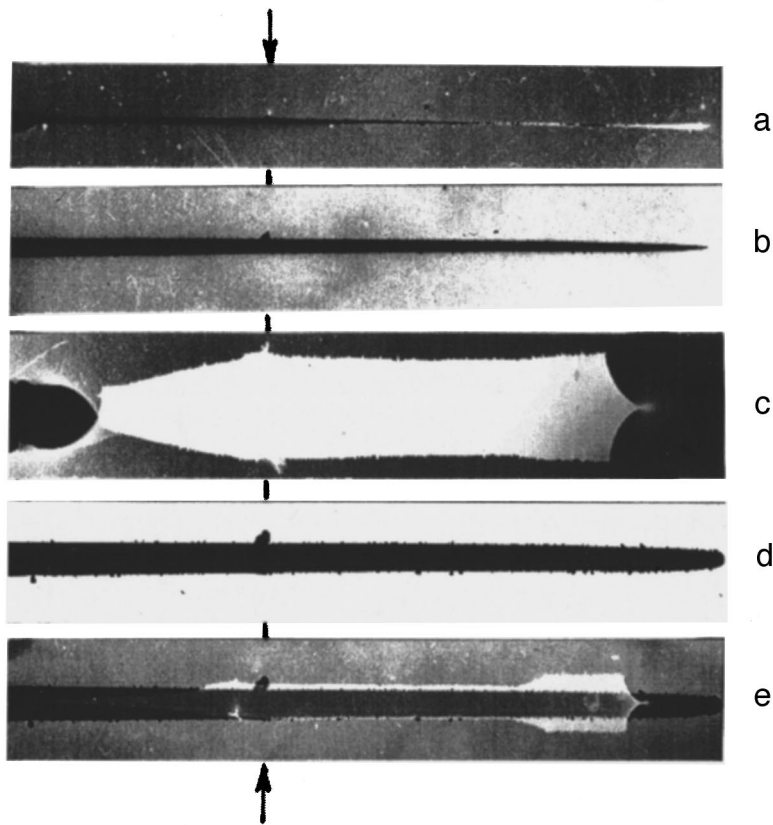
FIG. 2. Dark electron projection of the tip: a — $U=0$, without light, b — $U=0$, with illumination, c — $U=-30$ V, without light, d — $U=-30$ V, with light, e — $U=-30$ V, with and without light. The arrows show a charged particle on the tip.

The charge leakage from the insulating surface induced by the laser beam can be used in an electron microscope and electron diffraction equipment to neutralize the surface charge of poorly conducting objects together with beams of slow electrons.

On the dark electron projections we also observed bending of the tip of a freely-hanging, very thin glass fiber with a diameter of about 1 μm when the laser light passed through it. The fiber was prepared and installed in the same manner as a tip. The light from the 5 mW laser was introduced into the end of the initial fiber by means of a 9×0.2 microscope objective. The curvature of the fiber was proportional to the intensity of the light flux and could be repeated reproducibly. The greatest deflection of the tip was 50 μm, which corresponded to an angle of inclination of about 20°. The reason for the inclination is presumably heating of the fiber by the energy of the light passing through it, since the power density in the thinnest part of the fiber could exceed 10^3 W/cm. The heating could also be caused by the lack of any heat loss in the vacuum through convection and the low thermal conductivity of the fiber.

[1] G. Molenschtedt and H. Ducker, Phys. **245**, 377 (1956).
[2] Yu. V. Chentsov, Yu. M. Voronin, I. P. Demenchonok, and A. N. Ageev, Opt. Zh. No. 8, 55 (1996).

Translated by J. R. Anderson

Q-switching in single-heterojunction lasers and generation of ultrahigh-power picosecond optical pulses

G. B. Venus, I. M. Gadzhiev, A. M. Gubenko, E. L. Portnoĭ, and A. A. Khazan

A. F. Ioffe Physicotechnical Institute, Russian Academy of Sciences, St. Petersburg

Q-switching has been obtained for single-heterojunction lasers. The ultrafast saturable absorber in the laser cavity is created by implantation of high-energy heavy ions. The peak power generated by the lasers in a 150 μm stripe width is 380 W with a pulse length of 40 ps. © *1997 American Institute of Physics.* [S1063-7850(97)02002-8]

The range of application of picosecond light pulses has greatly expanded in recent years, and new direction in their use have arisen, for example, laser mammography, and high-resolution laser ranging. Such a situation calls for the development of small semiconductor light sources of picosecond pulses with peak power approaching that of solid-state lasers. High optical power in a picosecond pulse, which is the most important parameter for applications of this type, requires the design of semiconductor lasers considerably different from the optimal design of high-power cw lasers. In this connection, the purpose of this investigation was to devise and design a diode laser that would provide a new level of power in picosecond light pulses in Q-switched operation.

In Q-switched operation, the simplest means of increasing the output energy in the light pulses of lasers is to increase the stored energy in the laser cavity until the instant the optical shutter is triggered. In semiconductor lasers the accumulation of energy is directly related to the number of nonequilibrium carriers existing at the instant the saturable absorber is triggered and to the degree of modulation of the carrier concentration. The degree of modulation is determined by the quality of the saturable absorber introduced into the cavity of the semiconductor laser. An increase in the volume of the active layer increases the number of nonequilibrium carriers in the laser cavity. This can be thought of in terms of an increase in the physical dimensions of the active layer or an increase in the volume of the active layer in energy space, i.e., an increase in the concentration of nonequilibrium carriers.

The standard way to increase the volume of the active layer and thus increase the pulsed power is to use multisection quantum-well lasers with a broad stripe of a complex shape, and with a reverse-biased section of saturable absorber.[1,2] Further increase in the volume is possible by going from quantum-well structures to bulk materials. Here the maximum thickness of the active region with which it is still possible to retain lasing in the zeroth mode can be obtained with lasers having an asymmetric waveguide. Of the commercial lasers available today, the best ones for this purpose are lasers based on a single-heterojunction (SH lasers) with an active region about 2 μm thick. Similar structures have been used previously for generating high-power single light pulses under special pump conditions of current and temperature.[3,4]

To obtain stable Q-switching in a diode laser it is nec-essary to produce a high-efficiency saturable absorber, which in the case of a SH laser is not possible using the multisection design with reverse-biased sections of saturable absorbers, standard with quantum-well lasers. One of the reasons for this situation is the inadequate speed of existing saturable absorbers, since the space-charge region is no larger than 0.1 μm, and the speed of response is dictated by the lifetime of the nonequilibrium carriers in the active layer with a thickness of about 2 μm, which corresponds to a few nanoseconds. A large increase in speed is possible through the technique of implantation of high-energy heavy ions, which we have developed over a period of years.[5,6] We believe that this method provides the best results, particularly for lasers with a bulk active layer, since in this case, in addition to the extremely short lifetimes in the region of the absorber, it also gives the greatest degree of modulation of the nonequilibrium carrier concentration in the active layer. We have obtained new levels of power output in picosecond optical pulses with Q-switched operation by applying this technique to commercial SH lasers.

In our experiments we used LD-60 SH laser diodes with an active region 70 μm wide and LD-62 lasers with an active region 70 μm wide, manufactured by Laser-Diode Inc. The mirrors on these lasers were irradiated with different kinds of ions (N^+, O^+, Ar^+) at an energy of 10–50 MeV and doses in the range 5×10^{10} to 4×10^{11} ions/cm^2. The energy of each type of ion was selected so that the penetration depth was at least 6–8 μm for a cavity length of 350–400 μm. Preliminary investigations showed that the implantation of the heavy ions gives a region of saturable absorber that has an ultrafast response and is stable against optical annealing.[5]

In addition to producing the saturable absorber in the region of the mirrors, the implantation method was used for shaping the directional diagrams of the picosecond lasers in the plane parallel to the $p-n$ junction. The implantation was done with nitrogen ions to a dose above 10^{12} ions/cm^2 on the sides of the LD-60 laser diodes with a contact width of 70 μm. The ion energy (and the corresponding penetration depth in the material) was selected so as to form a stripe of maximum width providing stable lasing in the zeroth mode in the waveguide with current confinement over the entire range of the single-peak regime.

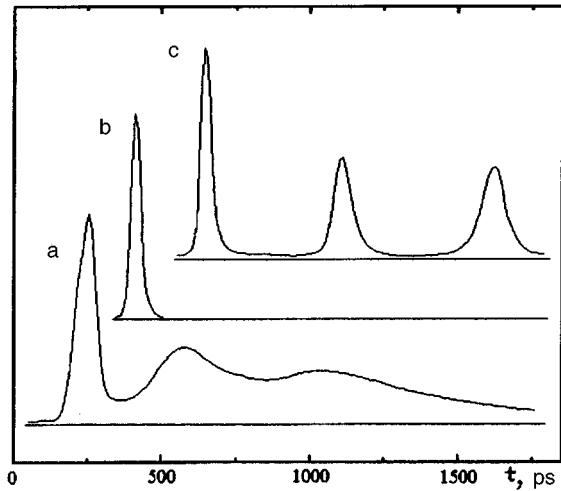To obtain peak generation, the lasers were pumped with

FIG. 1. Shape of the optical pulse from an LD-62 SH laser; a — before implantation, $I = 18.5$ A; b — after implantation of 17.6 MeV N^{4+} ions with a dose of 1.5×10^{11} cm^{-2}; $I = 1.3 I_{th} = 18.5$ A and c — $I = 2.7 I_{th} = 38.4$ A.
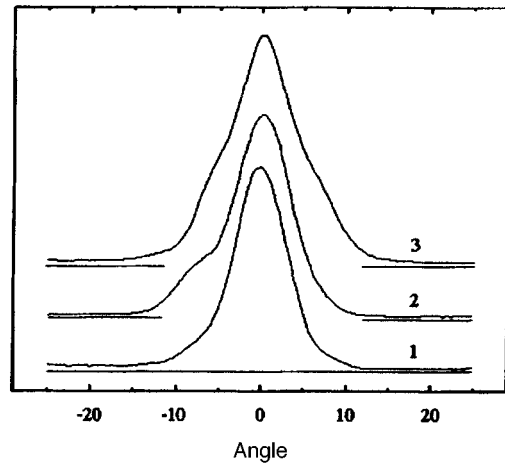

FIG. 2. Changes in the far field of the laser in the plane of the $p-n$ junction for a SH-laser of stripe design for single-pulse lasing with different pump currents. 1 — $I = 1.1 I_{th} = 7.8$ A, $P_{opt} = 6.3$ W; 2 — $I = 1.5 I_{th} = 10.6$ A, $P_{opt} = 24$ W, 3 — $I = 1.9 I_{th} = 13.5$ A, $P_{opt} = 38$ W.

2-ns pulses with an amplitude to 50 A and a repetition rate up to 100 kHz. After implantation the pulsed threshold current increased by a factor of 2.2–3.1, depending on the irradiation dose and the energy and type of ion. With irradiation by N^{4+} ions with an energy of 17.2 MeV and doses of 1.5×10^{11} ions/cm^2 the threshold current for the LD-62 SH laser (150 μm width of the lasing region) was in the range 13.8–14.8 A. Figure 1 shows how the optical pulse of the SH lasers and has changed form after implantation. It can be seen from this curve that we have succeeded in obtaining stable Q-switched lasing of the SH lasers despite possible limitations associated with the strong asymmetry of the waveguide in these structures. The pulsed optical power in a single peak reaches 380 W for the LD-62 lasers (lasing region 150 μm) and 45 W for lasers with the zeroth mode for a pulse length from 40 to 45 ps. The distribution of the far-field in the plane parallel to the plane of the $p-n$ junction for lasers with current confinement, prepared by implantation from the side by the method described here, is shown in Fig. 2. The effective width of the lasing region, determined from the diffraction limit, corresponds to a stripe 14 μm wide.

The pulsed power density on the mirror for the stripe laser is about 125 MW/cm^2, and for the lasers with a wide lasing region it is about 105 MW/cm^2. Our experiments have shown that the mirrors of the original structure do not dete-

riorate at these high radiation power densities because of the short picosecond duration of the light pulses. The saturable absorber we have developed is also stable against optical annealing at these high power densities. This is indicated by the complete reproducibility of the results of measurements of the pulsed power and the threshold currents in the single-peak regime for the lasers operating for several hundred hours.

[1] B. Zhu, I. H. White, K. A. Williams, and F. R. Laughton, IEEE Photonics Technology Letters **8**, 503 (1996).
[2] Z. Jiang, H. K. Tsang, W. Wang, Z. Wang, X. Wang, and Q. Wang, *15th International Semiconductor Laser Conference,* 1996. Haifa, Israel, Th. 1.3., pp. 159–160.
[3] F. Volpe, V. Garfinkel, J. Sola, and G. Kompa, *Conference on Laser & Electro-Optics (CLEO-9)*, Anaheim, California USA, May 1994.
[4] S. Vainshtein, V. Rossin, A. Kilpela, J. Kostamovaara, R. Myllyla, and K. Maatta, IEEE J. of Quantum Electron. **QE-31**, 1015 (1995).
[5] E. L. Portnoĭ, N. M. Stel'makhm and A .V. Chelnokov, Piz'ma Zh. Tekh. Fiz. **15**(11), 44 (1989) [Sov. Tech. Phys. Lett. **15**, 432 (1989)].
[6] E. Portnoi, E. Avrutin, and A. V. Chelnokov, in *Proceedings of the Joint Soviet-American Workshop on the Physics of Semiconductor Lasers*, Leningrad, May 20–June 3, 1991. *AIP Conference Proceedings,* No. 240., pp. 58–66 (New York 1991).

Translated by J. R. Anderson

Diffraction pattern of electrons scattered quasi-elastically by adsorbed fullerenes

M. V. Gomoyunova, I. I. Pronin, and N. S. Faradzhev

A. F. Ioffe Physicotechnical Institute, Russian Academy of Sciences, St. Petersburg

The diffraction patterns are calculated for 2 keV electrons scattered quasi-elastically by C_{60} molecules adsorbed on a solid surface. It is shown that when the molecules are bound to the substrate strongly enough the symmetry of these patterns reveals uniquely the orientation of the adsorbed fullerenes. A new and effective method that takes into account phenomenologically the focusing of the scattered electrons is proposed for modeling the diffraction patterns
© *1997 American Institute of Physics.* [S1063-7850(97)02102-2]

The focusing of intermediate-energy electrons (the forward-focusing effect), in which the electrons emitted by a crystal are concentrated along the closest-packed chains of atoms, is widely used in the structural analysis of surfaces. This is the phenomenon that underlies the method of diffraction of photoelectrons or Auger electrons,[1–3] and also the diffraction of back-scattered electrons,[4,5] which give information on the object in real space. In the most recent articles[6,7] these methods were used to determine the orientation of C_{60} molecules adsorbed on the surfaces of single crystals. This is possible because long-range order is not required to form these diffraction patterns, and if all the adsorbed fullerenes in the ensemble have a common preferred orientation, the experimentally observed pattern characterizes the individual molecules.

This paper reports a continuation of the work of Ref. 7, in which the orientation of fullerenes was determined from an analysis of the spatial distribution of quasi-elastically scattered electrons. The actual form of the diffraction pattern simplified the solution of the problem, reducing it to an analysis of only one of the possible orientations of the adsorbed molecules. Here we analyze the most common case and model the diffraction patterns for all the most probable orientations of the adsorbed C_{60} molecules. In addition, we propose a new method of modeling the diffraction patterns from individual fullerenes, which speeds up the calculations by a factor of a hundred compared the previously used model.

Let us first consider the results obtained for 2-keV electrons in the cluster model of singly scattered electron plane waves we used before.[7] In the first step the coordinates of the atoms of the object (fullerene with a particular orientation relative to the substrate surface) are given in real space. Each of these atoms can take part in the backscattering of the electrons incident on the fullerene, and therefore can be considered as a source of an electron wave contributing to the diffraction pattern. As the electrons penetrate into the interior of the fullerene the probability of excitation of such sources is assumed to decay exponentially as $\exp(-z/\lambda)$, where λ is the mean free path of the electrons before inelastic scattering, which is calculated by the formula given in Ref. 8. The next step is to examine the focusing of the electrons as they are emitted by the sources, caused by their interaction with other atoms of the fullerene during their emission into the vacuum.

For this purpose the necessary data for the scattering amplitudes and the phase shifts were obtained by extrapolation of the calculated values tabulated in Ref. 9. The contributions to the pattern from the individual sources were calculated by summing the amplitudes of the forward and reverse scattered electron waves. The total intensity of the model pattern for each direction of detection of the electrons was obtained by incoherent summation of the partial contributions from all the fullerene atoms. The calculations were carried out over the entire backscattering hemisphere with a step of 1° in the polar and azimuthal angles.

We analyzed five of the most probable orientations of the adsorbed C_{60} molecule for which the fullerene is attached to the surface by a hexagon, a pentagon, an edge between two hexagons, an edge between a pentagon and a hexagon, or only one of the atoms of the molecule. The results are illustrated in Fig. 1, which shows the diffraction patterns of the first three cases along with the corresponding orientation of the molecule. For convenience of comparing these with experiment (for which the contribution of the substrate must first be removed[7]) the numerical data are shown in the form of a two-dimensional picture of the intensity distribution of the reflected electrons along the polar and azimuthal emission angles and are displayed in stereographic projection. The center of the circle corresponds to the normal to the substrate surface, and the outer circle to the emission of electrons tangent to the surface. We used a linear gray scale, in which the maximum signal corresponds to white and the minimum to black.

The calculations give distinct diffraction patterns with prominent features characteristic of each of the orientations. An analysis of these patterns shows that in all the cases the most intense diffraction spots are formed along the edges of the adsorbed molecules, i.e., along the directions corresponding to the minimum distance between the emitting and scattering atoms, where the conditions for focusing the electrons are optimum. In addition to these maxima in the reflected electrons, we also see weak features in the diffraction patterns, corresponding to the directions along the inner diagonals of the icosahedron. We should point out the difference in the symmetry of the Kikuchi patterns. The symmetry of the pattern is defined by the order of the rotation axis of the molecule coinciding with the normal to the substrate surface. When the C_{60} molecule is is attached to the substrate by a
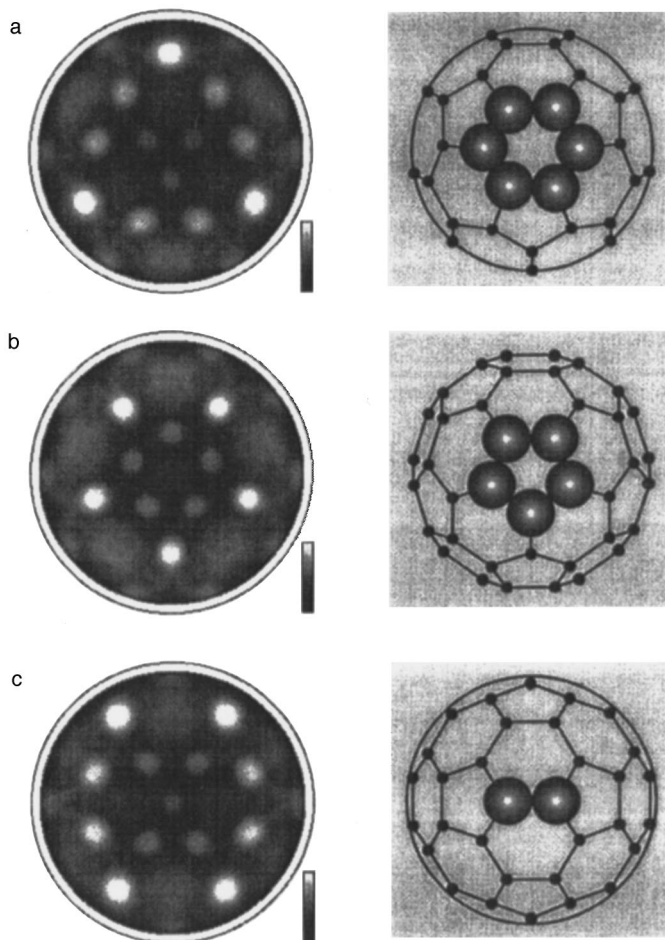
FIG. 1. Diffraction patterns obtained in the plane-wave approximation by the single-scattering cluster model for some probable orientations of the C_{60} molecule on a solid surface, shown to the right. The molecules are attached to the substrate by: a — a hexagonal face, b — a pentagonal face, c — an edge between a pentagon and a hexagon.

hexagon, this axis has threefold symmetry. When the molecule is adsorbed on the surface on a pentagonal face the symmetry is fivefold, and when the molecule rests on an edge the rotational symmetry is twofold. In this way the geometry and the symmetry of the diffraction pattern is uniquely linked to the orientation of the adsorbed fullerene relative to the substrate.

The direct manifestation of the internal structure of the molecule in the diffraction pattern allows us to use an extremely simplified model for calculating the pattern. In this calculation we take into account phenomenologically the coherent scattering events only from the atoms lying near the line connecting the emitter with the scattering direction along which the intensity of the pattern is being calculated. It

is assumed that the intensity of this scattering is inversely proportional to the distance between the source and the scattering atom, and its angular profile is a Gaussian with a constant dispersion; then the contributions from all the atoms in the fullerene are summed up.

Using this model, we also carried out calculations for the five orientations enumerated above for the adsorbed molecule. The results of one of them is shown in Fig. 2a. The diffraction pattern there refers to the case where the fullerene is attached to the substrate by only a single atom. In the same figure we show for comparison the analogous pattern obtained in the single-scattering cluster model (Fig. 2b). It can be seen that the symmetry and the overall shape of these patterns are quite different from those shown in Fig. 1, which
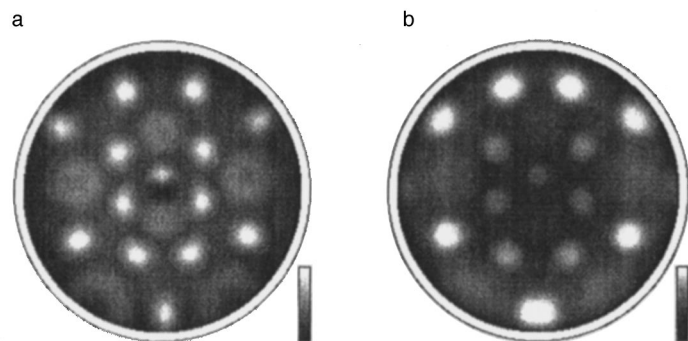

FIG. 2. Calculated diffraction patterns obtained with two models: a — a model that takes into account phenomenologically the focusing of the electrons by the atomic chains, b — in the plane-wave approximation by the single-scattering cluster model. The adsorbed C_{60} molecules are attached to the surface by a single atom.

again is evidence for the correctness of the conclusions drawn above. A point that merits attention is the close proximity of the results obtained by the different methods. In fact, the arrangement of all the bright spots is the same in Figs. 2a and b. The differences mainly concern the intensity ratios of the weakest spots. Similar results were also obtained for the other cases. It can thus be concluded that the proposed model takes into account properly the principal factors that bear upon the formation of the pattern. Since it is possible to use this model to calculate the complete diffraction pattern of fullerene in less than a minute (using a 80486 PC), this approach should be very promising for calculations with a large number of variable parameters. This model can also be used to determine the orientation of adsorbed fullerenes more complicated than C_{60}. It is also quite applicable for studying the localization of metal atoms in fullerenes.

[1] C. S. Fadley, *Synchrotron Radiation Research: Advances in Surface Science*, V. 1: *Techniques*, ed. by R. Z. Bacharach (Plenum Press, New York 1992) Ch. 9. pp. 421–518.

[2] W. F. Egelhoff, Jr., *Crit. Rev. Solid State Mater. Sci.*, 1990. V. 16., No. 3, pp. 213–235.

[3] S. A. Chambers, Surf. Sci. Rep. **16**, 261 (1992).

[4] M. Erbudak, M. Hochstrasser, and E. Wetli, Mod. Phys. Lett. B. **8**, 1759 (1994).

[5] M. V. Gomoyunova, I. I. Pronin, and N. S. Faradzhev, Zh. Éksp. Teor. Fiz. **110**, 311 (1996) [JETP **83**, 168 (1996)].

[6] R. Fasel, P. Aebi, R. G. Agostino, D. Naumovic, J. Osterwalder, A. Santaniello, and L. Schlapbach, Phys. Rev. Lett. **76**, 4733 (1996).

[7] M. V. Gomoyunova, I. I. Pronin, and N. S. Fardzhev, Fiz. Tverd. Tela (St. Petersburg) **38**, 2549 (1996) [Phys. Solid State **38**, 1398 (1996)].

[8] M. P. Seah, Surf. Interf. Anal. **2**, 85 (1985).

[9] M. Fink and J. Gregory, Atom. Data Nucl. Data Tables **14**, 39 (1974).

Translated by J. R. Anderson

New semiconductor devices based on a special metal−insulator−semiconductor structure for measuring the energy (dose) of electromagnetic and nuclear radiation

P. G. Kasherininov and A. N. Lodygin

A. F. Ioffe Physicotechnical Institute, Russian Academy of Sciences, St. Petersburg

This article describes and studies a new type of device for quantitative measurements of radiation energy. © *1997 American Institute of Physics.* [S1063-7850(97)02202-7]

The energy (dose) of electromagnetic and nuclear radiation is widely used in science and technology, but practical devices for measuring it directly have been scarce. Semiconductor photoelectric devices form signals proportional to the intensity of the radiation, but no principle has yet been developed for recording directly the radiation energy (or dose).

In this article we describe a new type of semiconductor device based on new principles for radiation dosimeters, which form electrical signals at the output directly proportional to the energy (dose) of the radiation being detected (light, x rays, gamma rays, etc). In these devices the energy (dose) of the radiation is converted to a time sequence of short current pulses. With steady, uniform irradiation of the dosimeter the energy (dose) of radiation falling on the dosimeter during the time between two current pulses is determined only by the voltage applied to it, and is independent of the intensity of the radiation. The total radiant energy incident on the surface of the dosimeter over a given interval of time is given by the number of current pulses in the external circuit in that time interval. If an individual part of the dosimeter surface is irradiated the repetition rate of the current pulses is proportional to the intensity of this flux on the irradiated surface. If several spatially distributed radiation fluxes are simultaneously incident on the dosimeter surface, then the device generates current pulses independently according to all of these fluxes individually with repetition rates proportional, respectively, to the intensities of these fluxes. The dosimeter consists of a special kind of metal−insulator−semiconductor structure on an insulating wide-gap crystal. The operation of this dosimeter is described in the following paragraphs.

When the structure is irradiated at the crystal−insulator interface an electrical charge of the corresponding sign accumulates there and causes redistribution of the applied voltage between the layers of the structure. In structures with a solid insulator this process occurs until the electric field is completely expelled from the crystal.[1−3] As shown in Ref. 4, the energy (dose) of radiation required does not depend on the intensity of the radiation, but is determined by the voltage V_0 applied to the structure.

In this way, the structure is a kind of radiation dosimeter, in which a certain fixed amount of energy (dose) of radiation is converted into a change in the distribution of the applied voltage between the layers. However, the detection of the energy (dose) of radiation is only a one-time operation: it is then necessary to get rid of the charge accumulated in the crystal to prepare it for the next energy measurement. To make a device that can record continuously the energy (dose) impinging on it one must devise a process for redistributing cyclically the voltage between the layers of the structure and find a means to record reliably each of these cycles. Such conditions can be realized in the structure described here if the conductivity of the insulator depends nonlinearly on the electric field in it, specifically, if the insulating layer converts discontinuously into a high-conductivity state when a critical electric field is set up in it. Such a structure may be based on a wide-gap insulating crystal with a gaseous layer as the insulator. When the crystal−insulator interface in this structure is irradiated, an electrical charge is formed, which reduces the electric field in the crystal and consequently increases the field in the insulating layer.[4] When the field in the insulating layer (the gas) reaches a critical value the gas switches to the high-conductivity state (a gas discharge). Then the charge accumulated in the crystal flows out of it, producing a current pulse in the electronic circuit of the structure, after which the field in the gas layer is reduced below the critical value, the discharge stops, and the field distribution in the structure returns to its initial state; then the process starts all over again. In this way, steady irradiation of this structure will generate a cyclic redistribution of the applied voltage between the layers of the structure, accompanied by periodic current pulses generated in the circuit when the gas discharge occurs. The radiation energy incident per unit surface area of the structure over the time of one cycle of field redistribution in it is determined by the voltage applied to the structure, and does not depend on the intensity of the radiation. In this work we have studied the photoinduced redistribution of the applied voltage between the layers of such a structure based on the electrooptical insulating BSO crystals (bismuth silicate) with a gas layer as the insulator, and its photoelectric characteristics. A dc voltage $V_0 = 1-3$ kV is applied and the structure is illuminated with a steady extrinsic light ($\lambda = 0.63$ μm) on its surface parallel to the direction of the electric field, the light being partially transmitted through the structure. The redistribution of the applied voltage between the layers of the structure caused by the part of the light that is absorbed in the crystal was examined by an optical polarization method by measuring the time dependence of the intensity of the part of the light not absorbed in the crystal,[4] while at the same time measuring the time dependence of the current in the structure.

Figure 1 shows the experimental results for the time dependence of the longitudinal electrooptical effect in structures with two different kinds of insulators (mica and air)[4]
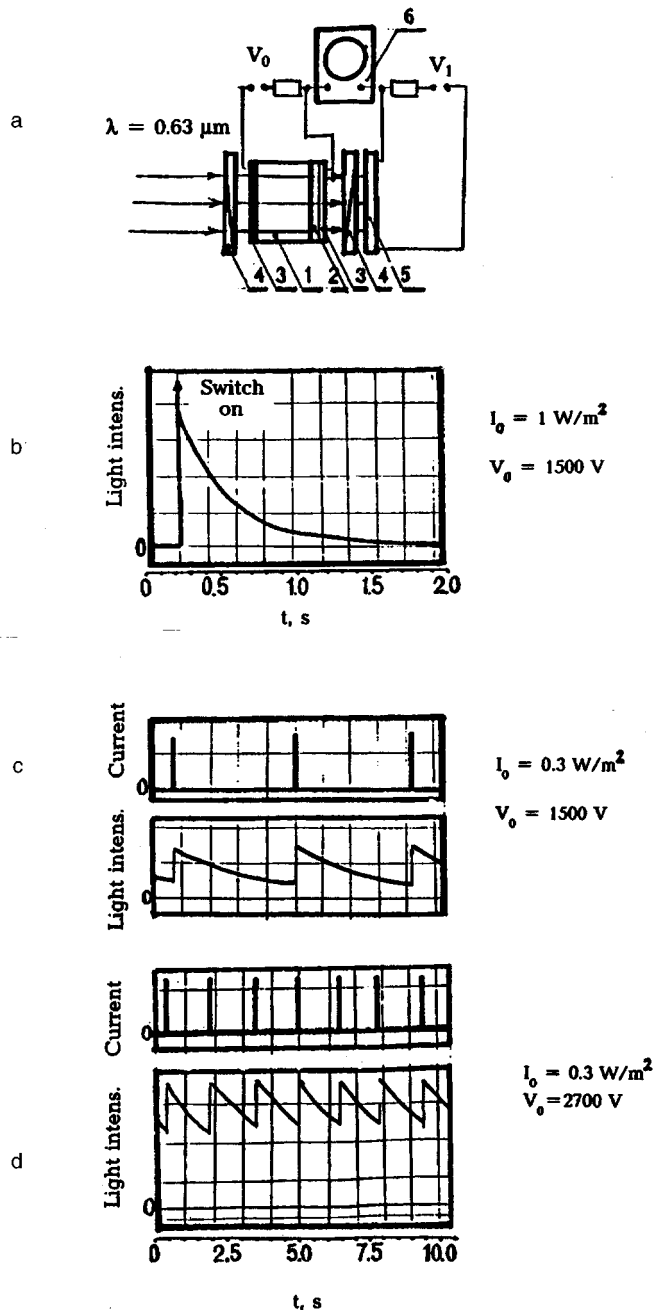
FIG. 1. Detection of the redistribution of the applied voltage V_0 between the layers of the metal–insulator–semiconductor structure under steady illumination: a — essential diagram of the device: 1 — electrooptical insulating crystal (BSO), 2 — insulating layer, 3 — optically transparent electrode, 4 — polarizer, 5 — photodetector, 6 — oscilloscope; b — time variation of the intensity of the light flux at the exit from the modulator when the metal–insulator–semiconductor structure with a mica insulator is illuminated with a light flux of constant intensity ($I_0 = 1$ W/m^2, $\lambda = 0.63$ μm, $V_0 = 1500$ V); c — the same, but with illumination of a similar structure with a gas insulator ($I_0 = 0.3$ W/m^2, $\lambda = 0.63$ μm, $V_0 = 1500$ V); d — the same for $V_0 = 2700$ V.

and the current in them during illumination. Both types of structures show the same exponential decrease of the intensity of the light flux with time during illumination, associated with the expulsion of the electric field from the crystal into the insulating layer. In the structures with the solid insulator
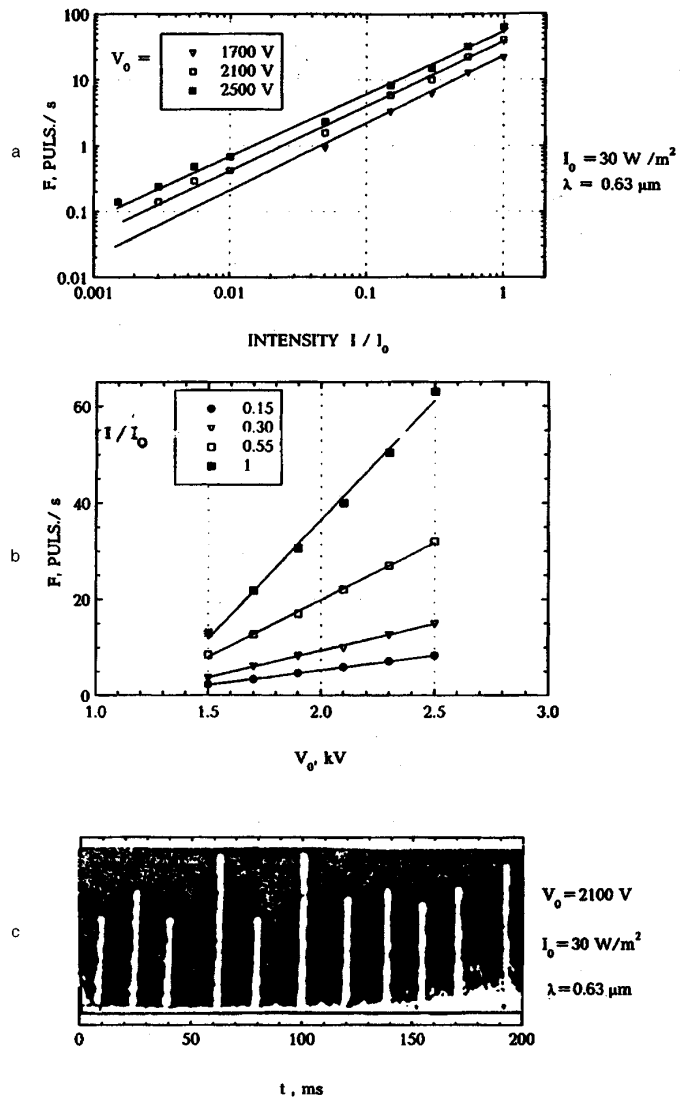

FIG. 2. Conversion of the intensity (I_0) of steady irradiation into a frequency F of current pulses in a metal–insulator–semiconductor structure with a gas insulator, on a BSO crystal: a — for fixed voltage on the structure ($V_0 = $ const, I_0 variable); b — for fixed irradiation intensity ($I_0 = $ const, V_0 variable); c — shape of current pulses in the analogous structure with steady irradiation ($I_0 = 30$ W/m^2 $V_0 = 2100$ V, $\lambda = 0.63$ μm).

(mica) this process continues until all the electric field is expelled from the crystal[4] (Fig. 1b). In the structure with the gas insulator the initial decrease in the intensity of the transmitted light flux is interrupted by a discontinuous recovery to the initial value (Fig. 1c, d), and a short current pulse flows (Fig. 1c,d (2) Fig. 2c). This process repeats periodically. This effect is explained by the switching of the gas layer into the high-conductivity state after the electric field in it exceeds some critical value. In Fig. 2a,b we show the frequency F of the current pulses in the circuit of such a structure based on the BSO crystal as a function of the intensity of the irradiation I and the applied voltage V for steady irradiation ($\lambda = 0.63$ nm). Figure 1a shows that $F(I)$ is linear over three orders of magnitude of intensity and $F(V)$ is linear for a variation of V over a factor of 2–3 (Fig. 2b). These devices can be operated as dosimeters for gamma rays, ultraviolet light and visible light, as well as for image recognition.

[1] A. A. Vasil'ev, D. Kasasent, I. N. Kampanents, and A. V. Parfenov, *Spatial Light Modulators* [in Russian] (Radio i Svyaz', Moscow, 1987).

[2] M. P. Petrov, S. I. Stepanov, and A. V. Khomenko, *Photosensitive Electrooptical Media in Holography and Optical Information Processing* [in Russian] (Nauka, Leningrad, 1982).

[3] I. S. Zakharov, *Space-Time Light Modulators* [in Russian] (Tomsk University, Tomsk, 1983).

[4] I. A. Zelenin, P. G. Kasherininov, and V. E. Khartsiev, Pis'ma Zh. Tekh. Fiz. **22**(5), 86 (1996) [Tech. Phys. Lett. **22**, 221 (1996)].

Translated by J. R. Anderson

Te$_{Cd}$ antistructural defects in CdTe crystals

O. A. Matveev and A. I. Terent'ev

A. F. Ioffe Physicotechnical Institute, Russian Academy of Sciences, St. Petersburg
(Submitted November 27, 1996)

Two-temperature annealing with a controlled vapor pressure of tellurium P_{Te2} is used to study CdTe$\langle$Cl$\rangle$ crystals under conditions of high-temperature thermodynamic equilibrium of the crystal with the gas phase (735–940 °C). For low pressures P_{Te2} ($\geqslant P_{min}$) Cl$_{Te+}$ begins to condense because of the formation of V$_{Cd-2}$ in the crystal. As P_{Te2} increases, this mechanism of exact self-compensation no longer operates because of the formation of Te$_{Cd+}$ intrinsic antistructural point defects. © *1997 American Institute of Physics.*
[S1063-7850(97)02302-1]

In this paper we present the result of a study of the phase equilibrium of CdTe:Cl and Te$_2$ gas, i.e., when the vapor pressure P_{Te2} of tellurium is controlled. This is an area of interest since here (with decreasing P_{Cd}) one might expect an increase in the concentration N$_{VCd}$. The charged V$_{Cd}^{-2}$ form associates with donor point defects.[1] At high values of N$_{VCd}$ (and for low t_{cr} and high binding energy in the associates) the association is almost complete.[2]

Thus the number of charged point defects should decrease because they join together in the crystal. In addition, the donor plus acceptor associate can be neutral, and therefore one should expect an increase in μ and τ of the electrons and holes with increasing N$_{VCd}$.

The annealing was carried out at three temperatures: $t_{cr}=735$ °C, $t_{cr}=870$ °C, and $t_{cr}=940$ °C. The annealing temperatures for which the self-compensation was studied in CdTe:Cl with controlled P_{Te2} were limited from above by the observable deformation of the sample due to sublimation of CdTe. At the lowest pressures $P_{Te2}\sim P_{Te2min}$ this is $t_{cr}\leqslant 940$ °C. The lowest annealing temperature $t_{cr}\sim 735$ °C was selected from considerations of the duration of the diffusion processes, which establish the composition in the crystal corresponding to the given P_{Te2}.

The intrinsic point defects in CdTe are electrically charged centers and they determine the free carrier concentration in the crystal. The free carrier concentration determined from Hall effect measurements on the annealed crystals and their dependence on P_{Te2} are shown in Fig. 1. For low values of P_{Te2} the sample sublimates, which is reflected in Fig. 1 by the dashed parts of the curves. It can be seen from this figure that both n-type and p-type samples were obtained after annealing. For all annealing temperatures t_{cr} three distinct sections of the curves can be distinguished; the first corresponds to a low and approximately constant concentration $n(p)\sim 10^7$–10^9 cm^{-3} for low P_{Te2}; the second section is for a high $n(p)\sim 10^{15}$ cm^{-3} and high values of P_{Te2}, and the third is the transition region between the first two. The first section corresponds to the exact self-compensated state of donor and acceptor defects of the crystal lattice (Cl$_{Te}^+$ and V$_{Cd}^{-2}$). The energy level of V$_{Cd}^{-2}$ in the band gap is $+0.83$ eV above E_v (Ref. 3). The second section corresponds to donor-controlled electrical conduction.[1]

Let us examine the results given in Fig. 1 in the region of low pressures $P_{Te2}\sim P_{Te2min}$. The samples annealed at $t_{cr}=735$ °C showed only n-type conduction (Fig. 1a). At this temperature the solubility of V$_{Cd}$ is small compared to the Cl concentration in the crystal. In the self-compensation process[4] a charged center V$_{Cd}^{-2}$ is formed that is responsible for the deep electron energy level in the band gap, and thus the low value of n. The value of n was lower than that measured for the crystals annealed at higher t_{cr}. With increasing t_{cr} following the line P_{min} (Fig. 2), we obtain a high concentration of acceptor intrinsic point defects (V$_{Cd}$) in the crystal (Fig. 1b, c). The samples annealed at $t_{cr}=870$ °C and $P_{Te2}\sim P_{Te2min}$ showed both p-type and n-type conduction (Fig. 1 b). The samples annealed at $t_{cr}=940$ °C were nonuniform in the conduction type. Both p-type and n-type conduction would exist within the same crystal. As the temperature was increased the regions of self-compensation were washed out, presumably because of the increasing concentration of point defects.[1]

When the crystal was annealed with increasing P_{Te2}, the concentrations $n(p)$ increased abruptly (Fig. 1). An increase in P_{Te2} (in the transition and second parts of the curves in Fig. 1) should result in an increase in V$_{Cd}$ (or Te$_i$) acceptor centers, i. e., an increase in p but not in n. However, this does not happen for $t_{cr}=735$ °C over the entire range of pressure P_{Te2}. For the case $t_{cr}=870$ °C we obtained both p-type and n-type samples only in the range of pressures P_{Te2} close to or slightly higher than P_{min}. For $t_{cr}=940$ °C we observed both p-type and n-type conduction over the entire range of pressures P_{Te2}.

These results can be explained by taking into account the participation of antistructural defects, Te$_{Cd}^{+2}$ donors, in the thermodynamic equilibrium. The formation of antistructural defects can be regarded as a transition of Te atoms from lattice sites or interstitial Te$_i$ to the V$_{Cd}$ sites, whose concentration increases with P_{Te2}. The calculated enthalpy of formation, $\Delta H(\text{Te}_{Cd}^{+2})=4.0$ eV (Ref. 5) and 5.56 eV (Ref. 6) is high compared to $\Delta H(\text{V}_{Cd}, \text{V}_{Te})=2.5$ eV (Ref. 5). (Other data[7] give $\Delta H(\text{Te}_{Cd}^{+2})=3.67$ eV and $\Delta H(\text{V}_{Cd}^{-2})=4.75$ eV). Consequently, the solubility of antistructural defects in the crystal can be appreciable only for high values of P_{Te2}. Because of the strong dependence of the concentration of Te$_{Cd}^{+2}$ on P_{Te2} (Ref. 6), the concentration of intrinsic point defects near P_{min} does not change relative to the models that do not take into account the effect of antistructural defects.[8,9]

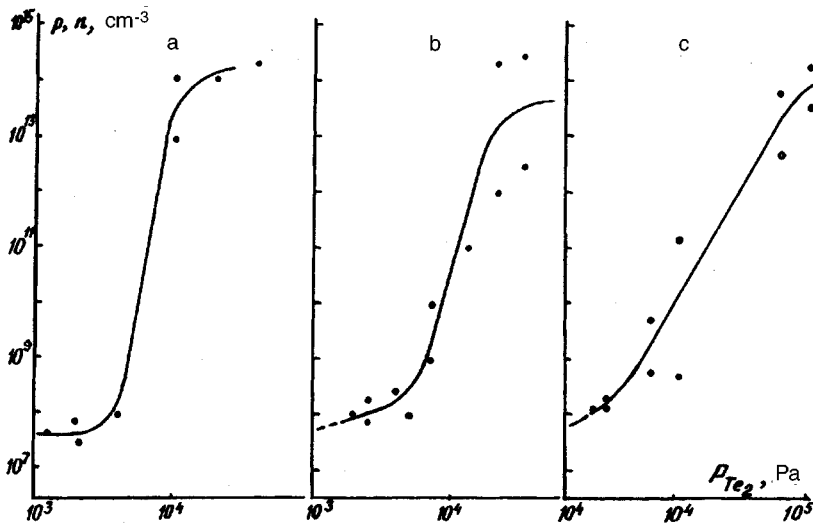The calculations in Ref. 5 show that compensation can

FIG. 1. Concentration of free carriers in the crystal versus P_{Te2}: a — $t_{cr}=735$ °C, b — 870 °C, c — 940 °C; 1 — n, 2 — p.

occur not only at high temperatures of the equilibrium thermodynamic state, but also when the crystal is cooled, because local energy gain when the diffusional loss of intrinsic point defects does not occur. It is well known that at high temperatures the concentration of intrinsic point defects, Te_i, is quite high, $\geqslant 10^{16}$ cm^{-3} (Refs. 6 and 8). Residing in tetrahedral sites, Te_i have a high outward relaxation, and will readily be drawn into regions where the superstresses of the crystal lattice (formed during cooling) will be removed, i.e., in the region of high concentration of V_{Cd} that have an inward relaxation displacement of neighboring atoms and can attract the Te_i (Ref. 10). This will also facilitate the creation of the antistructural defect Te_{Cd}, where the concentration of centers can be high ($\geqslant N_{Te_i}$) and the distribution over the crystal can be highly nonuniform, creating $n(p)$ regions with compensated conduction.

In these experiments on annealed crystals in a pressure P_{Te2} the maximum values of n at room temperature were $\sim 10^{15}$ cm^{-3}. According to the calculation, Te_{Cd}^{+2} is a deep donor center with ionization activation energies of $0.4E_g$ and $0.7E_g$ (Ref. 7). Doping with a donor to $N(Cl_{Te}^+)=10^{17}$ cm^{-3} and the same concentration of compensating intrinsic point defects V_{Cd}^{-2} does not allow us to assess the amount of

Te_{Cd}^+ in the crystal. However, inversion of the conduction type $p_i(n_i)$ to n-type indicates that $N(Te_{Cd})\sim N(V_{Cd})\sim N(Cl_{Te})$.

In summary, the method of annealing a CeTe:Cl crystal in Te_2 vapor yields crystals with a limited self-compensation of the electrical conduction. The dependence of p and n on P_{Te2} at annealing temperatures of 735–940 °C has been obtained. At low pressures P_{Te2} charge self-compensation occurs according to a model where V_{Cd}^{-2} and donor Cl_{Te}^+ are the principal centers responsible for the condition of electrical neutrality in the crystal. In this case complete association of charged point defects into neutral centers occurs. Here the results of annealing are compared with annealing with a controlled pressure P_{Cd} (Ref. 3). At high pressures P_{Te2} the complex intrinsic point defect Te_{Cd}^{+2} is formed. This defect prevents the creation of a high concentration of V_{Cd}^{-2}, which absorb the latter.

Higher annealing temperatures result in a higher solubility of V_{Cd}^{-2} and give a self-compensated p-type conduction of the crystal. However, these experiments are nonreproducible, and the crystal is not uniform in the concentration $p(n)$ because of the formation of antistructural defects when the material is cooled after annealing.
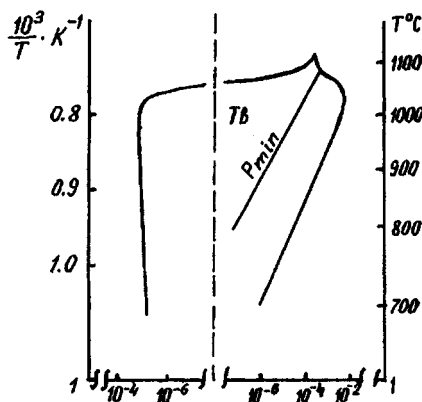

FIG. 2. $T–x$ cross section of the region of existence of solid CdTe.

[1] F. A. Kröger, *The Chemistry of Imperfect Crystals* (Wiley, New York 1964) [Russ. transl., Mir, Moscow, 1969].
[2] R. O. Bell, F. V. Wald, C. Canaly, F. Nava, and G. Ottavian, IEEE Trans. Nucl. Sci. **NS-21**, 331 (1974).
[3] O. A. Matveev and A. I. Terent'ev, Fiz. Tekh. Poluprovodn. **27**, 1894 (1993) [Semiconductors **27**, 1043 (1993)].
[4] G. Mandel, Phys. Rev. A **134**, 1073 (1964).
[5] J. A. Van Vechten, J. Electrochem. Soc. **122**, 423 (1975).
[6] V. N. Martynov and S. P. Kobeleva, Kristallographiya **28**, 394 (1983) [Sov. Phys. Crystallogr. **28**, 232 (1983)].
[7] M. A. Berding, M. van Schiltgaarde, M. Paxton, and A. Sher, J. Vac. Soc. Technol. A **8**, 1103 (1990).
[8] V. M. Glazov and L. P. Pavlova, Neorg. Mater. **30**, 629 (1994).
[9] C. G. Morgan-Pond and R. Raghaven, Phys. Rev. B **31**, 6616 (1985).
[10] J. T. Schick and C. G. Morgan-Pond, J. Vac. Sci. Technol. A **8**, 1108 (1990).

Translated by J. R. Anderson

Visualization of the reconstruction of a silver film on silicon

I. I. Pronin, N. S. Faradzhev, and M. V. Gomoyunova

A. F. Ioffe Physicotechnical Institute, Russian Academy of Sciences, St. Petersburg

In this investigation the focusing of medium-energy electrons is used to visualize the thermally activated reconstruction of a thin film of silver (6 monolayers) deposited on a Si(111)-7×7 surface at room temperature. It is shown that the initial unannealed film consists of Ag(111) domains of two types, mutually misoriented in azimuth by 180°. When the sample is heated to 350–400 °C, the film recrystallizes and a single-domain epitaxial layer of Ag(111) is formed. © *1997 American Institute of Physics.* [S1063-7850(97)02402-6]

The growth of a silver film on the surface of single-crystal silicon and the formation of its atomic structure is a topic still attracting a good deal of attention after many years.[1-3] Moreover, this system, whose components do not mix in the contact region, remains a model system for studying the formation of metal/semiconductor phase boundaries. However, not all the aspects of this process have yet been subjected to a thorough study. For example, no studies have been made of the evolution of the crystal structure of a rather thick continuous film condensed on Si(111)-7×7 at room temperature when it transforms into an island film. The purpose of the work reported here was directed at this problem.

To solve this problem we made use of a new method we have worked out for surface structure analysis. It is based on the focusing of quasi-elastically-scattered medium-energy electrons and permits visualization of the crystal structure of several surface monolayers of the object studied.[4,5]

The measurements were carried out in an angle-resolving secondary-electron spectrometer.[6] The energy resolution of the analyzer was 0.4%, and the angular resolution was 1°. The diffraction patterns of the quasi-elastically scattered electrons (the Kikuchi patterns) were obtained at an energy of 2 keV with automatic recording of the azimuthal distribution $I(\varphi)$ of the reflected electrons over nearly the entire reflection hemisphere of the electrons. The surface of the single-crystal silicon was cleaned by brief heating in ultrahigh vacuum at 1200 °C. The elemental composition of the surface was monitored by Auger electron spectroscopy, which was also used to determine the thickness of the deposited silver film. To study the thermally activated processes we used a three-minute annealing of the sample at higher temperatures. The Kikuchi patterns were recorded at temperatures intermediate between the latter and room temperature in a vacuum of 5×10^{-10} Torr.

In Fig. 1a we show the diffraction pattern obtained directly after an 18-Å silver film was deposited on the substrate at room temperature. The center circle on the pattern is at the normal to the sample surface and the outer circle corresponds to the electrons emitted along the tangent to the surface. The intensities of the various spots on the pattern are indicated on a linear gray scale (shown on the right) where the maximum reflected intensity corresponds to white and the minimum to black. It can be seen that the pattern is highly structured. Elements of sixfold symmetry are dominant. This is seen, for

example, for the strongest maximum at $\Theta = 35°$, which is repeated every 60° in azimuth. The overall shape of this pattern remains the same up to annealing temperatures of about 300 °C.

Qualitative changes in the diffraction pattern are observed upon heating the sample to $T = 350–400$ °C. This can be readily seen in Fig. 1b, which shows the corresponding Kikuchi pattern. Unlike the previous pattern, this one has pronounced threefold symmetry. It should be noted that the main intensity maxima of this pattern are due to focusing of the electrons along individual chains of atoms in the crystal and show the orientation of the latter in real space. Consequently the diffraction patterns can be considered as analogs of stereographic projections. It would therefore be interesting to compare the pattern in Fig. 1b with the stereographic projection of the Ag(111) surface, which also has threefold symmetry (Fig. 1d). It is seen that the main maxima of the pattern in Fig. 1b coincide with the orientation of the densest packed crystallographic directions, shown in Fig. 1d. We can thus conclude that after the sample is annealed at $T = 350–400$ °C, an epitaxial layer of the Ag(111) fcc structure is formed on the Si (111) surface.

These results may also serve as a starting point for interpreting the pattern of Fig. 1a. An analysis of its main features suggests that it is a superposition of two patterns, one of which coincides with the pattern of Fig. 1b we have just been discussing, while the other is similar to it but rotated in azimuth by 180°. We should point out that this is equivalent to the statement that two types of domains coexist on the silicon surface, differing by the stacking sequence of the silver atoms (ABCAB . . . and ACBAC . . .). To check this hypothesis we carried out a numerical simulation of the pattern in Fig. 1a with the assumption that the intensity of the quasi-elastic electron scattering, $I(\theta, \varphi)$, at each of its points specified by the angles θ and φ is given by

$$I(\theta, \varphi) = \alpha I_1(\theta, \varphi) + (1 - \alpha) I_2(\theta, \varphi),$$

where $I_1(\theta, \varphi)$ is the intensity of the pattern generated by the domains of the first type (Fig. 1b); $I_2(\theta, \varphi)$ is the intensity from the domains of the second type, and α is a variable parameter representing the statistical weight of the domains of the first type. The fraction of surface covered by domains of the first type (the optimum value of α) was determined by minimizing the reliability factor (the R_2 factor), which is
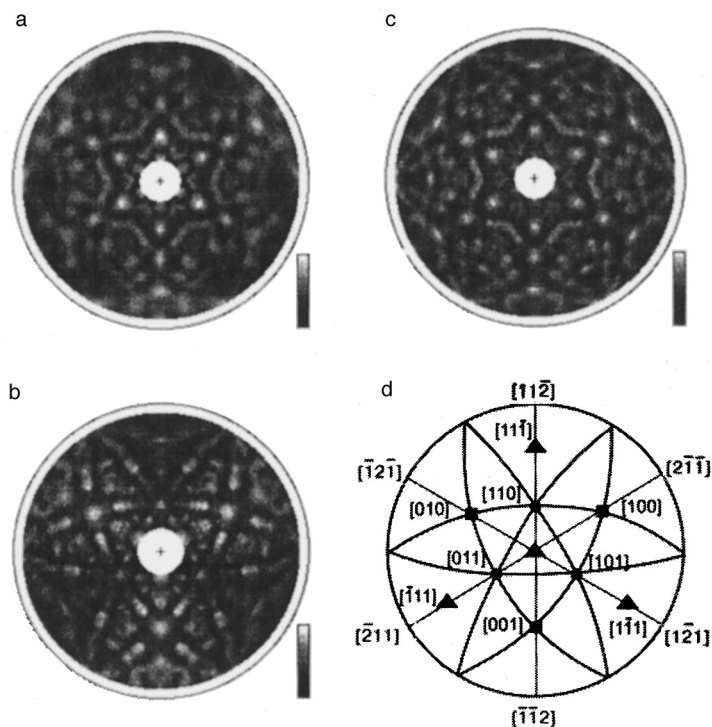
FIG. 1. a — Kikuchi pattern of a silver film 18 Å thick deposited on Si(111)-7×7 at room temperature; the data are shown as the two-dimensional intensity distribution $I(\theta,\varphi)$ of quasi-elastically-scattered 2 keV electrons over the polar and azimuthal emission angles and are shown as a stereographic projection; b — the analogous Kikuchi pattern for an annealed silver film; c — results of simulation of pattern a; d — stereographic projection of the Ag(111) face; the lines indicate the close-packed {100} and {110} planes of the crystal.

widely used to estimate the discrepancy between theoretically and experiment. This fraction of the surface was found to be $(52\pm2)\%$ and the R_2 factor 0.006.

The result of simulating the distribution of the Kikuchi pattern is shown in Fig. 1c. One can see very good agreement between the calculation and experiment. It follows that the film formed at room temperature consists of Ag(111) domains of two types, rotated from each other in azimuth by 180°. The coexistence of these domains in a film deposited at room temperature has also been observed elsewhere, but with the use of more sophisticated methods — ion scattering[7] and photoelectron spectroscopy with high energy and angular resolution.[8] However, the thermally activated reconstruction of the film with the formation of a single-domain Ag(111) structure is observed here for the first time. Previously it has only been noted that in the temperature interval used in the present experiments (where there is still very little thermal desorption of Ag) a change in the morphology occurs in the films, involving the formation of an island structure.[2] However, our data shows unambiguously that this process is accompanied by recrystallization of the film.

These results also show that the method we have developed might be used for visualization of various structural reconstructions in the surface layers of solids.

[1] V. G. Lifshits, A. A. Saranin, and A. V. Zotov, *Surface Phases on Silicon. Preparation, Structure, and Properties* (John Wiley and Sons, Chichester, 1994).

[2] S. Yasegawa, H. Daimon, and S. Ino, Surf. Sci. **186**, 138 (1987).

[3] G. Le Lay, Surf. Sci. **132**, 169 (1983).

[4] M. V. Gomoyunova, I. I. Pronin, N. S. Faradzhev *et al.*, Fiz. Tverd. Tela (St. Petersburg) **36**, 2295 (1994) [Phys. Solid State **36** 1250 (1994)].

[5] M. V. Gomoyunova, I. I. Pronin, N. S. Faradzhev, Zh. Éksp. Teor. Fiz. **110**, 311 (1996) [JETP **83**, 168 (1996)].

[6] I. I. Pronin, M. V. Gomoyunova, D. P. Bernatskiĭ *et al.*, Prib. Tekh. Éksp. No. 175 (1982).

[7] K. Sunimoto, K. Tanaka, Y. Ezawa *et al.*, Appl. Surf. Sci. **41−42**, 112 (1989).

[8] M. DeSeta, J. Avila, N. Franco *et al.*, in *European Conference Abstracts, 16th European Conference on Surface Science, Genova (Italy), September 9–13, 1996.*

Translated by J. R. Anderson

Basins of attraction for chaotic attractors in coupled systems with period doubling

B. P. Bezruchko and E. P. Seleznev

Institute of Radio Engineering and Electronics, Russian Academy of Sciences (Satatov Branch)

This article studies basins of attraction for chaotic attractors and their evolution when the attractors are restructured through variations in the control parameters. Numerical calculations show the evolution of the boundaries of the attractors, the changes within simply-connected regions, etc. Some of the regularities could be identified in a physical experiment.
© *1997 American Institute of Physics.* [S1063-7850(97)02502-0]

1. The coexistence of two or more attractors in phase space, with their own basins of attraction (multistability) is typical of nonlinear dynamical systems. When the control parameters are changed, the attractors evolve, undergoing various bifurcations. This is accompanied by a restructuring of their basins of attraction, so that the structure of the basins becomes very complicated and even fractal. These phenomena are studied experimentally and numerically in this investigation for chaotic oscillations of two symmetrically coupled systems, each of which, when the control parameter is varied, exhibits a transition to chaos through a sequence of period-doubling bifurcations.[1–3]

Two resistively coupled RL-diode circuits,[4,5] excited in phase by a harmonic external force, were studied experimentally. The dynamics of each of them in a limited region of parameters was qualitatively modeled by a quadratic mapping. As shown in Ref. 3, an adequate model of this experimental system is represented by two quadratic maps coupled dissipatively:[2]

$$\begin{cases} X_{n+1} = \lambda - X_n^2 + k(X_n^2 - Y_n^2), \\ Y_{n+1} = \lambda - Y_n^2 + k(Y_n^2 - X_n^2), \end{cases} \quad (1)$$

where X_n and Y_n are dynamic variables, $n = 1, 2, 3, \ldots$ is
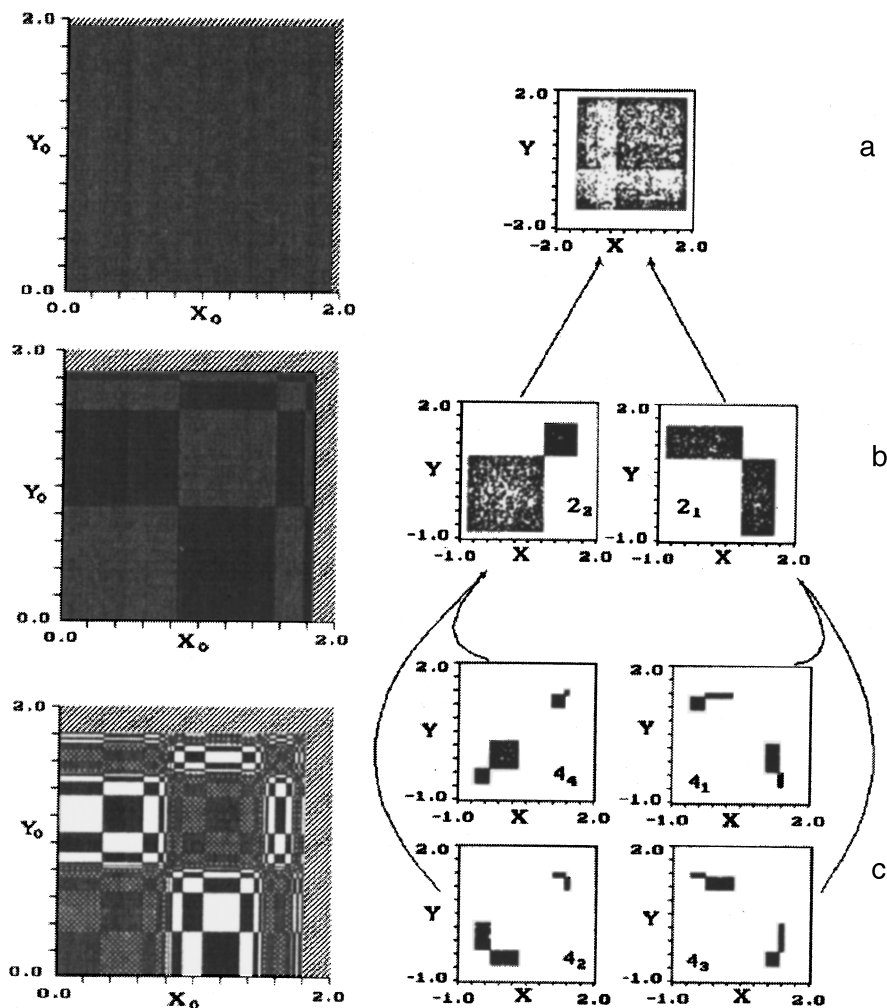

FIG. 1. Basins of attraction (left) of system (*1*) for the values: a — $\lambda = 1.8$, $k = 0$; b — $\lambda = 1.54$, $k = 0$; c—$\lambda = 1.428$, $k = 0$ (the phase portraits corresponding to the attractors are shown on the right hand side); d — $\lambda = 1.454$, $k = 0.0128$; e—$\lambda = 1.57$, $k = 0.42$, f—$\lambda = 1.7$, $k = 0.07$ (the right-hand side shows the fragments magnified.

FIG. 1. (continuation)

- $4_4, 2_2, 1_1$
- 4_2
- $4_1, 2_1$
- 4_3
- infinite solution
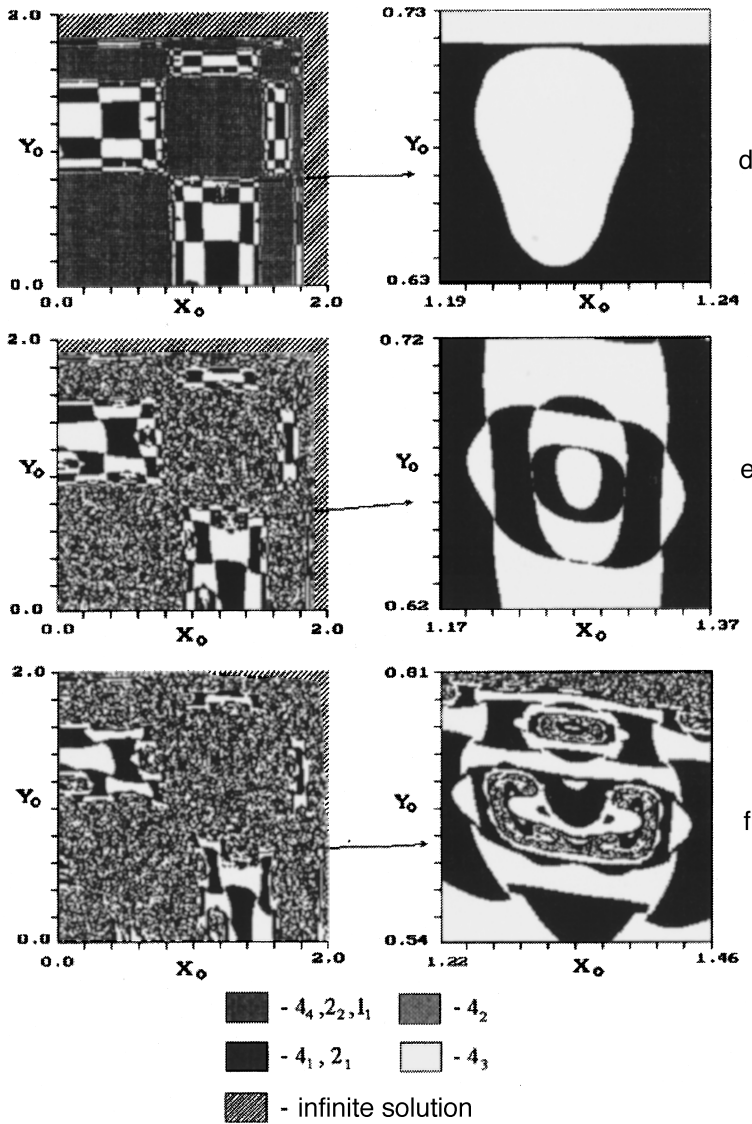
the discrete time, λ is the nonlinearity parameter, and k is the coupling constant. The analog to the coupling constant k in the experiment is the conductance of the coupling resistor, while the nonlinearity parameter λ is the amplitude of the harmonic driving force.

2. The variants of chaotic motion in these systems can nominally be divided into three kinds. Two of them, respectively, are in-phase (or synchronous, the oscillations of the subsystems are identical) and out of phase, which form as a result a cascade of period doublings. The existing attractors consist of bands (accumulations of phase trajectories). As the nonlinearity parameter is increased from the critical value at which the transition to chaos occurs, the number of bands in the attractor decreases from a theoretically infinite number to 1 by merging together. In Fig. 1a–c we show on the right examples 1, 2, and 4 of band attractors of the system (1). We introduce the notation N_m for identifying them, where N is the number of bands and m is the time displacement between X_n and Y_n. The in-phase oscillations correspond to $m=0$. The third class consists of chaotic oscillations that arise as result of disruption of the quasiperiodic motions.[1]

3. As the parameters are varied, a hierarchy of bifurcation transitions occur in the systems, reflected in Ref. 3 by evolution schemes. We shall vary the parameters and identify the main features in the structure of the basins of attraction of the chaotic attractors. We begin with an examination of the model (Eqs. (1)). The configuration of the region of existence of finite solutions in the plane of initial conditions (X_0, Y_0) varies smoothly with increasing coupling from a square with a side $l = (\sqrt{1+4\lambda}-1)/2$ for $k=0$ (Fig. 1a, left) to a circle for $k=0.5$. The entire region is a basin of attraction of a single chaotic attractor or is divided between multistable attracting manifolds as shown in Fig. 1.

The attractors and their basins have the same symmetry. For example, the attractors 4_2 and 4_4 and their basins are symmetric about the diagonal $X_0 = Y_0$ (interchange of X_n and Y_n). The attractors 4_1 and 4_3 and their basins are asymmetric, but with reflection of the (X_0, Y_0) plane about the diagonal $X_0 = Y_0$ they transform into one another. An infinite decrease in the dimensions of similar elements occurs near the boundaries of the basins of the attractors with different

145   Tech. Phys. Lett. **23** (2), February 1997

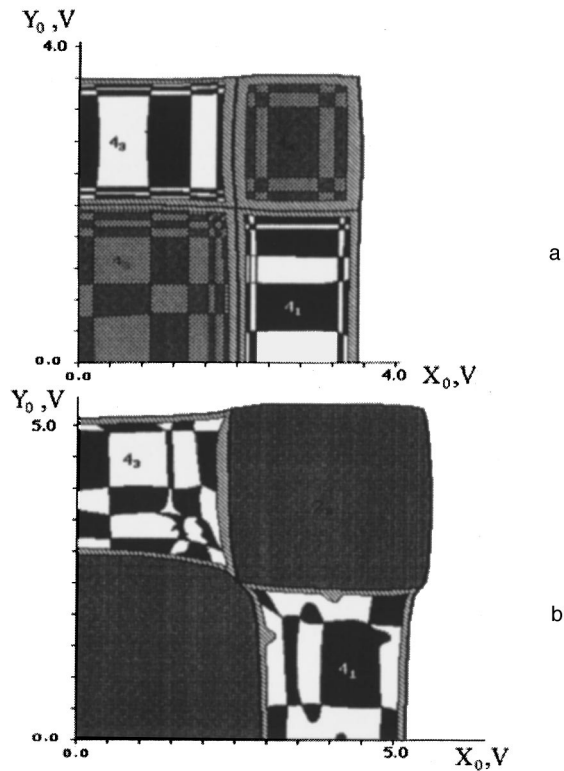B. P. Bezruchko and E. P. Seleznev   145

FIG. 2. Basins of attraction of chaotic attractors of the experimental system for the values: a — $\lambda = 1$ V, $k = 0.002$ ms, b — $\lambda = 1.79$ V, $k = 0.025$ ms.

However, more important metamorphoses occur for values of λ and k where phase space contains two 4-band attractors, while the 2_2 attractor coexisting with them becomes nonattracting and disappears. The region of the (X_0, Y_0) plane that its basin occupies is broken up in a fractal manner onto basins of attraction of the remaining pair of attractors (Fig. 1d). Symmetry about the diagonal $X_0 = Y_0$ appears in the seemingly unordered alternation of white and black regions in Fig. 1e. The structure of the embedded seas is preserved and occurs in even the smallest regions and remains finite. However, at certain critical values of λ and k this embedding of small areas into larger areas becomes infinite; i.e., the structure of the previously existing simply-connected regions becomes fractal (Fig. 1f).

Some of these regularities can be identified in a physical experiment. Figure 2 illustrates basins of attraction of attractors of oscillator circuits for situations analogous to Fig. 1e and 1f. The near-boundary region between the basins of the attractors, where small fragments not resolvable in a physical experiment accumulate, is shaded in Fig. 2 around the dark line (the separatrix). In, the experimental system we see in particular the merging of attractors with the attendant joining of the basins (4_2 and 4_4 into 2_2). Seas are observed within the simply-connected regions of the basins of attraction of the attractors 4_1 and 4_3 (Fig. 2b). The perceived asymmetry in the structure of the basins of attraction about the line $X_0 = Y_0$ exists because the partial experimental subsystems are not entirely identical.

4. The qualitative correspondence between the experimental and numerical results of these investigations demonstrates the generality of the regularities discussed here for period-doubling objects of this particular class and indicates the crudeness of the proposed picture. It should be emphasized that despite all the observed changes in the basins of attraction, the boundaries of each individual simply-connected region, both large and small, remain smooth.

symmetry — they become fractal. In a manner similar to periodic regimes[3,6] when a pair of chaotic merge together, their basins of attraction also merge. This is illustrated in Fig. 1 (c→b→a) for the case $k = 0$.

Let us now increase the coupling and simultaneously adjust the nonlinearity parameter so that during motion in the $\lambda - k$ plane one of the Lyapunov exponents remains approximately constant. The initial values of the parameters will be those corresponding to Fig. 1c. An increase in k causes a curvature (rounding) of the boundaries of the basins of attraction of the attractors in the manner described in Ref. 6 for periodic solutions. However, with further variations in λ and k, when the attractors 4_4 and 4_2 merge into the two-band attractor 2_2, the basins of chaos demonstrate specific properties. A ''sea'' of a basin of mirror-symmetric attractors (Fig. 1d) is formed within the previously simply-connected regions according to the scenario of Ref. 7. Variation of λ and k results in the formation of new seas of smaller size within these seas. The number of ''seas within seas'' increases with increasing parameter values but remains finite, a conclusion supported by the enlarged left fragment in Fig. 1e.

[1] K. Kaneko, *Collapse of Tori and Genesis of Chaos in Dissipative Systems* (World Scientific, Singapore, 1986.

[2] S. P. Kuznetsov, Izv. Vyssh. Uchebn. Zaved. Radiofiz. **28**, 991 (1985).

[3] V. V. Astakhov. B. P. Bezruchko, E. N. Erastova, and E. P. Seleznev, Zh. Tekh. Fiz **60**(10), 19 (1990) [Sov. Phys. Tech. Phys. **35**, 1122 (1990)].

[4] P. S. Linsay, Phys. Rev. Lett. **47**, 1349 (1981).

[5] R. Buskirk and C. Jeffries, Phys. Rev. A. **31**, 3332 (1985).

[6] B. P. Bezruchko, E. P. Seleznev, and E. V. Smirnov, Pis'ma Zh. Tekh. Fiz. **21**(8), 12 (1995) [Tech. Phys. Lett. **21**, 282 (1995)].

[7] C. Mira, D. Fournier–Prunaret, L. Gardini, H. Kawakami, and J. C. Cathala, Int. J. of Bif. Chaos. **4**, 343 (1995).

Translated by J. R. Anderson

Spectra of polycrystalline and single-crystal silicon for solar cells measured by deep-level transient spectroscopy

S. M. Kikkarin, B. N. Mukashev, M. F. Tamendarov, and S. Zh. Tokmoldin

Physicotechnical Institute, Ministry of Science, Academy of Sciences of Kazakhstan, Almata

Investigations are reported concerning the spectra of polycrystalline and single-crystal silicon for solar cells. A broad peak is observed in the distribution of traps in the silicon of commercial solar batteries. It is proposed that they are due to residual impurities. The peaks are suppressed by hydrogen passivation. © *1997 American Institute of Physics.* [S1063-7850(97)02602-5]

Polycrystalline silicon in the form of ribbons or ingots is a prospective material for fabricating solar cells. However, the efficiency of solar cells is frequently reduced by the presence in the silicon of deep recombination centers in the form of defects that have been introduced inadvertently during growth. To limit this factor it is necessary to identify the nature of these defects and work out methods of passivation and gettering.

The interaction of hydrogen with defects and impurities is well known and has been well studied (see, e.g., Refs. 1 and 2). Hydrogen also is able to passivate grain boundaries and dislocations in silicon.[3] The ability of hydrogen to passivate defects and impurities is of great significance for solar cell technology, since this technique makes it possible to obtain high efficiency in solar batteries prepared from relatively cheap polycrystalline silicon.

In this paper we present some preliminary results obtained by capacitive deep-level transient spectroscopy with samples of polycrystalline and single-crystal p-type silicon doped with boron ($N_B \sim 10^{16}$ cm^{-3}) intended for commercial solar cells.

For the spectrometer we designed and built a highly sensitive capacitance meter attached to a PC equipped with an analog-to-digital converter with a sampling frequency up to 200 kHz. Control of the spectrometer and the signal processing techniques were realized as a "virtual device" in the terms of the software LabVIEW^{TM} for Windows. With the spectrometer we could observes traps at a concentration $10^{-5}N_B$, where N_B is the concentration of the shallow doping impurities. The sensitivity of the spectrometer was limited mainly by the quality of the n^+–p junctions. For the measurements we used samples of n^+–p mesa structures from commercial solar cells.

The solar cell samples were passivated with hydrogen. The hydrogen was implanted from a Kaufmann-type ion source at a substrate temperature of 250 °C, with the ion energy in the range 1–2 keV and a maximum dose of about 5×10^{17} cm^{-2}.

A spectrum measured for the n^+–p sample of a polycrystalline solar cell is shown in Fig. 1. The broad peak with a jagged top around 200 K is associated with majority carrier traps, and also with recombination centers for minority carriers in the high-temperature region. The width of the peak indicates a broad distribution of discrete levels in the band gap. The peaks are completely gone after hydrogenation under the conditions described above, which indicates a reduction in the concentration of hole and electron traps to a level below the sensitivity of the spectrometer. The sensitivity threshold for these samples is 4×10^{11} cm^{-3}. The traps for majority carriers (holes) in p-type polycrystalline silicon are associated with grain boundaries (see, e.g., Refs. 4 and 5),
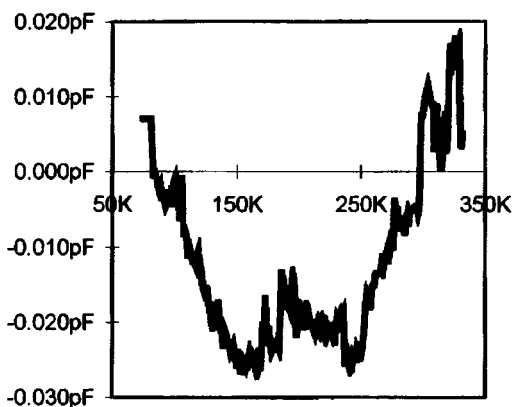

FIG. 1. Deep-level transient spectroscopy spectrum measured on an n^+–p sample of polycrystalline silicon. The horizontal axis is the temperature in K. The vertical axis is the measured capacitance in pF.
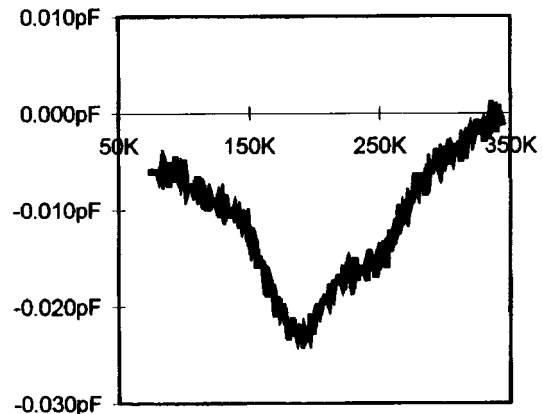

FIG. 2. Deep-level transient spectroscopy spectrum measured on an n^+–p sample of single-crystal silicon. The horizontal axis is the temperature in K. The vertical axis is the measured capacitance in pF.

while the electron traps are believed to be distributed over the entire bulk of the silicon.[6]

We also measured the spectrum of an n^+-p sample of single-crystal silicon solar cells. The spectrum is shown in Fig. 2. It has a broad peak centered around 180 K, which indicates a broad distribution of majority carrier traps. This peak also disappears completely, within the limits of sensitivity of the spectrometer, after hydrogen passivation.

To summarize, we have used a high-sensitivity spectrometer and capacitive deep-level transient spectroscopy to observe broad peaks in the distribution of traps in commercial polycrystalline and single-crystal silicon solar cells. The peaks are tentatively associated with residual contaminant impurities, boundaries and growth defects, and are sup-

pressed by hydrogen passivation. In polycrystalline silicon the peak is tentatively associated with grain boundaries. The peak also is well passivated with hydrogen. On the average, the relative increase in the efficiency of the solar cells after passivation is about 20%.

[1] S. J. Pearton, J. W. Corbett, and T. S. Shi, Appl. Phys. A. **43**, 153 (1987).
[2] B. N. Mukashev, S. Zh. Tokmoldin, and S. Zh. Tamendarov, Fiz. Tekh. Poluprovodn. **26**, 1124 (1992) [Sov. Phys. Semicond. **26**, 628 (1992)].
[3] J. C. Muller *et al.*, Solar Cells **17**, 201 (1986).
[4] P. S. Srivastava *et al.*, J. Appl. Phys. **53**, 8633 (1982).
[5] O. S. Sastry *et al.*, J. Appl. Phys. **57**, 5506 (1985).
[6] P. K. McLarty, D. E. Ioannou, and A. P. Shea, J. Appl. Phys. **61**, 2672 (1987).

Quantum-dot cw heterojunction injection laser operating at room temperature with an output power of 1 W

Yu. M. Shernyakov, A. Yu. Egorov, A. E. Zhukov, S. V. Zaĭtsev, A. R. Kovsh, I. L. Krestnikov, A. V. Lunev, N. N. Ledentsov, M. V. Maksimov, A. V. Sakharov, V. M. Ustinov, Chao Chen, P. S. Kop'ev, Zh. I. Alferov, and D. Bimberg

A. F. Ioffe Physicotechnical Institute, Russian Academy of Sciences, St. Petersburg
Technical University of Berlin

This paper describes a new cw laser with tunnel-coupled vertically aligned InGaAs quantum dots in an AlGaAs matrix with a room-temperature output power of $\sim$ 1 W at both mirrors. The maximum operating temperature of the heat sink is $\sim$ 75 °C. © *1997 American Institute of Physics.* [S1063-7850(97)02702-X]

Further progress in the development of heterojunction lasers is bound up with the use of quantum dots in the active region.[1] Recently self-organization effects on a surface[2] have been utilized to produce a large bank of elastically stressed nano-size InGaAs–GaAs quantum dots with a high density, highly ordered in shape and size,[3] and an injection laser was developed on the basis of this object.[4] Considerable improvements in the properties of these lasers have been attained by preparing quantum dots tunnel-coupled in the vertical direction[5] and embedding the quantum dots in an AlGaAs matrix.[6] In the latter case the threshold current density was 60 A/cm^2 at room temperature .

The structure was grown by molecular beam epitaxy on a substrate of n-GaAs(100) in the standard double-heterojunction separate-confinement geometry with a graded-index waveguide. The technological conditions for growing the device have been described in Ref. 5. The substrate temperature during growth of the emitter and the waveguide was 700 °C and during growth of the active layer, 485 °C. The active region of the laser was a stack of 10 layers of vertically coupled In$_{0.5}$Ga$_{0.5}$As quantum dots separated by interlayers of Al$_{0.15}$Ga$_{0.85}$As with a thickness of 50 Å. The effective thickness of the deposited InGaAs was 12 Å.

The lasers were laid out in a planar geometry with a stripe width of 114 μm (a structure of the "small mesa" type). No dielectric coating was applied to the mirrors.

The photoluminescence spectra of the tunnel-coupled quantum dots are described in Ref. 6. In the present article we report investigations of the power and spectral properties of the quantum-dot heterojunction laser. The threshold current density in the laser with a cavity length of 1100 μm at room temperature was 290 A/cm^2.

In Fig. 1a we show the current-power characteristics of the laser at room temperature, and in Fig. 1b the spectrum of the laser emission at the corresponding pump currents. The lasing peak shifts towards longer wavelengths with increased pump current, which indicates that the structure is heated by 20 °C at a power of $\sim$300 mW. As the pump current is increased the width of the spectrum also increases somewhat.

The maximum emitted power at the two mirrors was from 800 mW to 1 W at room temperature. The differential efficiency was about 40%.
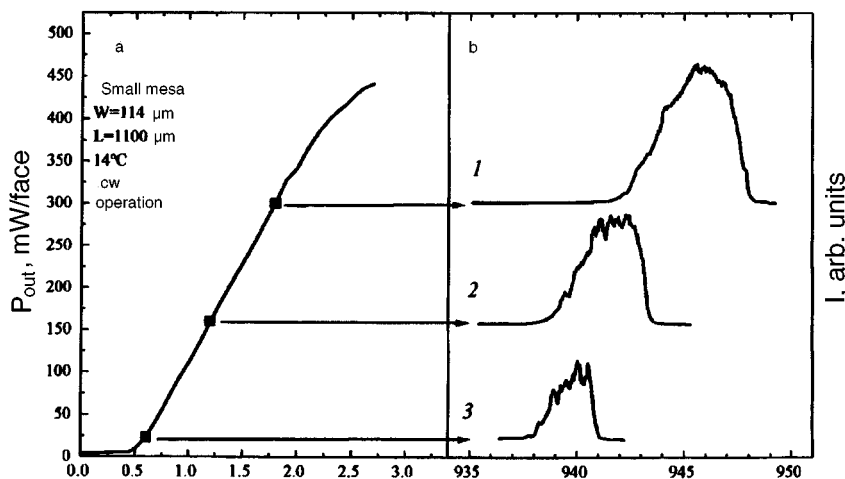
In Fig. 2 we present the current–power characteristics of

FIG. 1. a — Current–power characteristics of the laser in cw operation at 14 °C; b — laser emission spectrum for various pump currents: *1* — 0.6 A, *2* — 1.2 A, *3* — 1.8 A.
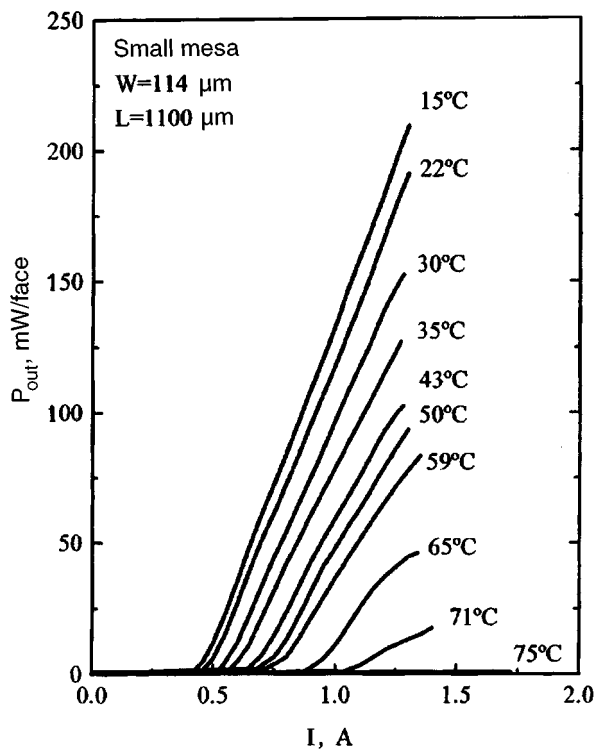
FIG. 2. Current–power characteristics of the laser in cw operation, taken for various heat sink temperatures.

the laser in cw operation above room temperature. This figure shows that the maximum temperature of the heat sink at which lasing can be obtained is ~70–75 °C.

In conclusion, our data indicate that the quantum-dot structures are suitable for making high-power injection lasers. Further optimization of the structure (increase in differential efficiency, reduction in the threshold current density in the stripe, the use of dielectric mirrors) should substantially improve the maximum output power.

[1] Y. Arakawa and H. Sakaki, Appl. Phys. Lett. **40**, 939 (1982).

[2] L. Goldstein, F. Glas, J. Y. Marzin, M. N. Charasse, and G. Roux, Appl. Phys. Lett. **47**, 1099 (1985). V. 47. P. 1099.

[3] N. M. Ledentsonv, M. Grindmann, N. Kirstaedter, O. Schmidt, R. Heitz, J. Böhrer, D. Bimberg, V. M. Ustinov, V. A. Shchukin, P. S. Kop'ev, Zh. I. Alferov, S. S. Ruvimov, A. O. Kosogov, P. Werner, U. Richter, V. Gösele, and J. Heydenreich, *7th International Conference on Modulated Semiconductor Structures*, Madrid, Spain, June 1995, published in *Solid State Electronics*, 1996. V. 40., P. 785.

[4] N. Kirstaedter, N. N. Ledentsov, M. Grundmann, D. Bimberg, U. Richter, S. S. Ruvimov, P. Werner, J. Heydenreich, V. M. Ustinov, M. V. Maximov, P. S. Kop'ev, and Zh. I. Alferov, Electronics Letters. **30**, 1416 (1994).

[5] Zh. I. Alferov, N. A. Bert, A. Yu. Egorov, A. E. Zhukov, P. S. Kop'ev, A. O. Kosogov, I. L. Krestnikov, N. N. Ledentsov, A. V. Lunev, M. V. Maksimov, A. V. Sakhharov, V. M. Ustinov, A. F. Tsatsul'nikov, Yu. M. Shernyakov, and D. Bimberg, Fiz. Tekh. Poluprovodn. **30**, 351 (1996) [Semiconductors **30**, 194 (1996)].

[6] N. N. Ledentsov, *23rd International Conference on the Physics of Semiconductors*, Berlin, July 1996.

Translated by J. R. Anderson

Infrared laser (λ=3.2 μm) based on broken-gap type II heterojunctions with improved temperature characteristics

K. D. Moiseev, M. P. Mikhaĭlova, O. G. Ershov, and Yu. P. Yakovlev

A. F. Ioffe Physicotechnical Institute, Russian Academy of Sciences, St. Petersburg

Laser structures based on broken-gap type II p-GaInAsSb/n-InGaAsSb heterojunctions in the active region are proposed and studied. Lasing at 3.2–3.4 μm has been obtained in the temperature range 77–195 K with a threshold current density of 400 A/cm² at 77 K and a characteristic temperature $T_0 = 47$ K.   © *1997 American Institute of Physics.* [S1063-7850(97)02802-4]

Previously we have reported the fabrication and study of a new tunnel-injection laser,[1] in which a broken-gap isotypic type II p-GaInAsSb/p-InAs heterojunction is located in the active region. The main feature of this laser is that lasing occurred by indirect radiative transitions of electrons and holes at the heterojunction, accompanied by tunneling. The operating current is maintained by tunneling injection of electrons from the bulk of the narrow-gap semiconductor. In this laser structure Auger recombination at the heterojunction is suppressed and the temperature dependence of the threshold current is less strong:[2] in the temperature range 80–110 K a high characteristic temperature, $T_0 = 40$–60 K, was observed. Single-mode lasing was obtained in the temperature range 77–125 K. At $T = 77$ K the wavelength of the stimulated emission was λ = 3.26 μm, and the threshold current density was 2 kA/cm². Further improvements in the threshold characteristics of this laser are limited for several fundamental reasons. The first is the large hole leakage current from the valence band of the wide-gap semiconductor into the valence band of the narrow-gap semiconductor through the narrow barrier at the heterojunction, which is related to the details of the energy band diagram of the p–p heterostructure with reverse bias.[2] Second, radiative recombination and lasing occur in the narrow-gap heterostructure in the narrow region near the heterojunction. Because of Auger processes,[3] which have no threshold, the minority carriers are localized near the interface, and this results in an increase in interband absorption, which depends exponentially on the temperature.

In this work we propose a new approach to making laser structures of type II heterojunctions by locating in the active region broken-gap p–n junctions, whose band diagram is shown in Fig. 1. It is proposed that this structure, unlike the p–p heterojunction, will greatly reduce the hole leakage through the heterojunction while maintaining a large band offset, which provides good electron confinement. It is also expected that these factors will decrease the threshold current and increase the operating temperature of the laser.

First we prepared a model p–n heterostructure and studied its luminescence properties. The undoped quaternary wide-gap layer of $Ga_{0.83}In_{0.17}As_{0.22}Sb_{0.78}$ with a hole concentration $p = 4 \times 10^{16}$ cm^{-3} was grown by liquid-phase epitaxy on a lightly doped n-InAs substrate ($n = 2 \times 10^{16}$ cm^{-3}). When a forward bias $U > 0.4$ V was applied to this structure

at $T = 77$ K, intense electroluminescence was observed (Fig. 1), consisting of two bands: a narrow one with a photon energy $h\nu_1 = 392$ meV at the peak and a long-wavelength one, less intense and broader, at $h\nu_2 = 333$ meV. The peak of the band $h\nu_1$ was close to the band gap of n-InAs, $E_g = 412$ meV, so it may be concluded that radiative transitions in the bulk of the n-InAs are responsible for this band. The second band can be assigned to electron recombination from the quantum well on the InAs side with Auger holes in the wide-gap layer. Unlike the case of the p–p heterostructure, the well at the p–n broken-gap heterojunction with light doping ($\sim 10^{16}$ cm^{-3}), should be quite broadened and the electron states in it should form a broad spectrum. These results were used by us in preparing the new laser structure with a broken-gap type II heterojunction in the active region.

We prepared a five-layer structure with separate electron and optical confinement, as shown in Fig. 2, grown by liquid-phase epitaxy on a p-InAs(100) substrate. The coating
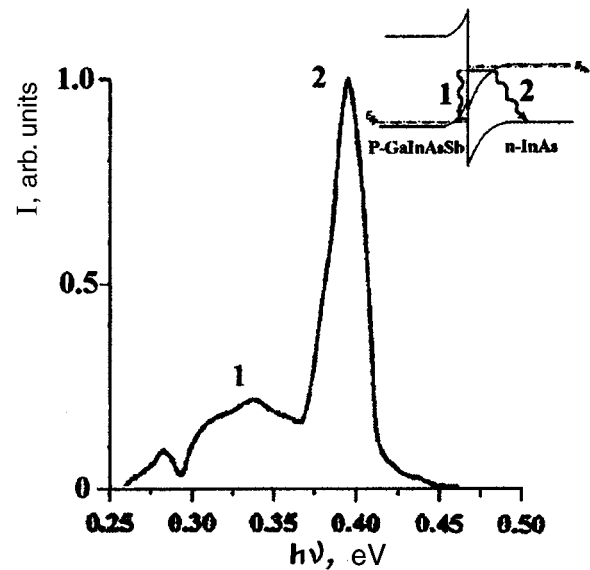
FIG. 1. Electroluminescence spectrum of p-GaInAsSb/n-InAs heterostructures with forward bias at $T = 77$ K. The emission bands correspond to radiative transitions involving the heteroboundaries (*1*) and the bulk $n =$ InAs (*2*). The inset shows the energy band diagram of the broken-gap type II p-GaIn$_{0.17}$As$_{0.22}$Sb/n-InAs heterojunction with a forward bias. The arrows show the possible recombination transitions.
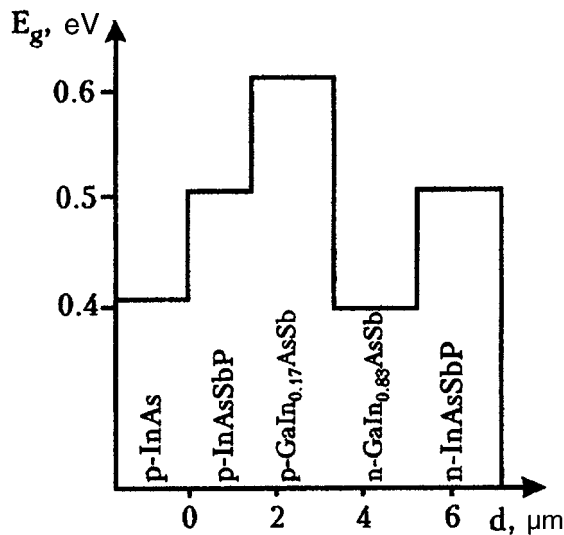
FIG. 2. Layer arrangement of the new laser structure with broken-gap type II $p-n$ heterojunction in the active region.
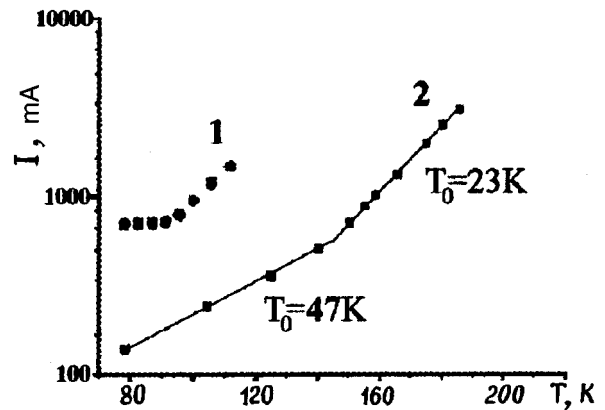

FIG. 3. Temperature dependence of the threshold current for two laser structures with broken-gap $p-p$ (*1*)and $p-n$ (*2*) type II heterojunctions in the active region.

layers were made of the quaternary solid solutions $InAs_{1-x-y}Sb_yP_x$ ($x=0.30$). The active region was formed of two $Ga_{1-x}In_xAs_ySb_{1-y}$ solid solutions, a wide gap layer ($E_g=640$ meV) and a narrow-gap layer ($E_g=390$ meV), with an indium content of 0.17 and 0.83, respectively. These solid solutions form together a type II heterojunction, close to broken-gap (the gap beween the valence band of the wide-gap semiconductor and the conduction band of the narrow-gap semiconductor is about $\Delta \sim 40-60$ meV, according to our estimates). In calculating Δ we used a linear interpolation of the electron affinity of the binary compounds forming the quaternary compounds GaInAsSb (Ref. 4). The large offset in the conduction band of the laser structure, $\Delta E_c \sim 600$ meV, provided good electron confinement.

In this structure we observed spontaneous and coherent emission, and single-mode lasing was obtained at the wavelength $\lambda=3.2$ μm with a threshold current density $j_{th}=400$ A/cm^2 at $T=77$ K. The threshold current was five times lower than that for a previously described laser structure with broken-gap type II $p-p$ heterostructures in the active region.[1] Figure 3 shows that in the new laser we have been able to extend the region of weak temperature dependence of the threshold current in pulsed operation ($\tau=200-500$ ns) to $T=140-150$ K, as compared with $T=110$ K obtained for the laser with the $p-p$ heterojunction.[1] We also obtained a high characteristic temperature $T_0=47$ K in the range 77–140 K and 30 K in the range 150 to 200 K. The highest operating temperature of the laser was extended to $T=195$ K. We also studied the polarization dependence of the radiation in the new laser structure in spontaneous and pulsed operation. It can be seen in Fig. 4 that TM polarization always predominates over TE polarization. This may be explained by the fact that the recombination involves light holes that tunnel through the heteroboundary.[5]

To improve the characteristics and raise the operating temperature of the InAs lasers to room temperature requires further optimization of the laser structure, including investigations of the fundamental loss mechanisms (Auger processes, heat loss in the confining layers of the structure, interband absorption and the related carrier heating, etc.).

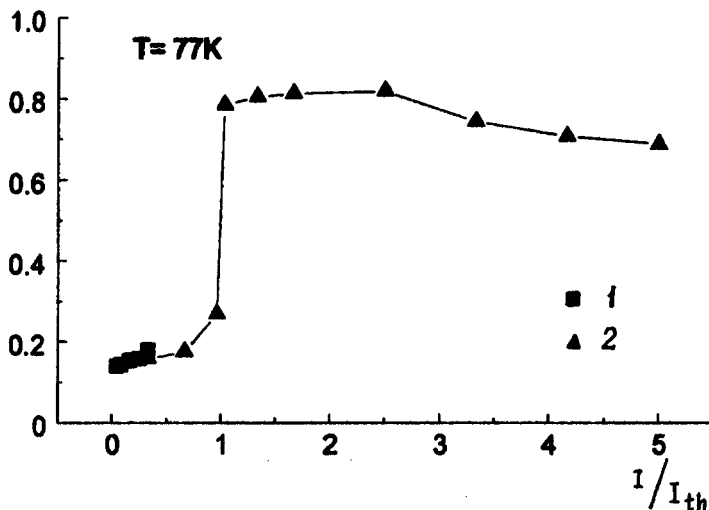In conclusion, we have proposed and fabricated a new

FIG. 4. Degree of polarization $P=(P_{TM}-P_{TE})/(P_{TM}+P_{TE})$ as a function of the ratio of the pump current to the threshold current, I/I_{th}; *1* — spontaneous luminescence, *2* — coherent radiation.

and improved laser structure based on a type II p-GaInAsSb/n-InGaAsSb broken-gap heterojunction in the active region, and have observed single-mode lasing at the wavelength $\lambda = 3.2$ μm with a threshold current density $j_{th} = 400$ A/cm^2 ($T = 77$ K). A high characteristic temperature $T_0 = 47$ K has been obtained, and the operating temperature of the laser in pulsed operation has been raised to $T = 195$ K.

The authors wish to thank S. Luryi, A. D. Gorbatyuk, and G. G. Zegrya for helpful discussions.

[1] K. D. Moiseev, M. P. Mikhaılova, O. G. Ershov, and Yu. P. Yakovlev, Pis'ma Zh. Tekh. Fiz. **21** 83 (1995) [*sic*].

[2] M. P. Mikhaĭlov, G. G. Zegrya, K. D. Moiseev, I. N. Timchenko, and Yu. P. Yakovlev, Fiz. Tekh. Poluprovodn. **29**, 687 (1995) [Semiconductors **29**, 357 (1995)].

[3] G. G. Zegrya and A. D. Andreev, Appl. Phys. Lett. **67**, 2683 (1996).

[4] H. Sai-Halasz, R. Tsu, and L. Esaki, Appl. Phys. Lett. **30**, 651 (1977).

[5] N. S. Averkiev, A. N. Baranov, A. N. Imenkov, A. A. Rogachev, and Yu. P. Yakovlev, Pis'ma Zh. Tekh. Fiz. **13**, 332 (1987) [Sov. Tech. Phys. Lett. **13**, 135 (1987)].

Growth dynamics of GaAs on a vicinal surface of GaAs(100) in migration-stimulated epitaxy: computer simulation

G. É. Tsyrlin

Institute of Analytic Instrument Construction, Russian Academy of Sciences, St. Petersburg

A computer simulation is made of growth of III–V binary compound semiconductors from fluxes of dimer anions and atomic cations to study the time dependences of the average height and roughness of GaAs films for various conditions of growth by migration-stimulated epitaxy on a vicinal surface of GaAs(100). © *1997 American Institute of Physics.*
[S1063-7850(97)02902-9]

The method of molecular beam epitaxy makes it possible to grow in a controlled way single-crystal semiconducting compounds with transition layers a few monolayers thick. This permits the fabrication of a new class of device, whose principle of operation is based on size-quantization effects. There are, however, a number of drawbacks associated with this technology. For example, in the growth of structures with semiconductors of different compositions, it must be taken into account that the region of the interface (e.g., GaAs/Al$_x$Ga$_{1-x}$As) has a high density of atomic steps; moreover, although the substrate temperature during growth is considerably lower than in other epitaxial methods (such as liquid-phase epitaxy or MOVPE), and these temperatures are low enough for interlayer diffusion of the doping impurities to be neglected. Thus with the use of conventional molecular beam epitaxy it is difficult to obtain very abrupt interfaces between semiconductors of different composition and doping profile, which is an important factor in the preparation of structures with quantum wells, quantum wires, and quantum dots. To avoid these drawbacks it is first necessary to stimulate surface kinetic processes and second to reduce the growth temperature. To this end one tactic that is used is to suspend the growth by closing the shutter on the source that governs the growth (in the III–V system it is the group III element),[1] to use sources with ionization of the elements,[2] etc. However, the method of migration-stimulated epitaxial,[3] which has been developed over the past few years, provides a method that goes the farthest in solving the problem of creating a very abrupt interface. One of the tools by which it is possible to observe the principal stages of growth is statistical simulation of the growth process by the Monte Carlo method.

This paper uses computer simulation of the growth of binary III–V compound semiconductors from fluxes of anion dimers and cation atoms to analyze the time dependence of the mean height and the roughness of GaAs films for various growth conditions in the method of migration-stimulated epitaxy on a GaAs(100) vicinal surface.

The computer model proposed in Ref. 6 was used to describe migration-stimulated epitaxial growth. The main propositions of the model are as follows. The arsenic molecule is assumed to be diatomic, and dissociative chemisorption occurs by a two-step mechanism.[7] The flux of gallium is assumed to be atomic; the criterion for the chemisorption of a Ga atom is that it occupy its own sublattice in a defect-free location, plus the presence of two empty bonds with neighboring As atoms in the previous atomic layer.

The energetics of the "atom plus surroundings" system is given by the Hamiltonian function:

$$H = -E_1 \int z(\mathbf{R})\,\delta(|\mathbf{R}| - a\sqrt{2}/4)\,d\mathbf{R}$$
$$+ E_2 \int z(\mathbf{R})\,\delta(|\mathbf{R}| - a\sqrt{2}/2)\,d\mathbf{R}, \tag{1}$$

where a is the lattice constant, E_1 is the binding energy of nearest neighbors, E_2 is the binding energy of next-nearest neighbors, and $z(\mathbf{R})$ is a function that is nonzero only at occupied lattice sites, where it equals unity. The zero of energy is taken to be the interaction energy of an infinitely distant particle with the crystal surface; the arguments of the δ functions correspond to the nearest-neighbor and next-nearest neighbor distances the crystals with the zinc blende structure.

The rates of evaporation and surface migration are given, respectively, by

$$D = D_0 \exp(-E/kT_s), \tag{2}$$
$$R = R_0 \exp(-(E - E_d)/kT_s), \tag{3}$$

where E is the binding energy of a particle, E_d is a surface migration parameter, which is determined by the breaking of a half a bond in the regular surface, D_0 and R_0 are rate constants, k is Boltzmann's constant, and T_s is the substrate temperature.

The constants in expressions (1)–(3) were calculated from experimental data. The following values were obtained: $E_1 = 1.0$ eV, $E_2 = 0.1$ eV, $R_0 = 1.2 \times 10^{13}$ s^{-1}, and $D_0 = 3.2 \times 10^9$ s^{-1} (Ref. 6). The simulation was set up in the following way. A number of Ga atoms were deposited onto the surface so as to fill a monolayer (the matrix contained 30×30 lattice sites) and then were followed by a number of As molecules equal to the product of the number of deposited Ga atoms times the specified flux ratio. It was assumed that no impurity centers or interstitial defects were present, and segregation of like particles was neglected. The distribution gradients of the fluxes over the surface and the sample temperature gradient were taken to be zero. In the analysis,
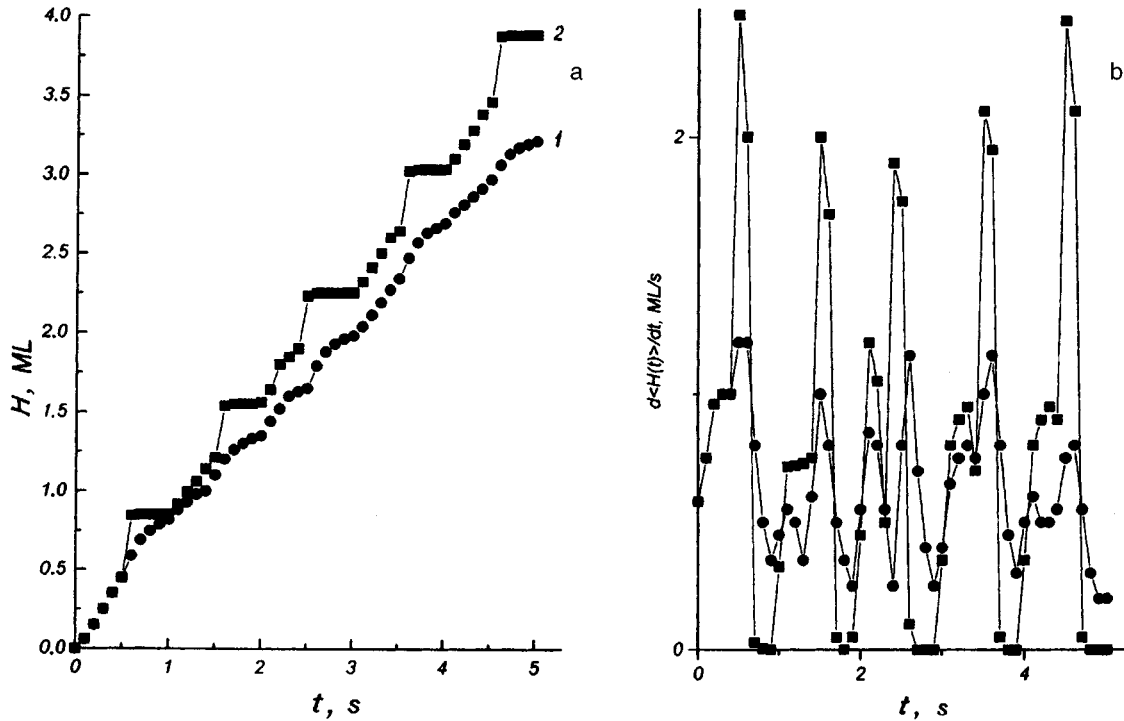
FIG. 1. Time dependence of the average height (a) and the derivative of the average height with respect to the time (b) for a substrate temperature of 700 K and arsenic to gallium flux ratios 1 (*1*) and 10 (*2*).

in-layer and interlayer migration was taken into account. The initial surface for the growth was the As-stabilized GaAs(100) surface tilted by 0.95° towards the [011] direction. The growth rate corresponded to the deposition of one monolayer on the surface per second.

The results of the simulation were presented in the form of the time dependence of the average height $\langle H(t)\rangle$ and the average roughness $\sigma(t)$ of the surface, calculated from the formula

$$\sigma(t) = \sqrt{(1/N)\sum_{i,j} (\langle H(t)\rangle - H_{i,j}(t))^2}, \qquad (4)$$

where N is the number of unit cells in the layer and $H_{i,j}(t)$ is the height of the layer at a given location i,j at time t. The results were averaged in a series of five independent computer runs with identical growth conditions. The standard deviation of the average values of the quantities was not higher than 5%.

Figure 1 shows typical plots of the mean height as a function of time for various flux ratios J_{As}/J_{Ga}. It shows that $\langle H(t)\rangle$ has a stepwise-linear shape (this is more evident in the function $d\langle H(t)\rangle/dt$, which is more pronounced at higher values of J_{As}/J_{Ga}. The stepped behavior can be explained by the nature of the direction of the fluxes on the substrate surface in migration-stimulated epitaxial growth. Indeed, if the shutter on the gallium source is opened, Ga is deposited uniformly on the underlying As layer, and the initial stage of growth of the monolayer is eliminated. In this time interval the adatom concentration is low and lateral interaction between surface Ga atoms is essentially nonexistent. After further deposition (after ~ 0.1 monolayer cover-

age), this kind of interaction can no longer be neglected, and quasistable two-dimensional clusters are formed on the surface. The growth proceeds by the joining of atoms to form nuclei, and there is almost no desorption. This produces the linear section of the function $\langle H(t)\rangle$ until the shutter on the gallium source is closed and the shutter of the As source is opened. Since the As is diatomic, the rate of filling the As sublattice is twice that of Ga, assuming 100% chemisorption of the dissociated molecules, beginning with $J_{As}/J_{Ga}=1$ (because of desorption this rate may be somewhat lower). In this way, a segment appears on the curve of $\langle H(T)\rangle$ where the average height increases more sharply. Of course, an increase in the flux ratio makes the function $\langle H(t)\rangle$ nearly step-shaped. The presence of a part of the curve where the average height is independent of the deposition time before the arsenic source is turned off is explained by the fact that all the configurations of the Ga atoms on the underlying layer up to this time are occupied, and the excess arsenic re-evaporates from the surface (the sticking coefficient of As on As at these temperatures is zero).

It has been found that the surface roughness as a function of time oscillates over a wide ranges of substrate temperature flux ratio (an example is shown in Fig. 2a). With increasing substrate temperature the surface roughness falls off until $T_s \sim 750$ K, and then $\sigma(t)$ increases independently of the arsenic pressure P_{As}. However, while the value of $\sigma(t)$ remains essentially constant with increasing P_{As} at these low temperatures, when T_s is increased to 750 K, the surface roughness decreases somewhat with increasing arsenic pressure, which is demonstrated in Fig. 2b, where the values of $\sigma(t)$ are shown after five seconds of deposition.
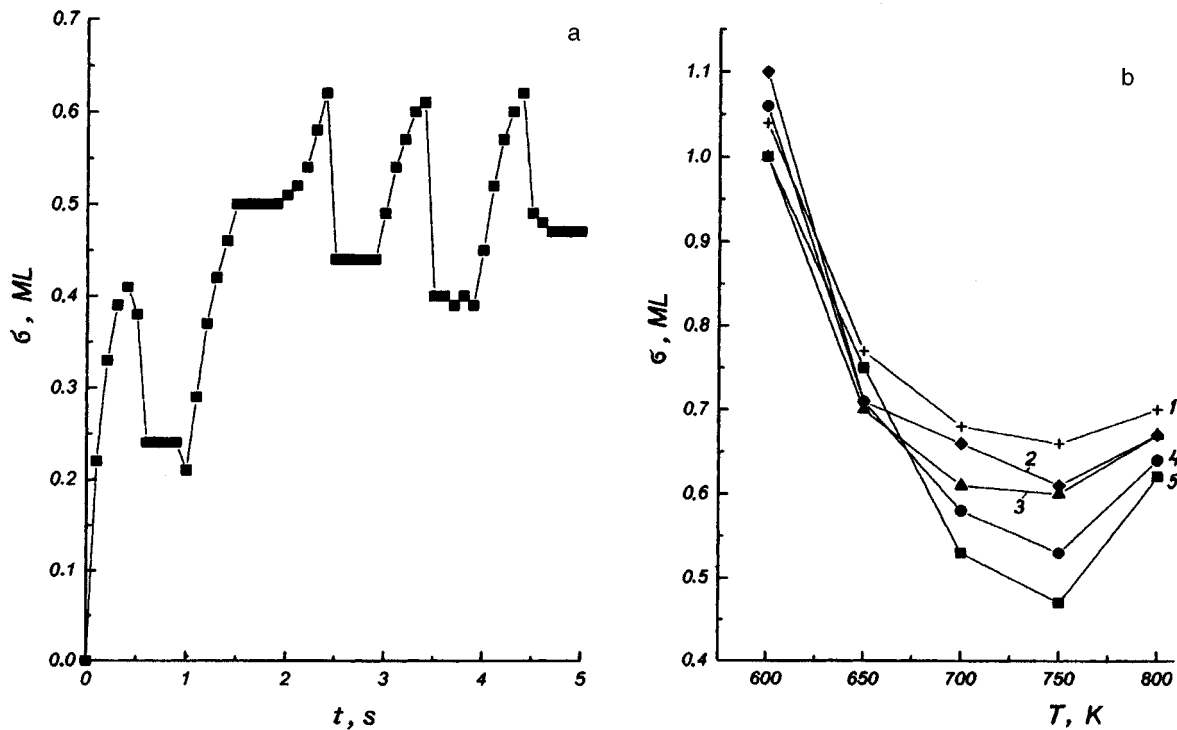
FIG. 2. a — Time dependence of the surface roughness at a substrate temperature of 750 K and an arsenic to gallium flux ratio of 10; b — dependence of the surface roughness on the substrate temperature for various flux ratios: *1* — 1, *2* — 2, *3* — 3, *4* — 5, *5* — 10.

Similar dependences have also been observed experimentally in Refs. 8 and 9, where migration-stimulated epitaxial growth was studied by *in situ* methods of surface photoabsorption and reflection high-energy electron diffraction. It was shown that when the arsenic pressure is increased and the substrate temperature is lowered (to certain values), the quality of the crystal-vacuum interface is improved.

In conclusion it should be pointed out that these results indicate a lower surface roughness, by a factor of 1.5–2, as compared to molecular beam epitaxy,[10] which demonstrates the advantage of using migration-stimulated epitaxy for producing unique devices for microelectronics and optoelectronics. This is particularly important in the use of strained systems (for example, InGaAs/GaAs), in which quantum dots are formed because of the effects of self-organization,[11,12] and the spread in the sizes of the nanoobjects is considerably less with the use of submonolayer migration-stimulated epitaxy.

[1] H. Sakaki, M. Tanaka, and J. Yoshimo, J. Jpn. Appl. Phys. **24**, L417 (1985).

[2] S. Shimizu, O. Tsukakoshi, S. Komiya, and Y. Makita, J. Vac. Sci. Technol. B. **3**, 554 (1985).

[3] H. Yamaguchi, M. Kawashima, and Y. Horikoshi, Appl. Surf. Sci. **33/34**, 406 (1988).

[4] C. T. Foxon, J. Crystal Growth **95**, 11 (1989).

[5] S. Nagata and T. Tanaka, J. Appl. Phys. **48**, 940 (1977).

[6] A. G. Filaretov and T. É. Tsyrlin, Fiz. Tverd. Tela (Leningrad) **33**, 1329 (1991) [Sov. Phys. Solid State **31**, 751 (1991)].

[7] J. R. Arthur, Surf. Sci. **43**, 449 (1974).

[8] Y. Horikoshi, M. Kawashima, and N. Kobayashi, J. Crystal Growth **111**, 200 (1991).

[9] Y. Takamo, M. Lopez, T. Torihata, T. Ikei, Y. Kamaya, K. Pak, and H. Yonezu, J. Crystal Growth **111** 216 (1991).

[10] G. E. Cirlin, in *Proceedings of the 4th International Conference on Physics Computing*, ed. by R. de Groot and J. Nadrchal, (World Scientific), pp. 303–304.

[11] G. E. Cirlin, G. M. Guryanov, A. O. Golubok, S. Ya. Tipissev, N. N. Ledentsov, P. S. Kop'ev, M. Grundmann, and D. Bimberg, Appl. Phys. Lett. **67**, 97 (1995).

[12] G. M. Guryanov, G. E. Cirlin, V. N. Petrov, N. K. Polyakov, A. O. Golubok, S. Ya. Tipissev, V. B. Gubanov, Yu. B. Samsonenko, N. N. Ledentsov, V. A. Shchukin, M. Grundmann, D. Bimberg, and Zh. I. Alferov, Surf. Sci. **352–354**, 651 (1996).

Translated by J. R. Anderson

New properties created in metal−oxide−silicon structures by reducing their dimensional parameters to the nanometer range

G. G. Kareva

St. Petersburg State Technical University

An experiment has been carried out in which standard metal−oxide−silicon barrier structures are used to develop resonance tunneling of electrons. The result is an extension in the array of properties of the structure. In particular, the capacitance−voltage characteristics take on resonance features: steps and peaks in one range of applied voltage and the classical behavior in another. The number of resonance features can be controlled by the applied voltage. Hysteresis observed in the capacitance−voltage characteristics indicates that the structure is multistable, that it has the property of memory, that electron charge can be written and erased. © *1997 American Institute of Physics.* [S1063-7850(97)03002-4]

The oxide thickness and the extent of the space-charge region in a semiconductor in standard metal−oxide−silicon structures has been reduced to nanometer dimensions. The nanostructure proposed here is a double-barrier structure,[1–4] and by means of the field effect one can create conditions for resonance tunneling of electrons, which can be seen in resonance features in the capacitance−voltage characteristics in the appropriate range of applied voltage, along with the conventional behavior of the characteristics[5,6] in another voltage range. Thus a single metal−oxide−silicon (MOS) nanostructure combines the properties of a MOS structure[5,6] and an artificially periodic structure,[1–4] depending on the range of operating voltage.

To clarify how this double barrier is constructed and how it operates, Fig. 1 shows the energy band diagram of the metal−oxide−semiconductor nanostructure for voltages that induce resonance tunneling of electrons from the semiconductor to the metal. One part of the double barrier (B_2) is the tunneling-thin oxide prepared as explained in Ref. 7. The other part of the double barrier (B_1) is a barrier layer of a tunneling-thin $p-n$ junction formed in the heavily boron-doped silicon by the field effect in the metal−oxide−semiconductor structure. The high doping level, in the range 10^{18}–10^{20} cm^{-3}, provides the required tunneling transmission of the barrier layer B_1 and makes the quantum well (W), which is part of the surface space-charge region, narrow enough for the required quantization. The depth of the well changes with the voltage. With the onset of resonance tunneling it exceeds the band gap of the semiconductor, i.e., 1.1 eV. Such a deep quantum well is favorable for observing resonance features at room temperature. The double barrier is asymmetric. To induce resonance tunneling through the quantization levels of the well it is necessary to apply the correct voltage to line up the quantization levels with the emitting level, which in the present case is the Fermi level in the bulk of the semiconductor (Fig. 1). The minimum voltage for which the lowest level (0) of the quantum well lines up with the Fermi level will be called the threshold voltage V_{th}.

For negative voltages less in magnitude than the threshold and for positive voltages the conditions for resonance tunneling are not met, and the metal−oxide−semiconductor structure operates in the standard mode, which is also confirmed by the capacitance−voltage characteristic (Fig. 2, the dashed line), which has the ordinary shape[5,6] with a transition from the capacitance C_0 of the upper plateau, determined mainly by the oxide region, to the capacitance C_{sp} of the lower plateau, which is determined mainly by the space-charge region of the semiconductor. The value of C_0 as well as the ratio C/C_{sp} reflects an oxide thickness in the range 1−5 nm. The additional reduction of the capacitance, which causes the bend in the curve at $V = -0.9$ V, indicates the onset of nonequilibrium depletion of the space-charge region under conditions of a tunneling current. The range of operating voltage where the metal−oxide−semiconductor structure has the ordinary capacitance−voltage characteristic may be termed the classical range, in contrast to the quantum range, which begins at $|V| > |V_{th}|$.

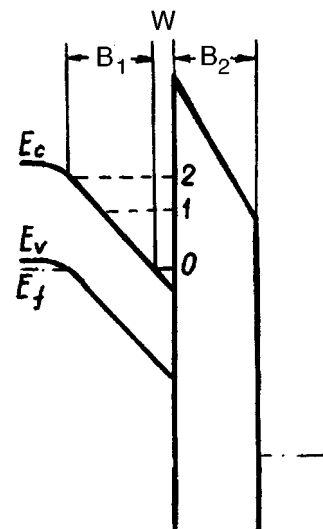For $-V = -V_{th}$ the lowest miniband in the quantum well

FIG. 1. Energy band diagram of a metal−oxide−semiconductor nanostructure for a voltage that produces resonance tunneling of electrons from the semiconductor to the metal through the quantized levels of the well of the space-charge region of the semiconductor.
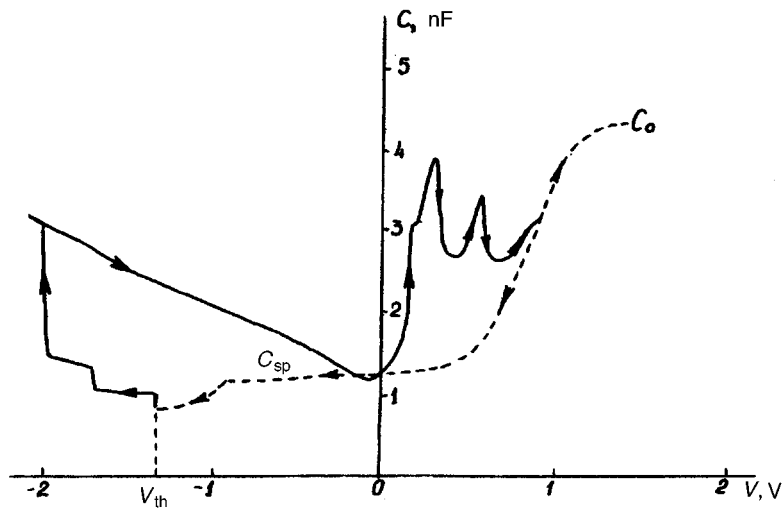
FIG. 2. Typical behavior of the high-frequency (10^5 Hz) capacitance–voltage characteristics of nano-MOS structures based on p-type silicon ($N_A = 8 \times 10^{18}$ cm^{-3}); the sweep rate is ~ 10 V/min.

lines up with the Fermi level in the bulk of the semiconductor, which brings about the possibility of resonance tunneling of electrons from the Fermi level through the miniband into the metal. This is reflected in a step-wise increase in the capacitance (Fig. 2). With increasing negative voltage the higher-lying minibands in the quantum well reach the Fermi level, and they then are switched into resonance tunneling and produce new steps in the capacitance–voltage characteristic. Because of the shape of the well, the levels become closer together in energy in going from lower to higher energies. Consistent with this occurrence is the decrease in the spacing between the steps with increasing voltage.

One of the features of the capacitance–voltage characteristics of metal–oxide–semiconductor nanostructures that is advantageous for their practical use, in particular in memory applications, is the hysteresis in the controlling voltage during operation of the structure in the resonance tunneling mode (Fig. 2). A necessary condition for the hysteresis to occur is that a negative voltage greater in magnitude than $-V_{th}$ be exceeded. The greater the negative voltage, the sharper the hysteresis. In one cycle of hysteresis the capacitance C is larger in the reverse path of the cycle than in the forward path over most of the range of V. For $V > 0$, the capacitance–voltage characteristic in the reverse path shows a peak (Fig. 2). The larger the step passed over for $V < 0$ in the forward path, the higher the peak for $V > 0$ in the reverse path. The final result of the action of the positive polarity in the hysteresis cycle is that the structure returns to its initial state with the initial capacitance–voltage characteristic, which is maintained until the negative threshold voltage is again exceeded, and thus the next time the characteristic of the structure can be restored to its initial state by means of a voltage $V > 0$. These cycles can be repeated many times with different numbers of steps and cycles.

The observed hysteresis is most likely due to the following circumstances. It can be seen that an increase in the negative voltage with $|V| > |V_{th}|$ results not only in resonance

tunneling, but also in the sequential conversion of all the high-lying minibands from empty to full, and as a consequence electronic charge is accumulated in the quantum well. The charge state of the quantum well is changed relative to its original state.

These results indicate that the accumulated charge is retained after the external voltage is removed. This is entirely possible if the electron gas is not two-dimensional, but zero-dimensional. The cause of the reduction in the dimension of the gas may be nonuniformities in the nanostructure over the surface. Because of the accumulated and retained charge in the quantum dots, resonance tunneling of electrons from the metal to the semiconductor is possible through the quantized levels of the dots for $V > 0$, as is indicated by the peaks that appear on the characteristic, which are absent in the original structure. The peaked nature of the resonance features (as opposed to the stepped shape for the opposite polarity of the voltage V) reflects consistently the energy details of the collector in the form of a gap between the Fermi level and the top of the valence band of the semiconductor. An increase in the positive voltage is accompanied by resonance tunneling from the metal into the semiconductor through even deeper quantum minilevels. In addition, this increase in the voltage converts the quantized levels from filled to empty, and in the end restores the structure to its original charge state, as is indicated by its characteristic and its behavior.

In summary, it has been shown in the context of the capacitance–voltage characteristic that the metal–oxide–semiconductor nanostructure studied in these experiments, in addition to displaying classical behavior, can also:

1) Support resonance tunneling of electrons from the semiconductor to the metal and from the metal to the semiconductor and display a characteristic with resonance features: steps for one voltage polarity and peaks for the other.

2) Record electron charge with one polarity and erase it with the other, thus inducing multistability in the structure.

[1] L. L. Chang, L. Esaki, and R. Tsu, Appl. Phys. Lett. **24**, 593 (1974).

[2] L. Esaki, IEEE. J. Quantum. Electron. **QE-22**, 1611 (1986).

[3] F. Capasso, K. Mohammed, and A. Y. Cho, IEEE J. Quantum. Electron. **QE-22**, 1853 (1986).

[4] F. Capasso, S. Sen, and F. Beltram, *High-Speed Semiconductor Devices* (Wiley, New York, 1990).

[5] A. Goetzberger, Bell Syst. Tech. J. **45**, 1097 (1966).

[6] S. M. Sze, *Physics of Semiconductor Devices* (Wiley, New York, 1981).

[7] G. G. Kareva, Patent ''Superlattice'' Russian Federation, No. 2 062 529, Bulletin No. 17, 1996.

Translated by J. R. Anderson

Intense luminescence with a tunable wavelength from films of tetrahedral amorphous hydrogenated carbon on a fused quartz substrate

M. E. Kompan, O. I. Kon'kov, E. I. Terukov, I. N. Trapeznikova, and I. Yu. Shabanov

A. F. Ioffe Physicotechnical Institute, Russian Academy of Sciences, St. Petersburg

A model is proposed for a new type of optoelectronic device that utilizes the luminescence of a film of *ta*-C:H in the plane of a fused quartz substrate. It is observed that the luminescence radiation propagating in the interior of the substrate becomes highly monochromatized. However, along the normal to the plane of the substrate luminescence occurs over a broad wavelength range, as is typical of *ta*-C:H. Visually this luminescence is white, while the color of the luminescence in the plane of the substrate depends on the film thickness. A film with a variable thickness yields radiation with a color that varies from turquoise to red. This monochromatization effect in a film/substrate system is observed for the first time. © *1997 American Institute of Physics.* [S1063-7850(97)03102-9]

In recent years researchers have paid a great deal of attention to films of tetrahedral amorphous carbon (*ta*-C:H) and diamond-like carbon. Hitherto, the intrinsic luminescence properties of these materials have not been regarded as a source for general application. Nonetheless, it is known that the luminescence of *ta*-C:H is easily excited by ultraviolet and visible light. With excitation by ultraviolet light (337 nm) the luminescence band covers nearly the entire visible range (from 450 to 650 nm at 25% of peak level), and the luminescence efficiency reaches 0.2 (Refs. 1 and 2), which is comparable with the luminescence efficiency of the well known laser dyes such as okasine.

In the work reported here we carried out experiments to use the luminescence properties of *ta*-C:H and the structural properties of the films prepared on the substrates to develop a prototype of a high-power source of visible radiation with a tunable wavelength. We used the properties of the film-on-substrate system, which is a kind of monochromator for the radiation channeled in the interior of the transparent substrate.

Let us consider the path of a ray in such a system (Fig. 1). The capability of a film with a thickness of the order of the wavelength of light to produce interference coloring in reflected light is well known. However, in the present case the source of radiation is inside the film, and the luminescence is emitted isotropically, so that monochromatization by the ordinary interference mechanism cannot occur, since light of different wavelengths is superimposed and it emerges at various angles, again producing white light. However, a two-layer system, as shown in Fig. 1, has the capability of monochromatizing white light emitted by the film. The presence of a substrate with a refractive index (n_s) having a value intermediate between that of air n_0 and of *ta*-C:H (n_f)

$$n_0 < n_s < n_f$$

permits angular selection of the radiation channeled in the interior of the substrate. The first separation of the luminescence light in direction occurs at the film-substrate interface. The luminescence light propagating in the film at an angle to the normal greater than $\alpha 1$, the limiting angle of total internal reflection for the film/substrate interface, is channeled in the luminescent film itself, and does not escape into the substrate. In a similar way the light incident on the substrate is separated at the substrate–air interface. The rays that propagate in the substrate at an angle to the normal equal to the angle of total internal reflection ($\alpha 2$) and larger cannot escape from the film and is channeled by the substrate.

The light propagating at a smaller angle to the normal escapes from the substrate. The direction of propagation of
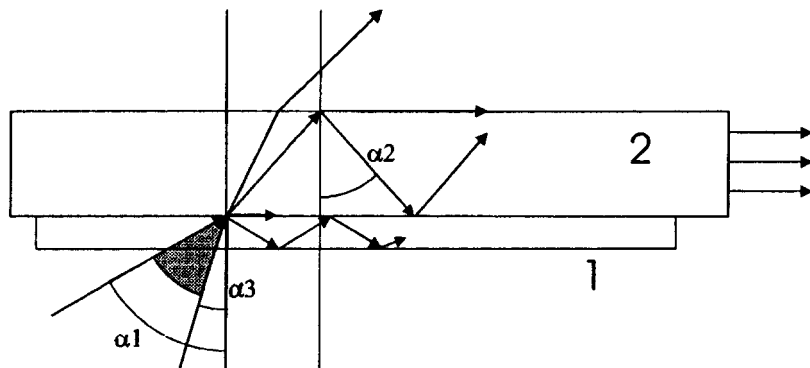

FIG. 1. Principle of monochromatization in a two-layer system — a *ta*-C:H film (*1*) on a fused quartz substrate (*2*). The notation is explained in the text.

the luminescence light in the film, which after refraction will correspond to the angle of total internal reflection in the substrate, is denoted as $\alpha 3$. Thus the substrate can collect the luminescence radiation that was initially emitted in the ta-C:H film in the range of angles between $\alpha 1$ and $\alpha 3$ from the normal. The angular selection of the radiation due to the double-layer nature of the system allows us to regard the interference in the emitting film as ordinary interference for light propagating in a narrow range of angles, which results in monochromatization of the luminescence observed from the end of the substrate. The thickness of the film emitting the light is a parameter that determines the wavelength of the luminescence light at the maximum, since, of the usual parameters determining the condition for interference in a thin film — the angle of propagation of the light and the thickness — the former is dictated by the conditions of total internal reflection.

The ta-C:H film was prepared by decomposition of a methane–argon mixture, 10% CH_4–90%Ar, in an rf glow discharge.[3] The material was deposited on a fused quartz substrate ($n_s = 1.4$ at 150 °C). The film thickness at the maximum was 0.8 μm. A thickness gradient was formed by placing the substrate at the edge of the discharge gap in the reaction chamber, and was 0.5 μm in a distance of 10 mm. The refractive index of the film was 2.4 and did not depend on the thickness.

The luminescence spectra of the films with excitation by a source of light with a photon energy from 1.83 to 3.68 eV were measured at room temperature. For an excitation photon energy of 2.9–3.68 eV the spectra had essentially the same shape, with the following parameters: $h\nu_{max} = 2.2$ eV, halfwidth 0.8 eV, quantum efficiency 0.15. Subsequent decrease in the excitation photon energy changes the shape of the spectrum by cutting off its high-energy tail; the halfwidth of the luminescence is reduced, and the peak is shifted towards lower energies.[4,5]

It should be emphasized that this luminescence is observed when the spectrum is measured normal to the plane of the substrate. However, the luminescence spectrum measured at the end of the substrate is found to be different for different film thicknesses.

In Fig. 2 we show the luminescence spectra for a ta-C:H film with a variable thickness, recorded from the end of the substrate with excitation by laser light with $\lambda = 337$ nm. The emitting film is uniform in composition, as is confirmed by checking the spectra of the emission along the normal to the substrate. The spectra shown in the figure were obtained for different points of the film by a simple displacement of the sample in the plane. Visually the color of the emission from the end of the substrate changed from turquoise to red during this displacement. This result confirms
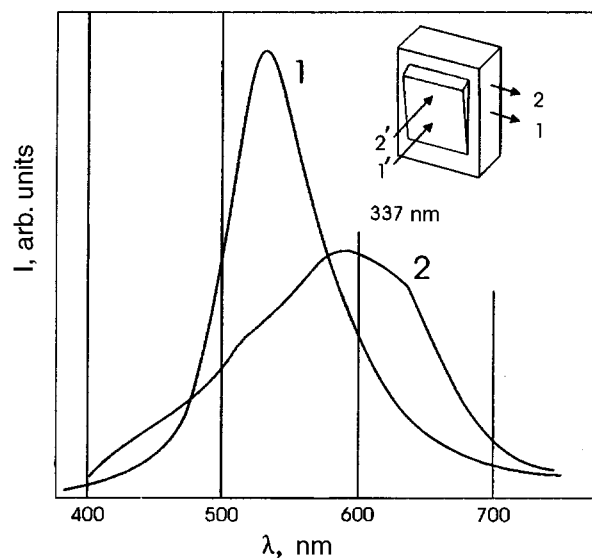

FIG. 2. Luminescence spectra of a ta-C:H film with a variable thickness, measured at the end of the substrate. The spectra shown in this figure and designated *1* and *2* were obtained for the corresponding points of the film by a simple translation of the sample in the plane, as shown in the inset. The thickness of the film at point *1* is 0.4 μm and at point *2* is 0.7 μm. *1′* and *2′* are the excitation beams.

the principle of monochromatization enunciated above. To the best of our knowledge, the proposed method of monochromatization has never been used before.

It should also be noted that in studying how the shape of the spectra depends on the intensity of the exciting light we observed a change in the width of the band. This indicates that superradiance may occur in the ta-C:H system, and this proposed light source may be a kind of new type of solid-state laser with a tunable wavelength.

I thank B. P. Zakharchenya for a discussion of the experimental results.

[1] V. A. Vasil'ev, A. S. Volkov, E. Musabekov, and E. I. Terukov, Pis'ma Zh. Tekh. Fiz. **14**, 1675 (1988) [Sov. Tech. Phys. Lett. **14**, 729 (1988)].
[2] S. V. Chernyshov, E. I. Terukov, V. A. Vassilyev, and A. S. Volkov, J. Non-Cryst. Solids **134**, 218 (1994).
[3] O. I. Kon'kov, E. I. Terukov, and I. N. Trapeznikova, Fiz. Tekh. Poluprovodn. 1997 (in press) [Semiconductors].
[4] V. A. Vasil'ev, A. S. Volkov, E. Musabekov, E. I. Terukov, and S. V. Chernyshev, Fiz. Tverd. Tela (Leningrad) **32**, 784 (1990) [Sov. Phys. Solid State **32**, 462 (1990)].
[5] V. A. Vasil'ev, E. I. Terukov, I. N. Trapeznikova, and V. E. Chelnokov, Fiz. Tekh. Poluprovodn. **30**, 1621 (1996) [Semiconductors **30**, 849 (1996)].

Translated by J. R. Anderson

The following two papers represent the last work of Professor Aleksander Semenovich Tager, Doctor of Technical Science. These papers were left on his desk after his sudden and unexpected death on January 1, 1996, in his seventieth year, and were prepared for publication by his colleagues and friends.

A. S. Tager participated in world science as the creator of a new class of semiconductor device, the avalanche diode. This great achievement was recognized by the Lenin prize.

In later years he brought forth a number of new devices that utilize the principle of longitudinal ballistic transport in nonuniform quantum-well structures.

The content of these papers represents the development of these ideas.

A. S. Tager was a steady contributor to our journal and a close friend to many of us. We regard it as an honored duty to introduce his papers with a short preface in his memory.

The Editorial Board

Spin splitting in longitudinal carrier transport in quantum structures

A. S. Tager[1]

State Scientific-Industrial Enterprise "Istok," Fryazino

The role of spin effects in electron waveguides is analyzed. It is shown that in noncentrosymmetric structures where the spin splitting is odd in the wave vector the phase velocity of the electron waves depends on the spin orientation. On the one hand this destroys the conditions for interference and degrades the characteristics of the device; but on the other hand it allows one in principle to obtain a beam of completely spin-polarized electrons from the exit. © *1997 American Institute of Physics.* [S1063-7850(97)03202-3]

A topic of active discussion concerns the means of making nanoelectronic devices of various kinds on the basis of the longitudinal transport of electrons in low-dimensional ($2D$, $1D$) quantum structures (electron waveguides). To analyze the possible characteristics of these devices we invoke the well-known analog between electron and electromagnetic waves. However, in all papers known to the author, including those dealing with the development of methods for detailed numerical calculations of the characteristics of the devices,[1,2] those investigators did not take into account the specific details of the electron waves related to the electron spin. Moreover, as is known,[3,4] spin-splitting occurs in crystals without a center of inversion, such as the III–V compounds, as well as in asymmetric quantum wells — the spin degeneracy is lifted for all electrons with quasimomentum $\mathbf{k} \neq 0$. As a result, a monoenergetic flux of charge carriers moving, for example, along a quantum well or in quantum wire with a wave vector $\mathbf{k}(k_\parallel, k_\perp)$, where $k_\parallel^2 = k_x^2 + k_y^2$ and $k_\perp \equiv k_z$, with $Z \parallel (001)$, will be split into two independent fluxes, each of which has its own dispersion relation

$$\varepsilon^\pm(K) = \frac{\hbar^2 k_\pm^2}{2m} \pm \gamma k_\pm \langle k_z^2 \rangle, \tag{1}$$

where $2\pi\hbar$ is Planck's constant and m is the effective mass of the carrier.

$$k_\pm \equiv k_\parallel \equiv (k_x^2 + k_y^2)^{1/2},$$

$$\langle k_z^2 \rangle = \int_{-\infty}^{\infty} |\frac{\partial^2 \psi}{\partial z^2}| dz, \quad \psi \sim \exp(j\mathbf{k}_\parallel \cdot \mathbf{r}) \psi(z)$$

is the wave function of the charge carrier in the quantum well and γ is a coefficient that depends on the band structure parameters of the semiconductor.

For a given total carrier energy ε Eq. (1) yields the equation for the longitudinal momentum of the electrons with like spin

$$k_\pm^2 \pm 2\varkappa k_\pm - k_0^2 = 0, \tag{2}$$

from which we obtain

$$k_\pm = \mp \sqrt{\varkappa^2 + k_0^2} \mp \varkappa. \tag{3}$$

Here

$$\varkappa = \frac{1}{2} D\gamma \langle k_z^2 \rangle, \quad D = \frac{2m}{\hbar^2}, \quad k_0^2 = D(\varepsilon - \varepsilon_\perp),$$

$$\varepsilon_\perp = \frac{\langle k_z^2 \rangle}{D}. \tag{3a}$$

The charge carriers injected into the quantum well (quantum wire) with an energy ε are distributed over n subbands corresponding to discrete longitudinal energies $\varepsilon_{\perp n} = \langle k_{zn}^2 \rangle / D < \varepsilon$. According to Eq. (3) in each subband electron waves propagating along the well (wire) with different phase velocities $\nu_\pm = \varepsilon / \hbar k_\pm$ correspond to charge carriers with opposite spins. Since the principle of operation of the planned nanoelectronic devices with longitudinal transport (such as directional couplers for electron waves, electron filters, switches, interference transistors, etc.) is closely tied to the phase shifts of the electron waves along the sections of the electron waveguides, the effect of spin splitting can have a large effect on the basic characteristics of the devices.

By way of example, let us estimate how this effects makes itself felt in a single-channel interference transistor,[5] based on the interference of electron waves corresponding to electrons from the adjacent energy subbands (channels) $n = 1, 2$. If electrons with energies ε injected into a section of the electron waveguide of length l are distributed evenly between these subbands, then the normalized wave function at the exit from the waveguide can be written as

$$\psi = \frac{1}{2}(e^{jk_1+l} + e^{jk_1-l} + e^{jk_2+l} + e^{jk_2-l}), \tag{4}$$

where $k_{n\pm}$ are the solutions of Eq. (2) for $\langle k_z^2 \rangle = \langle k_{zn}^2 \rangle$, $n = 1, 2$. If the difference between the longitudinal quasimomenta of the electrons with opposite spin is small, $\varepsilon^2 \ll k_0^2$, then, according to Eq. (3), $k_\pm \simeq k_0 \pm \varkappa$ and Eq. (4) gives

$$|\psi|^2 = 1 + \cos[(k_{01} - k_{02})l]\cos[(\varkappa_1 - \varkappa_2)l]. \tag{5}$$

Therefore the spin splitting can substantially change the conditions for interference suppression of the current at the exit from the waveguide. For complete suppression, not one, but two independent conditions must be satisfied:

$(k_{01}-k_{02})l=(2m+1)\pi$ and $(\varkappa_1-\varkappa_2)l=2s\pi$, or $(k_{01}-k_{02})l=2m\pi$ and $(\varkappa_1-\varkappa_2)l=(2s+1)\pi$, with $m,s=0,1,2,\ldots$. Similarly the condition for the transformation of the electron waves in coupled electron waveguides is made more complicated.[2] In principle, this should degrade the characteristics of the associated devices, reduce the directional coefficient and the decoupling coefficient of directional couplers, and in the efficiency of electron switches and the selectivity of filters, etc. However, the magnitude of the spin splitting and consequently its contribution to the characteristics of the devices may be small; this depends to a large degree on the properties of the semiconductor materials and the manner in which the electron waveguides are constructed — their crystallographic orientation, the presence of built-in electric fields, etc. Let us make some estimates. The contribution of the spin splitting to the interference effects is given by the ratio

$$\varkappa_n/k_0=\frac{1}{2}\gamma\frac{D^{3/2}\varepsilon_{\perp,n}}{(\varepsilon-\varepsilon_{\perp,n})^{1/2}}. \tag{6}$$

The parameter γ depends on the band structure of the material. According to Ref. 4,

$$\gamma=\frac{\alpha\hbar^3}{(2m^3\varepsilon_g)^{1/2}}, \quad \alpha\simeq M\frac{m}{m_0}\eta\left(1-\frac{1}{3}\eta\right)^{-1/2},$$
$$\eta=\frac{\Delta}{\varepsilon_g+\Delta}, \tag{7}$$

where ε_g is the band gap, Δ is the minimum of the hole energy in the split-off band, m_0 is the free-electron mass, and M is a numerical coefficient of the order of unity.

According to Eqs. (3) and (7) the product

$$\gamma D^{3/2}=\frac{1}{2}\frac{\alpha\hbar^3}{(2\varepsilon_g)^{1/2}m^{3/2}}\left(\frac{2m}{\hbar^2}\right)^{3/2}$$
$$=\alpha/\varepsilon_g^{1/2}=M\frac{m}{m_0}\eta\left(1-\frac{1}{3}\eta\right)^{1/2}\varepsilon_g^{-1/2}, \tag{8}$$

so that

$$\varkappa_n/k_0=\left(\frac{\varepsilon_{\perp,n}}{\varepsilon-\varepsilon_{\perp,n}}\right)^{1/2}\left(\frac{\varepsilon_{\perp,n}}{\varepsilon_g}\right)^{1/2}. \tag{9}$$

In GaAs ($\Delta=0.34$ eV, $m_e=0.067m_0$, $\varepsilon_g=1.5$ eV), the result is $\eta\simeq0.18$ so for electrons we have

$$\alpha_e\simeq10^{-2}M, \tag{10}$$

and for the heavy holes ($m_h\simeq0.5m_0$)

$$\alpha_h\simeq7.5\times10^{-2}M. \tag{11}$$

For InSb ($\varepsilon_g=0.234$ eV, $m_e\simeq0.013m_0$, $\Delta-0.81$ eV), $\eta(1-(1/3)\eta)\simeq1$, and

$$\alpha_e\simeq1.3\times10^{-2}. \tag{12}$$

Since the carrier energy does not exceed ε_g and the difference $\varepsilon-\varepsilon_\perp$ cannot be made much smaller than $\varepsilon_\perp$, we find that

$$[\varepsilon_{\perp_n}/(\varepsilon-\varepsilon_{\perp_n})]^{1/2}(\varepsilon_{\perp_n}/\varepsilon_g)^{1/2}\lesssim1.$$

Therefore, for electrons in GaAs and InSb,

$$(\varkappa/k_0)_e\lesssim10^{-2}M,$$

and for holes in GaAs

$$(\varkappa/k_0)_h\lesssim0.1M.$$

For the sake of comparison, let us estimate $\varkappa/k_0$ from the data of Refs. 3 and 6. In Ref. 3 the spin splitting is written as

$$\frac{1}{2}\Delta\varepsilon=\beta k_\parallel. \tag{13}$$

In the notation of Eqs. (1)–(3)

$$\frac{1}{2}\Delta\varepsilon=\gamma k\langle k_z^2\rangle=2\varkappa/Dk_0.$$

Consequently,

$$\varkappa=\frac{1}{2}\beta D. \tag{14}$$

For a two-dimensional gas with a concentration η_S

$$(k_\parallel)_F\equiv k_{OF}=(2\pi n_S)^{1/2}. \tag{15}$$

at the Fermi level. For $n_S=5\times10^{11}$ cm^{-2}, we obtain $k_{0F}=1.77\times10^6$ cm^{-1}. According to Ref. 6, the following values are correct for electrons in GaAs

$$\beta=2.5\times10^{-10}\text{ eV}\cdot\text{cm}\equiv4\times10^{-31}\text{ J}\cdot\text{m},$$
$$\varkappa=\frac{1}{2}\beta D_e=\frac{m_e}{\hbar^2}\beta=2.7\times10^4\text{ cm}^{-1}, \tag{16}$$
$$\frac{\varkappa_e}{k_{OF}}\simeq1.5\times10^{-2}. \tag{17}$$

For holes with $m_h=0.5m_0$, $\beta\simeq10^{-30}$ J$\cdot$m,

$$\varkappa_h=\frac{1}{2}\beta D_h=5\times10^5\text{ cm}^{-1}, \tag{18}$$
$$\varkappa_h/k_0\simeq0.28. \tag{19}$$

For electrons in InSb ($m_e=0.013m_0$; Ref. 6),

$$\Delta\varepsilon=1.61\text{ meV}.$$

Consequently,

$$\beta=\frac{1}{2}\frac{\Delta\varepsilon}{(k_0)_F}=7.2\times10^{-31}\text{ J}\cdot\text{m},$$
$$\varkappa_e=\frac{1}{2}\beta D_e\simeq9.4\times10^3\text{ cm}^{-1}. \tag{20}$$
$$\varkappa_e/k_0\simeq0.53\times10^{-2}. \tag{21}$$

A comparison of formulas (9)–(12) with formulas (17), (19), and (21) shows that both approaches give values of the same order of magnitude for the ratio $(\varepsilon/k_0)_e\simeq10^{-2}$ for electrons in GaAs and InSb. For these small values of $\varkappa/k_0$ the effect of spin splitting on the interference of electrons at distances of several wavelengths is not important. It should be pointed out, however, that while the size of the device (the length of the waveguide) is quite large, in the absence of scattering the condition $(\varkappa_1-\varkappa_2)/l\sim2\pi$ can in principle be satisfied, and

then the spin splitting becomes important. In particular, in GaAs these effects can be observed at 77 K and at waveguide lengths of about 1 μm.

For the heavy holes in GaAs the spin splitting is found to be quite large, particularly according to the data of Ref. 6. If the estimate of Eq. (19) is correct, then it is reasonable to try to separate the spin-oriented flux of heavy holes in GaAs/AlGaAs heterostructures. As a result of interference of electrons of like spin orientation ($S = \pm 1/2$) injected into the waveguide from adjacent subbands, the intensities of the corresponding electron waves at the end of the waveguide ($x = l$) are

$$|\psi_{\pm 1/2}|^2 = \frac{1}{2}[1 + \cos(\Delta k_0 \pm \Delta \varkappa)l], \qquad (22)$$

where

$$\Delta k_0 = k_{02} - k_{01}, \quad \Delta \varkappa = \varkappa_2 - \varkappa_1.$$

If $l = \pi/\Delta k_0 + \Delta \varkappa$ so that $|\psi_{1/2}|^2 = 0$, then for $\Delta \varkappa / \Delta k_0 \ll 1$

$$|\psi_{-1/2}(l)|^2 = \frac{1}{2}\left[1 - \cos 2\pi \frac{\Delta \varkappa}{\Delta k_0}\right] \simeq \pi^2 \left(\frac{\Delta \varkappa}{\Delta k_0}\right)^2 \qquad (23)$$

or in the notation of Eq. (3a),

$$|\psi_{-1/2}(l)|^2 = \frac{\pi^2}{4} \gamma^2 D^3 \frac{(\varepsilon_{\perp_2} - \varepsilon_{\perp_1})^2}{(\sqrt{\varepsilon - \varepsilon_{\perp_2}} - \sqrt{\varepsilon - \varepsilon_{\perp_1}})^2}. \qquad (24)$$

According to Eq. (23), the quantity $|\psi_{-1/2}|^2$ is quite different from zero (≥ 0.1) for $\Delta \varkappa / \Delta k_0 \sim \varkappa / k_0 \geq 0.1$, which is satisfied for holes in GaAs.

[1])Deceased.

[1] D. W. Wilson, E. N. Glytsis, and T. K. Gaylord, J. Appl. Phys. **73**, 3352 (1993).
[2] R. Kaji and M. Koshiba, IEEE J. Quantum Electron. **30**, 1036 (1994).
[3] Yu. A. Bychkov and É. I. Rashba, JETP Lett. **39**, 78 (1988).
[4] *Optical Orientation* [in Russian], ed. by B. Zacharchenko (Nauka, Leningrad, 1989).
[5] A. S. Tager and I. P. Chepurnykh, Zh. Tekh. Fiz **21**(11), 72 (1995) [Tech. Phys. Lett. **21**, 429 (1995)].
[6] U. Rossler, F. Malcher, and G. Lommer, *Springer Series in Solid State Science*, Vol. 87 (1989), pp. 376–385.

Unipolar semiconductor laser for the terahertz frequency range

A. S. Tager[1)]

State Scientific-Industrial Enterprise "Istok," Fryazino
(Submitted December 9, 1996)

In this paper a new design is proposed for a unipolar semiconductor laser with longitudinal transport of electrons and a stepped variation in the thickness of quantum wells, in which population inversion is obtained, and as a result the electrons of the first subband in the narrow part of the well, with injection into the wide part, preferentially populate its second subband. © *1997 American Institute of Physics.* [S1063-7850(97)03302-8]

In the past three years a considerable amount of discussion has been carried on regarding different variants of unipolar lasers based on intersubband transitions of the electrons in semiconducting heterostructures, which were proposed as long ago as 1971 by R. F. Kazarinov and R. A. Suris,[1] and were fabricated experimentally in 1994 by the group of F. Capasso.[2] Unlike ordinary injection bipolar lasers, which use interband electron transitions, the radiated frequency of the unipolar lasers is not related to the band gap of the semiconductor, and in principle can be varied over a wide range by a proper selection of the heterostructure parameters — the composition and thickness of the layers that make them up, the sequence of these layers, etc. This circumstance opens up the possibility in principle of developing semiconductor lasers operating in parts of the electromagnetic spectrum from the near infrared ($\lambda > 12$–15 μm) to the submillimeter wavelength range, which have been previously inaccessible to them. This possibility is all the more attractive because the frequency range 10^{12}–3×10^{13} Hz, which we nominally call the terahertz range, has not to this day yielded to practical electronics. However, the advance of unipolar lasers into the long-wavelength region encounters serious difficulties related mainly to electron relaxation processes in the crystal, whose negative role increases with decreasing photon energy and increasing period of the electromagnetic oscillations. In particular, with decreasing frequency the Ohmic losses of electromagnetic energy in semiconductor layers that form the electromagnetic waveguide (the cavity) of the laser, increase sharply (as ω^{-2}). The problem is that in conventional designs of semiconductor lasers with electron transport transverse to the active layer, the adjacent semiconductor layers that form the electromagnetic waveguide contain a high concentration of free electrons ($\sim 10^{18}$ cm^{-3}), which provide the necessary current density in the active layer. At frequencies above the inverse electron relaxation time ($\tau^{-1} \approx 10^{-13}$ Hz), the high-frequency Ohmic losses are less than the static losses by a factor of $(\omega\tau)^2$, so that amplification of the electromagnetic oscillations in the active layer (or layers) exceeds their absorption in the passive layers of the waveguide. At frequencies of about 1 terahertz, $\omega\tau \sim 1$, and the absorption in the passive layers dominates.

This communication presents a version of the unipolar laser which in principle avoids this difficulty. The principal idea involves using longitudinal instead of transverse transport, where the electrons that take part in the radiative transitions move not transversely to the structure of the quantum well but along one of the quantum wells (or several, parallel to it). In this version the population inversion of the energy subbands in the quantum well is obtained as a result of an abrupt (stepwise) change in the thickness of the quantum well in a certain cross section. As was shown in Ref. 3, at the juncture of two quantum wells (electron waveguides) of different thickness the electrons are redistributed between the subbands: when the electrons injected into the lower narrow quantum well (the first subband) make a transition into the wider well, they may end up preferentially in the second subband, corresponding to the next discrete value of their transverse energy. For more than a twofold increase in the well thickness, the population inversion of the two first subbands in the wide well can reach $2:1$ (Ref. 3).

A possible variant of the comb structure of the unipolar laser in the terahertz range with longitudinal electron transport is shown schematically in Fig. 1. The quantum well is formed from an epitaxial layer of undoped GaAs with a stepwise change in the thickness and two δ-doped barrier layers of AlGaAs with $x \approx 0.1$. This layer along with the two symmetrically situated AlGaAs boundary layers with a heavier aluminum doping ($y = 0.4$) form an electromagnetic waveguide calculated for a frequency of 4.5 THz. The hot electrons are injected into the narrow part of the quantum well from a narrow stripe source contact containing the AlGaAs/GaAs barrier structure that provides injection of electrons with an energy of 30–35 meV. The electrons move ballistically to the comb drain contact on the other side, with a small accelerating potential difference between the source and the drain. The width w of the comb and the total thickness d of the semiconductor layers making up the electromagnetic waveguide is about 10 μm, which corresponds to one-half wavelength of the electromagnetic radiation (in the crystal) at the frequency 4.5 THz.

The ballistic flight of the electrons over a distance of about 10 μm (at the operating temperature of $T = 77$ K) is possible because of their small energy (30–35 meV) as compared to the energy of longitudinal optical phonons in GaAs (~ 36 meV). For this condition, the electron mean free time in GaAs at $T = 77$ K is longer than 10^{-10} s (Ref. 4), so that the length of ballistic flight of the electrons with a longitudinal energy of 5 meV (a velocity of 1.6×10^7 cm/s) is greater than 16 μm.

As in an ordinary laser with transverse electron transport through quantum wells, in this structure the electrons interact
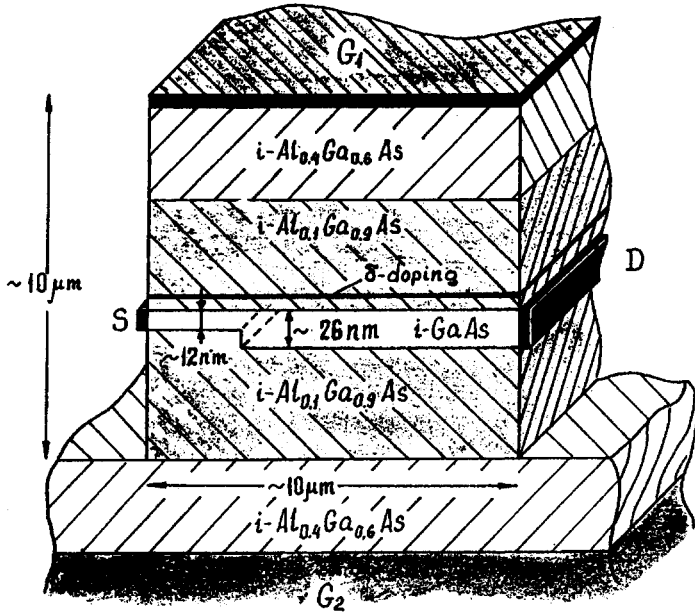
FIG. 1. Diagram of the comb structure of a unipolar laser.

with the transverse component of the electric field of the electromagnetic wave propagating along the comb, and because of the absence of free electrons the absorption of the rf energy in the bulk of the crystal is small, as is the loss due to radiation through the side surfaces of the comb, and is due mainly to the loss of uniformity of these surfaces near the thin source and drain contacts.

In conclusion, the following are the numerical results for the basic parameters of the laser.

1. The frequency $\omega/2\pi = 4.5$ THz corresponds to a photon energy $\hbar\omega \simeq 18$ meV $\gg 6$ meV $= kT$ ($T = 77$ K). If E_{II1} and E_{II2} are the energies of the bottom of the first two subbands in the second, wide part of the quantum well of thickness a_2, then $\hbar\omega = E_{II2} - E_{II1} \approx 3E_{II1}$, $E_{II1} \simeq 6$ meV, and $a_2 \simeq 26.5$ nm. For a stepped change in the thickness of the quantum well equal to $a_2/a_1 = 2.2$, which gives population inversion of the levels E_{II1} and E_{II2} equal to $n_2/n_1 \simeq 1.6$, the thickness of the first (narrow) part of the well is $a_1 \simeq 12$ nm, and the energy of the bottom of the lower subband is $E_{I1} \approx 30$ meV. If the Fermi energy is $E_F = E_{I1} + 5$ meV, then the surface density of electrons in the well is

$$n = \frac{\hbar^2}{2m^*}(E_F - E_{I1}) \simeq 1.8 \times 10^{11} \text{ cm}^{-2} \quad \text{and}$$

$$\Delta n = n_2 - n_1 = 0.23n \approx 4 \times 10^{10} \text{ cm}^{-2}.$$

In the absence of scattering of electrons by optical phonons in GaAs at $T = 77$ K, the electron lifetime τ in the coherent excited state (at the level E_{II2}) is limited by electron collisions, and according to various calculations is about $\tau = 10^{-12}$ s.

2. The specific (per unit length) electron amplification of the laser is

$$g \approx \Gamma \frac{\Delta n}{a_2} \frac{q^2 \tau Z_0 \omega \langle Z \rangle^2}{\varkappa \hbar},$$

where $Z_0 = \sqrt{V_\varepsilon} = 373\Omega$, $\varkappa \simeq 0.34$ is the coefficient of refraction of GaAs, $q^2 \langle Z \rangle$ is the matrix element of the dipole tran-

sition, q is the electron charge, and $\Gamma = 2a^2/d$ is the filling factor of a waveguide of height $d \simeq 10$ μm. In the present case $\langle Z \rangle \simeq 5.1$ nm, $\Gamma = 5.6 \times 10^{-3}$, and $g \simeq 65$ cm^{-1}. For a typical laser length, $L \simeq 0.5$ mm, the net electron amplification is $G = gL \approx 3.25$. If the radiative losses are small, this gain is sufficient for efficient lasing in the crystal with a partially transparent shutter electrodes.

3. The maximum power and width of the emission line of the laser with a single quantum well of width w and length L can be estimated from the formulas[5]

$$P_{max} \approx \frac{1}{2}\Delta n \hbar \omega w L/\tau.$$

For $w \approx L \approx 10$ μm, $\Delta n = 4 \times 10^{10}$ cm^{-2}, and $\tau = 10^{-12}$ s, we have

$$\Delta f = (\Delta n w L \tau)^{-1},$$

$$P_{max} \simeq 2.5 \text{ mW}, \quad \Delta f \simeq 0.6 \text{ MHz}.$$

The radiated power can be increased and the line correspondingly narrowed if not just one quantum well, but several identical parallel quantum wells are created in the crystal. The emission frequency can be varied over certain limits by changing the transverse potential difference between the shutters G_1 and G_2.

[1])Deceased.

[1] R. F. Kazarinov and R. A. Suris, Fiz. Tekh. Poluprovodn. **5**, 800 (1971) [Sov. Phys. Semicond. **5**, 710 (1971)].

[2] J. Faist, F. Capasso, D. L. Sivco et al., Science **264**, 553 (1994).

[3] A. S. Tager and V. P. Chepurnykh, Pis'ma Zh. Tekh. Fiz. **20**(18), 49 (1994) [Tech. Phys. Lett. **20**, 744 (1994)].

[4] J. G. Ruch and W. Fawcett, J. Appl. Phys. **41**, 3843 (1970).

[5] H. C. Casey and M. B. Panise, *Heterostructure Lasers* (Academic Press, New York 1978) [Russ. transl., Mir, Moscow, 1981].

Translated by J. R. Anderson

Convective instability of a rotating fluid above a rapidly heated surface

M. O. Lutset

S. S. Kutateladze Institute of Thermal Physics, Siberian Branch of the Russian Academy of Sciences, Novosibirsk

Convection in a rotating fluid above a rapidly heated surface is studied experimentally. © *1997 American Institute of Physics.* [S1063-7850(97)00102-X]

A particular case of hydrodynamic instability known as convective instability is encountered frequently in natural[1] and industrial[2,3] processes. A layer of fluid above a rapidly heated surface in a gravitational field ceases to be in equilibrium after a certain time has elapsed from the onset of heating, and the ordinary heat conduction is replaced by convective motion. We know of several studies[1,4] (see also the literature cited therein) where the onset of convection is related to the loss of mechanical stability, the effects of random fluctuations[5], or to a second-order phase transition[6] where the convection velocity was taken as the order parameter. Fluids with different Prandtl numbers and slow rates of heating in the Earth's gravitational field have been used in previous investigations. In the present paper we investigate the convective instability of a liquid nitrogen layer undergoing rigid-body rotation above a finite extremely rapidly heated surface. One parameter, the angular rotation velocity ω, was varied, which as will be shown subsequently, is equivalent to varying only the acceleration due to gravity g with an almost constant ratio of Coriolis force to viscous force (the Taylor number D).

The experiments were carried out using a rotating cryostat[7] with a working cylinder diameter of 0.2 m. The heat-transfer surface was the largest plane of a $50 \times 4.76 \times 3.2$ mm glass plate on which was deposited a 1000 Å conducting film whose resistivity was independent of temperature. Paper 15 μm thick was stuck to the film with BF-2 adhesive and five miniature silicon temperature sensors consisting of $0.3 \times 0.3 \times 0.5$ mm uncased KT324B transistors were stuck to this paper at various distances along the longitudinal axis of the surface. The thickness of the silicon wafer adhered to the heat-transfer surface was 0.1 mm and the total thickness of the film coating was 30 μm. The glass plate was placed on the cylindrical surface of the cryostat working volume along the generatrix, with the heat transfer surface facing the axis of rotation. The liquid nitrogen layer above the plate had a constant thickness of 13.4 mm.

At zero time, a direct current was switched instantaneously across the conducting film. Since the $p-n$ junction was sensitive to changes in temperature, the sensors changed resistance in proportion to the change in the average temperature in the 0.015 mm^3 volume. The delay of the sensors did not exceed 50 μs. The resistance of the $p-n$ junction was measured by the four-probe method and the change in resistance was recorded by a storage oscilloscope. The oscilloscope traces for a fixed current through the film and different ω were superposed. The combined pattern did not depend on the direction of rotation or the sensor number. A typical example is shown in Fig. 1. Up to the time t_c, which depends on ω, the traces were the same and followed the change in the temperature of the heat-transfer surface predicted by solving the heat conduction equation for the infinite composite body (glass, film, coating, nitrogen). After $t_c(\omega)$, the temperature of the heat transfer surface ceases to follow the heat conduction equation, which suggests that the equilibrium of the fluid layer is disrupted. An accurate solution of the heat conduction equation with suitable initial and boundary conditions for this particular problem was obtained by means of a Laplace transformation. For time intervals much greater than the delay $\delta^2/4\varkappa_1$ caused by the coating on the conducting film, disregarding time-decaying terms in the accurate solution, we obtain the asymptotic variation of the fluid temperature

$$T(x,t) = \frac{4a_1 Q}{\pi^{1/2}(a_1+a_2)(a_1+a_3)}$$
$$\times \left\{ t^{1/2} - \frac{\pi^{1/2}}{2}[\delta/\varkappa_1^{1/2} + x/\varkappa_2^{1/2}] \right\} \tag{1}$$

and the heat flux to the fluid at the coating–nitrogen interface

$$q(0,t) = Q\frac{2a_1 a_2}{(a_1+a_2)(a_1+a_3)}. \tag{2}$$

Here x is the coordinate normal to the heat-transfer surface, directed into the fluid, $a_i = (\lambda_i \rho_i C_{pi})^{1/2}$, $i=1,2,3$ is the label of the medium, where 1 is the coating, 2 is nitrogen, and 3 is the glass, λ_i, C_{pi}, and $\varkappa_i$ are the thermal conductivity, the specific heat, and the thermal diffusivity, respectively, ρ_i is the density, δ is the coating thickness, and Q is the heat flux released at the film, which was 6.9 W/cm^2 in our experiments. For $Q > 6.9$ W/cm^2 and small ω, boiling of the fluid was observed.

According to the linear theory,[8] the stability of the equilibrium of a rotating cylindrical layer of fluid is determined by two dimensionless parameters: the Rayleigh number Ra $= g\beta\Delta T h^3/\nu\varkappa_2$ and the Taylor number $D = \omega h^2/\nu$, where β and ν are the coefficient of volume expansion and the kinematic viscosity of nitrogen, respectively, ΔT and h are the temperature drop and a linear dimension characterizing the temperature gradient in the fluid. Equilibrium is disrupted when the Rayleigh number reaches the critical value Ra$_c(D_c)$. Since condition (1) is satisfied when mechanical equilibrium is conserved in the fluid, following Refs. 1, 4, and 5, we must assume $\Delta T = T(0,t)$ and $T(n,t) = 0$. This
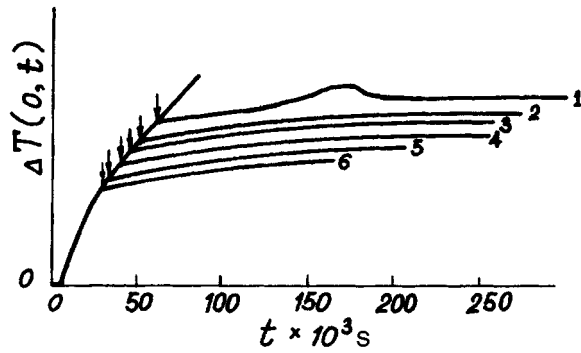
FIG. 1. Oscilloscope traces of sensor resistance for $Q = 6.9$ W/cm^2 for various η: 1 — 196, 2 — 345, 3 — 555, 4 — 818, 5 — 1535, and 6 — 1958. The arrows indicate t_c.

FIG. 2. Critical Rayleigh number Ra$_c$ versus D_c: 1 — calculated according to linear stability theory,[11] 2 — quasisteady-state measurements,[11] and 3 — our measurements. The inset shows our measurements on an enlarged scale.

gives $h = 2(\varkappa_2 t / \pi)^{1/2} - \delta(\varkappa_2 / \varkappa_1)^{1/2}$. The values of $\Delta T(t_c)$ and $h(t_c)$ determine Ra$_c$ and D_c. Results of calculations using the measured values of $t_c(\omega)$ are presented in Table I, where $\eta = g/g_0$ and g_0 is the acceleration due to the Earth's gravitational field. According to Refs. 9 and 10, we have $a_1 = 146$, $a_2 = 470$, $a_3 = 460$ J/m$^2 \cdot$ Ks$^{1/2}$, $\varkappa_1 = 1.97 \times 10^{-7}$ m^2/s, and $\varkappa_2 = 8 \times 10^{-8}$ m^2/s. The error in the measurements and the calculations did not exceed 15%. As the gravitational force increases monotonically, we observe a decrease in t_c, ΔT_c, and h_c, and a nonmonotonic variation of Ra$_c$ and D_c within 20%. Nevertheless, the behavior of Ra$_c(D_c)$ agrees within measurement error (Fig. 2) with that predicted by linear stability theory[11] for a rotating Rayleigh–Bénard cell. Strictly speaking, our problem and the Rayleigh–Bénard problem differ qualitatively because of the time dependence of the linear scale in our case. Thus the experimental results must be substantiated theoretically, and this is the subject of further research.

In our experiment the onset of convection is taken as the point where the change in the temperature of the heat-transfer surface deviates from the solution of the heat conduction equation. The Nusselt number constructed at time

t_c is obviously Nu$_c = qh_c/\lambda_2\Delta T_c = 1$, and Ra$_c \sim 10^3$, although these numbers are related by Nu$_c = C_T(\text{Ra}_c)^{1/3}$, where the coefficient C_T calculated from the tabular values of Ra$_c$ varies in the range 0.078–0.086 and is close to the value of 0.085 observed when Ra $> 10^5$ for advanced turbulent convection.[12] This external similarity may have a physical basis due to the development of convective motion in a layer with a time-varying linear scale.

[1] J. C. Mollendorf, H. Arif, and E. B. Ajiniran, Int. J. Heat Mass Transfer **27**, 273 (1984).

[2] M. O. Lutset and Yu. M. L'vovskiĭ, Dok. Akad. Nauk SSSR **256**, 583 (1981) [Sov. Phys. Dokl. **26**, 78 (1981)].

[3] A. N. Pavlenko and V. Yu. Chehovich, Fiz. Nizk. Temp. **16**, 510 (1990) [Sov. J. Low Temp. Phys. **16**, 291 (1990)].

[4] T. Y. Chu, in *Heat Transfer 1990*, Vol. 1 (Hemisphere, 1990), pp. 169–174.

[5] K. M. Kim and M. U. Kim, Int. J. Heat Mass Transfer **29**, 193 (1986).

[6] D. C. Rapaport, Phys. Rev. A **46**, R6150 (1992).

[7] M. O. Lutset and V. E. Zhukov, Cryogenics **29**, 37 (1989).

[8] G. F. Shaĭdurov, M. I. Shliomis, and G. V. Yastrebov, Izv. Akad. Nauk SSSR Ser. Mekh. Zhid. Gaz. No. 6, 88 (1969).

[9] I. G. Kozhevnikov and L. A. Novitskiĭ, *Handbook of Thermophysical Properties of Materials at Low Temperatures* [in Russian], Mashinostroenie, Moscow (1982).

[10] M. P. Malkov *et al.*, *Handbook of Physicotechnical Principles of Cryogenics* [in Russian], Énergiya. Moscow (1973).

[11] P. G. J. Lucas, J. M. Pfotenhauer, and R. J. Donnelly, J. Fluid. Mech. **129**, 251 (1983).

[12] S. S. Kutateladze, *Principles of Heat Exchange Theory* [in Russian], Atomizdat, Moscow (1979).

Translated by R. M. Durham

TABLE I.

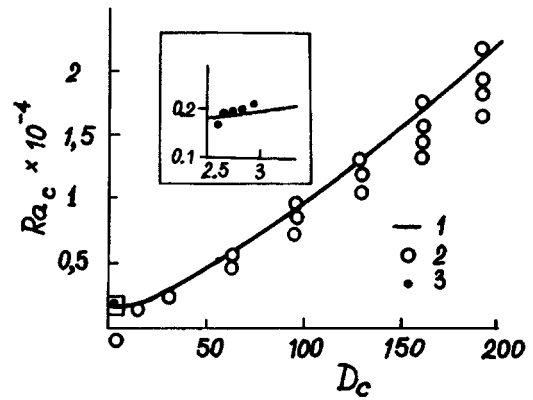| η	196	345	555	818	1221	1958
t_c, 10^{-3} s	60.6	50	40.9	37.9	33.3	27.3
ΔT_c, K	11.3	9.96	8.66	8.2	7.46	6.4
h_c, 10^{-6} m	59.4	52.2	45.4	43	39.1	33.6
Ra$_c$	1788	1883	1732	2054	2097	1831
D_c	2.71	2.78	2.66	2.90	2.93	2.74

Dynamics of field dislocations and disclinations in a few-mode waveguide: II. Pure types of singularities

A. V. Volyar and T. A. Fadeeva

Simferopol State University

Some aspects of recording dislocations and disclinations of the field of the linearly polarized LP_{11} mode at the exit from an optical fiber have been investigated experimentally and theoretically. It has been found that the type of field dislocation and its topological charge depend strongly on the fiber length, the polarization state of the reference beam, and the orientation of the polarizer axis at the interferometer exit. It has also been shown experimentally that when the reference beam is circularly polarized (without a polarizer), C^+ and C^- pure edge disclinations of the LP_{11} mode are recorded. In a polarization interference system where the fiber length is a quarter of the beat length of the LP_{11} mode, a pure screw dislocation with the topological charge $l=1$ and $l=-1$ is observed when the orientation of the polarizer transmission axis is $\alpha=\pi/4$ and $\alpha=3/4\pi$, respectively, if the reference beam is linearly polarized at the angle $\pi/4$ to the x axis. When the reference beam is circularly polarized, the angle of orientation of the pure edge dislocation follows the polarizer axis and reversal of the reference-beam polarization changes the sign of the angle of inclination of the edge dislocation.

When studying the field of a few-mode waveguide, some caution must be exercised in the description of wavefront singularities. Estimates of the average number of field dislocations[1] or the transformation of their topological charges[2] must depend on the method of observing the optical field. It was shown in Ref. 3 that when free-space Gaussian beams carrying a topological charge undergo spatial interference, the type of singularity observed depends on the curvature of the beam wavefronts and their directions of convergence. The vector properties of the wave fields must be taken into account when field singularities are observed in an inhomogeneous medium.

In the first part of this study, we noted that the main physical mechanism responsible for evolution of the field in the linearly polarized LP_{11} mode of an inhomogeneous medium is the interaction between circularly polarized C^+ and C^- disclinations, which form mixed types of singularities (superposed singularities of various components of the vector field). The polarization state of the reference beam must be taken into account when these mixed phase singularities, assigned to different polarizations, are recorded experimentally. The recording process also depends on whether the measuring system incorporates a polarization analyzer.

The aim of this paper is to study some features of the experimental manifestation of pure types of vector singularities (dislocations and disclinations) in the LP_{11} mode of the radiation field of a few-mode waveguide in the polarization interference of light. Particular attention is paid to the type of dislocation observed and its topological charge.

1. Let us examine an optical fiber excited such that only the LP_{11} mode combination is produced.

Let us assume that the radiation field is summed coherently with a smooth field having the polarization state $(a_{01}\hat{x}+a_{02}\hat{y})$. The superposition of these fields may be expressed as

$$e=a_1\begin{pmatrix}\cos\ \delta\beta_1z_0\ \cos\ \varphi\\ i\ \sin\ \delta\beta_1z_0\ \sin\ \varphi\end{pmatrix}\exp\{i\Phi_1\}F_1(R)\begin{pmatrix}a_{01}\\ a_{02}\end{pmatrix}$$
$$\times\exp\{i\Phi_2\}F_0(R), \tag{1}$$

where a_1 is the amplitude of the LP_{11} mode, $\delta\beta_1$ is the difference in the propagation constants of the TE_{01} and HE_{21} modes,

$$\Phi_1=\beta z_0+kz, \quad \Phi_2=\psi_0+kz\ \cos(\theta)+kr\ \sin(\theta), \tag{2}$$

β is the propagation constant of the LP_{11} mode in an inhomogeneous medium, r is the radial coordinate of the beam, θ is the angle of convergence of the beams, and $F_{1,0}(R)$ is the radial distribution function of the beam field.[4]

Let us assume that there is no polarizer in the optical system. Then the result of measuring the radiation field will depend only on the polarization state of the reference beam and the length of the optical fiber, z_0. If the reference beam is linearly polarized along the $\hat{x}$ or $\hat{y}$ axis and a_{01} or a_{02} are zero, a pure edge dislocation is observed for any fiber length z_0 (Fig. 1a). If the reference beam is linearly polarized at the angle $\pi/4$ ($a_{01}=1$, $a_{02}=1$), a mixed screw-edge dislocation (Fig. 1b) will be recorded experimentally for fiber lengths which are not multiples of a quarter of the beat length, $\Lambda/4$, of the LP_{11} mode ($\Lambda=2\pi/\delta\beta_1$). For fiber lengths $z_0=\Lambda/4(4m+1)$ a pure screw dislocation is observed with the topological charge $l=+1$, whereas for $z_0=\Lambda/4(4m+3)$, we also observe a screw dislocation, but with the topological charge $l=-1$. Reversal of the sign of the topological charge for fiber lengths which are multiples of $z_0=\Lambda/4(4m+1)$ or $z_0=\Lambda/4(4m+3)$ may be observed when the azimuth of the linear polarization of the reference beam is altered by 90° ($a_{01}=1$, $a_{02}=-1$) (Figs. 1c and 1d). For an arbitrary polarization state and arbitrary length z_0 a mixed screw-edge dislocation is observed.

The case of a circularly polarized reference beam is of particular interest. For right circulation ($a_{01}=1$, $a_{02}=i$) the reference beam selectively interferes with the right circulation of the field while the left circulation forms the background. In Fig. 1e we observe a pure edge dislocation with
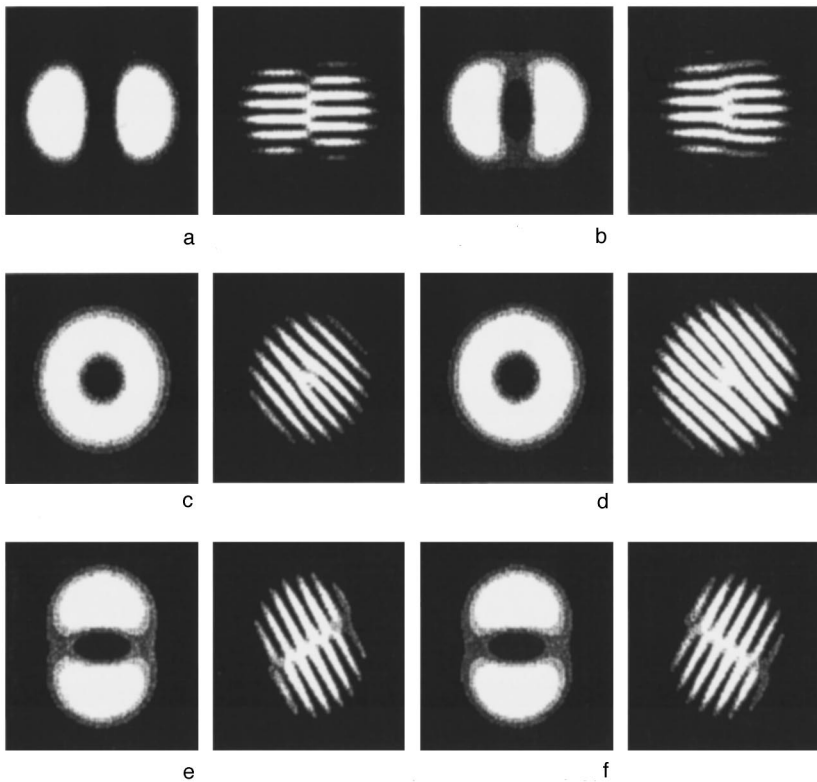
FIG. 1. Field distribution and interference patterns for polarization interference of the LP_{11} mode (computer calculations).

the angle of inclination $\psi = \delta\beta_1 z_0$ exactly matching that of the C^- disclination. Reversal of the circulation of the beam polarization ($a_{01} = 1$, $a_{02} = -i$) changes the sign of the angle ψ of the pure edge dislocation ($\psi = -\delta\beta_1 z_0$) (Fig. 1f). This change in the angle means that the reference beam now selects the C^+ disclination for interference, having its axis inclined at the angle $\varphi = -\delta\beta_1 z_0$.

Let us assume that the optical system incorporates a linear polarizer having its axis oriented at the angle α. The observation results will then depend on the length z_0 and the polarization state of the beam, and on the angle α, so that in a coordinate system with one axis directed along the polarizer axis, the field is expressed in the form

$$e_\alpha = e_x \cos \alpha + e_y \sin \alpha. \qquad (3)$$

When $\alpha = 0$ or $\pi/2$, pure edge dislocations are observed for any fiber length z_0. A mixed screw-edge dislocation is recorded for an arbitrary angle α and arbitrary beam polarization state. For $\alpha = \pi/4$ or $\alpha = 3/4\pi$, and $z_0 = \Lambda/4(4m+1)$ a pure screw dislocation is observed with topological charge $l = +1$ and $l = -1$, respectively.

An interesting effect is observed after a circularly polarized reference beam has propagated through the polarizer. For right circulation ($a_{01} = 1$, $a_{02} = i$) the axis of the edge dislocation always follows the rotation of the polarizer angle α. Reversal of the circulation ($a_{01} = 1$, $a_{02} = -i$) alters the angle of inclination of the dislocation axis relative to the polarizer axis ($\psi = -\alpha$).

The physical mechanism responsible for these effects is related to the nonuniform polarization of the optical fiber fields. A uniformly polarized reference beam only interacts selectively with that component of the mode combination
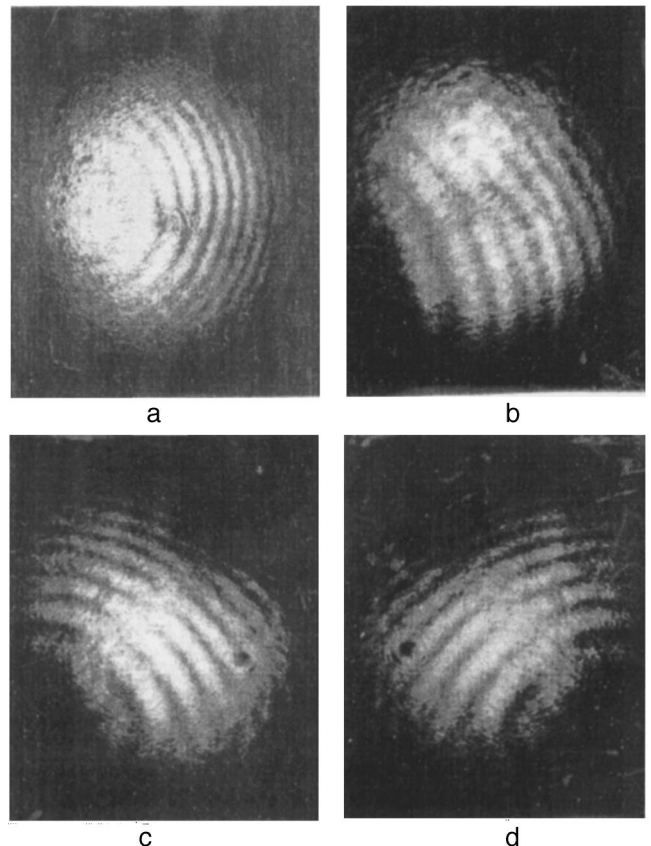

FIG. 2. Photographs showing interference of the LP_{11} mode and a Gaussian reference beam.

A. V. Volyar and T. A. Fadeeva   92

whose polarization is matched with it. Similarly the polarizer selects waves of the same polarization in the reference and object beams.

2. For an experimental investigation we selected a few-mode fiber with the core diameter $\rho_0 = 3.5$ μm and the waveguide parameter $V = 3.6$ for the wavelength $\lambda = 0.63$ μm. The beat length was $\Lambda = 3.6$ m. The fiber was inserted in a Mach–Zehnder interferometer (see Part I of this article). The polarization state of the reference beam was recorded by rotating the polarizer and a quarter-wave plate inserted in the reference beam. The fiber was successively broken off every 1 cm. The polarization interference patterns, angles of orientation of the dislocation axes, and their topological charges were recorded for various beam polarization states Q and angles of orientation of the polarizer axis, α. The accuracy of recording the circular polarization was $Q = 0.95 \pm 0.05$. Figure 2 shows typical interference patterns of the fiber radiation field and a Gaussian reference beam (TEM$_{00}$ laser mode). We specially selected pure screw dislocations which reverse the sign of the topological charge when the angle $\alpha = \pi/4$ is changed to $3/4\pi$ (Figs. 2a and 2b). Note that as well as selecting the fiber length z_0, we also needed to provide additional mode matching by altering the radius of curvature of the fiber loop mounted at the entry section of the fiber in order to achieve a pure screw dislocation.

It was established by means of a control experiment that when the field of the linearly polarized LP$_{11}$ mode interferes with that of a circularly polarized Gaussian beam, reversal of the circulation of the reference beam polarization (Figs. 2c and 2d) simultaneously alters the angle of orientation $\psi = \delta\beta_1 z_0$ of the edge dislocation of the interference pattern to $\psi = -\delta\beta_1 z_0$ in good agreement with the theoretical calculations. These results provide experimental confirmation that C^+ dislocations of the LP$_{11}$ mode field do exist.

[1] S. S. Abdulaev and G. M. Zaslavskiĭ, Kvantovaya Elektron. (Moscow) **14**, 1475 (1987) [Sov. J. Quantum. Electron. **17**, 937 (1987)].

[2] M. A. Bolshtyanskiĭ, Opt. Spektrosk. **79**, 512 (1995) [Opt. Spectrosc. J. 475 (1995)].

[3] I. V. Basistiy, M. S. Soskin, and M. V. Vasnetsov, Opt. Commun. **119**, 604 (1995).

[4] A. W. Snyder and J. D. Love, *Optical Waveguide Theory* (Methuen, London, 1984) [Russ. transl. Radio i Svyaz, Moscow, 1987].

Translated by R. M. Durham

Nonisothermal conditions for limitation of the current injected into a composite superconductor exposed to pulsed perturbations

V. R. Romanovskiĭ

"Kurchatov Institute" Russian Science Center

This study is devoted to solving one of the major problems of superconductivity engineering — the thermal stability of the superconducting state of a composite superconductor. The formulated problem is analyzed most comprehensively with allowance for the nonisothermal dynamics of the magnetic flux inside the composite. This approach allowed us to formulate the main aspects of the behavior under the simultaneous influence of various perturbing factors, i.e., varying current and external thermal perturbation. © *1997 American Institute of Physics.*
[S1063-7850(97)00302-9]

Destruction of the superconducting state of composite superconductors, formed by numerous superconducting wires in a normally conducting metal matrix, is caused by various instabilities.[1–4] The conditions for maintaining of superconductivity are generally analyzed using models which assume that the composite is exposed to one particular type of perturbation. In the theory of thermomagnetic instability, for instance, the perturbing factor is the varying external magnetic field or the current injected into the composite. In the theory of thermal stabilization, the stability of the superconducting state is considered in relation to pulsed thermal perturbations of varying length, duration, and shape under conditions where the transport current is either constant or varies negligibly. By solving these problems, it is possible to identify typical physical characteristics responsible for maintaining or destroying the superconducting properties of the composite subject to specific simplifying assumptions. In real windings however, the variations of the temperature of the current-carrying element and the current flowing through it in response to any external perturbation are interrelated. It is thus extremely interesting to consider the stability problem from this viewpoint.

It was shown in Refs. 5 and 6 that determining the boundaries of stable superconducting states by solving a complete system of Fourier and Maxwell equations eliminates inaccuracies in assessing the role of the tolerable increase in the superconductor temperature when analyzing the conditions for the onset of instability. In particular, it was established that there is a direct correlation between the depth of current penetration preceding cutoff and the tolerable overheating temperature. The overheating may indeed be very appreciable with poor cooling and a rapidly rising external magnetic field or current. Consequently the conditions for the onset of instability at a composite in an adiabatic condition depend strongly on the thermal prehistory of the sample.

The relative influence of thermal and electromagnetic processes taking place in composite superconductors also affects the conditions for the onset and propagation of thermal instabilities. The authors of Refs. 7 and 8 put forward an explanation for the experimentally observed anomalies in the propagation of the normal zone along the composite at high rates of current variation. An analysis of the critical energies needed to convert the superconducting composite to the normal state, carried out within the proposed model demonstrated their dependence on the current injection rate. It was assumed that the thermal instability only propagates in the longitudinal direction of the composite and the space–time behavior of the initial perturbation corresponds to the instantaneous release of heat in a local ("point") region. The results therefore disregard the thermal processes taking place over the transverse cross section of the composite. It was shown in Refs. 9 and 10 that these processes play a decisive role in the stability of the superconducting state of massive current-carrying elements exposed to extended thermal perturbations.

In the present paper we therefore examine the stability of the superconducting states attained without the spontaneous development of instability when current is induced in a composite superconductor at a constant rate and the composite is exposed to an extended pulsed thermal perturbation. As in Ref. 5, the problem was solved by a numerical analysis of a system of equations describing the interrelated dynamics of the thermal and electromagnetic fields on the transverse cross section of a superconducting composite.

We shall determine the distribution of the temperature T, the electric field E, and the current density J in a circular cross-section composite of radius r_0, when the current therein rises at a given rate dI/dt and there is an external source of thermal perturbation, by solving a problem of the type

$$c\frac{\partial T}{\partial t} = \frac{1}{r}\frac{\partial}{\partial r}\left(\lambda r \frac{\partial T}{\partial r}\right) + EJ + q(r,t),$$

$$\mu_0 \frac{\partial J}{\partial t} = \frac{1}{r}\frac{\partial}{\partial r}\left(r\frac{\partial E}{\partial r}\right),$$

$$J = \eta J_s + (1-\eta)J_m, \quad E = J_s \rho_s \exp\left(\frac{J_s}{J_\delta} + \frac{T-T_c}{T_\delta}\right) = J_m \rho_m,$$

$$T(r,0) = T_0, \quad E(r,0) = 0,$$

$$\lambda \frac{\partial T}{\partial r} + h(T-T_0)|_{r=r_0} = 0, \quad \frac{\partial E}{\partial r}\Big|_{r=r_0} = \frac{\mu_0}{2\pi r_0}\frac{dI}{dt}. \tag{1}$$
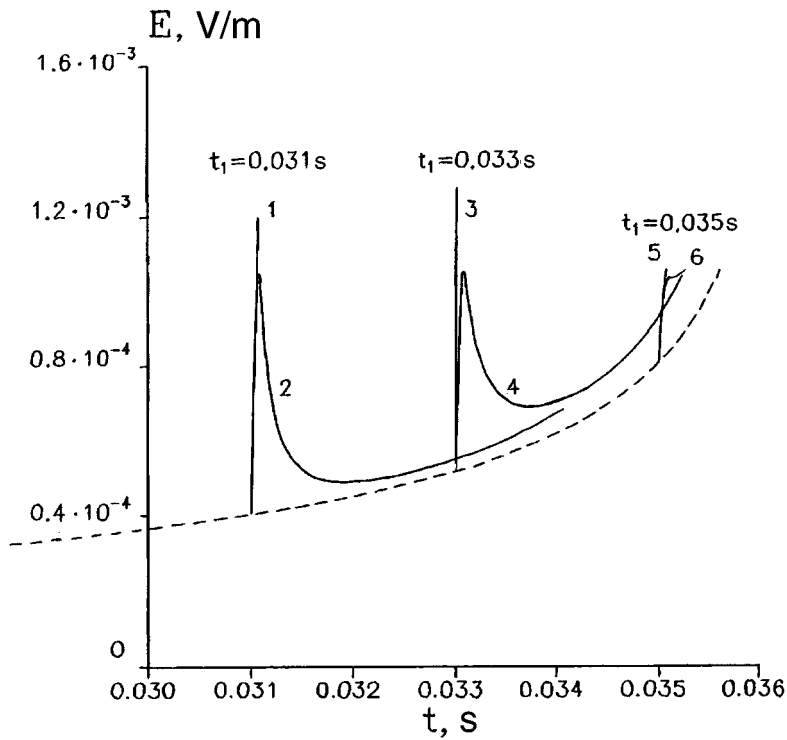
FIG. 1. Variation of the electric field strength at the surface of a composite exposed to perturbations of near-critical energy: 1 — $q_0=3.9\times10^7$ W/m^3, 2 — $q_0=3.8\times10^7$ W/m^2, 3 — $q_0=2.8\times10^7$ W/m^3, 4 — $q_0=2.7\times10^7$ W/m^3, 5 — $q_0=0.9\times10^7$ W/m^3, and 6 — $q_0=0.8\times10^7$ W/m^3.

Here c and λ are the volume specific heat and the thermal conductivity of the composite in the transverse cross section, ρ_s and ρ_m are the resistivities of the superconductor and the matrix, respectively, J_s and J_m are the currents flowing through the superconductor and the matrix, respectively, η is the fill factor of the composite by the superconductor, h is the heat transfer coefficient, T_0 is the coolant temperature, T_c is the critical temperature of the superconductor, J_δ and T_δ are the given growth parameters of the superconductor current–voltage characteristic, and q is the given power of the external heat source.

Within the limits of the model of a continuous medium, this problem describes the nonisothermal diffusion of the current inside a composite superconductor approximated in the simplest case by an infinitely long cylinder. The upper limit of the tolerable currents (cutoff currents) as a function of the external heat source power will be determined for the most dangerous pulsed short-lived perturbations, which can induce instability with the minimum amount of heat release.[3] In this case, the type of heat source scarcely influences the boundary of the stable states. Thus without loss of generality, we can assume that a rectangular heat pulse is released in a thin surface layer of composite $\Delta r=r_0-r_q$, i.e.,

$$q(r,t)=\begin{cases} q_0=\text{const}, & r_q\leqslant r\leqslant r_0, \quad t_1\leqslant t\leqslant t_1+\Delta t, \\ 0, & t>t_1+\Delta t. \end{cases}$$

This system was solved by a finite-difference method. The unknown values of the cutoff current and the heat release power are obtained by an iterative procedure similar to that described in Ref. 5. As a result, two values are obtained numerically for the heat source power for which the electric field strength either decays or increases irreversibly after the perturbation has ceased. Accordingly, the rise in the compos-

ite temperature is short-lived in the first case but in the second, may cause a transition to the normal state. By way of illustration, Fig. 1 shows curves describing the time behavior of the electric field strength at the surface of a composite exposed to near-critical perturbations. The calculations were made for

$$r_0=5\times10^{-4}\text{ m}, \quad c=1000\text{ J/m}^3\cdot\text{K},$$

$$\lambda=100\text{ W/m}\cdot\text{K}, \quad h=10\text{ W/m}^2\cdot\text{K},$$

$$\eta=0.5, \quad r_q=0.9r_0, \quad \Delta t=10^{-5}\text{ s}, \quad dI/dt=10^4\text{ A/s},$$

$$\rho_s=5\times10^{-7}\ \Omega\cdot\text{m}, \quad \rho_m=2\times10^{-10}\ \Omega\cdot\text{m},$$

$$J_\delta=4\times10^7\text{ A/m}^2,$$

$$T_\delta=0.048\text{ K}, \quad T_{\sup}=9\text{ K}, \quad T_0=4.2\text{ K}$$

for various perturbation initiation times t_1. The dashed curve gives the increase in the electric field strength observed when the current is injected without any external thermal perturbations.

Figure 2 gives results of calculations of the cutoff current as a function of the thermal pulse power for two different injection rates. The solid curves give the cutoff currents obtained by solving problem (1). The dashed lines describe the boundary of the stable states, determined with the assumption that no heat is released in the composite through Joule dissipation of energy for all times $t>t_1$ (i.e., the term EJ was omitted in the heat conduction equation). It is easily seen from a comparison of these calculations that under the action of a short pulsed perturbation, the intrinsic heat release plays little part in changing the thermal state of the composite. The onset of instability is therefore caused by an increase in the composite temperature originating mainly
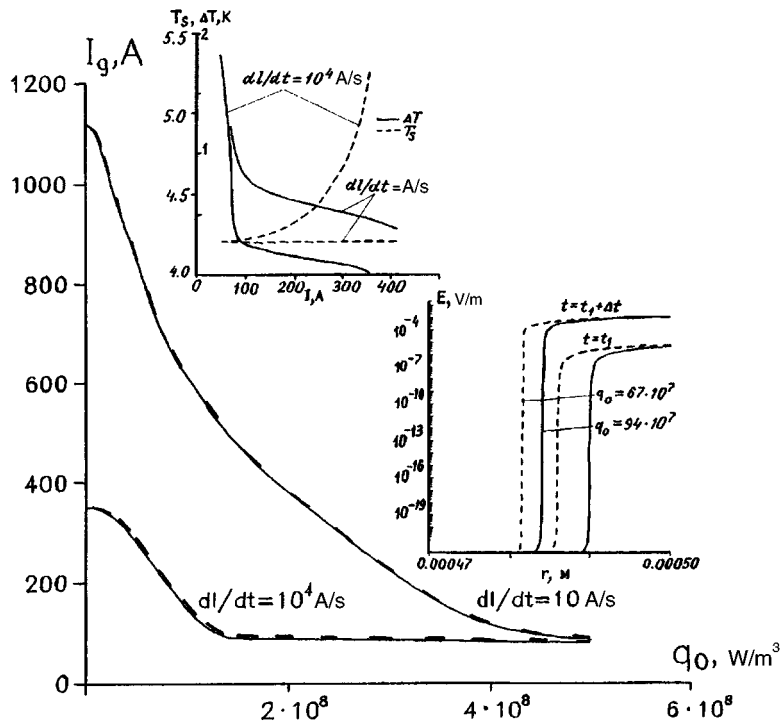
FIG. 2. Cutoff current versus perturbation power. (For commentary to insets see text).

from the external thermal perturbation. Its increase causes an increase in the strength of the electric field, which becomes continuous on exposure to a supercritical perturbation (Fig. 1).

The plotted curves $I_q(q_0)$ also reveal two characteristic regions. First there are regions with maximum cutoff currents whose range of existence depends primarily on the current injection rate and increases with increasing dI/dt. Thus the cutoff current falls off more rapidly when the current is injected slowly rather than rapidly. These relationships will obviously be observed when the coefficient of heat transfer, the superconductor properties, and the nature of the perturbation vary. The values of I_q are highest for $q_0 \to 0$ since in this case exceeding the cutoff current is accompanied by the spontaneous development of instability even when current injection has ceased and there are no external perturbations.[5] The second characteristic region of variation of $I_q(q_0)$ is the region of minimum current-carrying capacity of the composite. The extent of this region depends to a considerable degree on the current injection rate. Under the action of powerful perturbations however, the cutoff currents for different injection rates become similar and decrease very slightly with increasing q_0 over a wide range.

These relations assume that the tolerable overheating of the composite $\Delta T = T(r, t_1 + \Delta t) - T_s$ preceding the onset of instability depends on the injected current. This dependence is plotted in the left inset to Fig. 2 for $r = r_0$, which also gives the composite temperatures T_s against whose background thermal instability develops. It can be seen that as the current increases, the background temperature of the composite rises and the tolerable overheating decreases, approaching zero near the maximum cutoff current. In this case ΔT has very high values at low currents. At the same time, under these current conditions ΔT decays more rapidly with

increasing current than at higher currents. This may be attributed to two mechanisms having different influences on the electric field induced inside the composite by the external heat source. The field increases with temperature but the critical current density of the superconductor decreases, which helps to reduce the electric field. At relatively high cutoff currents the main contribution to the onset of instability is made by the first mechanism, since the relative change in the critical current density is small in this case. With decreasing current, the second factor becomes more important, since the tolerable overheating is increased. As a result, for two similar values of the injected current, a substantial increase in the external perturbation energy is required to achieve similar electric field distributions. By way of illustration, the right inset to Fig. 2 shows the electric field distribution inside the composite for $dL/dt = 10^4$ A/s, exposed to perturbations of near-critical energy. The solid curves correspond to the initial current $I = 50$ A ($t_1 = 0.005$ s) and the dashed curves correspond to $I = 70$ A ($t_1 = 0.007$ s).

This investigation has therefore shown that thermal perturbations strongly influence the stability of current injection into a composite superconductor. Its cutoff, caused by an extended short-lived thermal perturbation, is a direct consequence of a rise in the composite temperature in response to the external heat pulse. In this case, the intrinsic heat release negligibly influences the temperature field of the composite and thus the conditions for the onset of instability. Consequently, when the heat release in the superconducting winding exceeds a certain threshold, the onset of instability depends negligibly on the type of current variation and is accompanied by a considerable decrease in the injected current.

[1] W. J. Carr, *AC Loss and Macroscopic Theory of Superconductors* (Gordon and Breach, New York, 1983).

[2] V. A. Al'tov, V. B. Zenkevich, M. G. Kremlev, and V. V. Sychev, *The Stability of Superconducting Magnet Systems* [in Russian], Énergoatomizdat, Moscow (1984).

[3] M. N. Wilson, *Superconducting Magnets* (Oxford University Press, London, 1983) [Russ. transl. Mir, Moscow, 1985].

[4] A. V. Gurevich, R. G. Mints, and A. L. Rakhmanov, *The Physics of Composite Superconductors* [in Russian], Nauka, Moscow (1987).

[5] V. E. Keĭlin and V. R. Romanovskiĭ, Zh. Tekh. Fiz. **63**(1), 10 (1993) Tech. Phys. **37**, 752 (1992)].

[6] V. R. Romanovskiĭ, Dokl. Akad. Nauk SSSR **336**, 341 (1994) [Phys. Dokl. **39**, 363 (1994)].

[7] A. A. Pukhov and A. L. Rakhmanov, Sverkhprovodn. (KIAE) **6**, 1165 (1993).

[8] A. A. Pukhov, A. L. Rakhmanov, V. S. Vysotsky, and V. N. Tsikhon, IEEE Trans. Appl. Supercond. **5**, 560 (1995).

[9] V. R. Romanovskiĭ, Zh. Tekh. Fiz. **60**(4), 31 (1990) [Sov. Phys. Tech. Phys. **35**, 419 (1990)].

[10] V. R. Romanovskiĭ, Izv. Akad. Nauk. Ross. Akad. Nauk. Ser. Énergetika No. 2, 129 (1992).

Translated by R. M. Durham

Monte Carlo simulation of the electron drift velocity in a one-dimensional GaAs quantum wire

V. M. Borzdov, O. G. Zhevnyak, S. G. Mulyarchik, and A. V. Khomich

Belarus State University, Minsk

Electron transport in a one-dimensional GaAs quantum wire is modeled in the electrical quantum limit with allowance for scattering of charge carriers by polar optical phonons, impurity ions, and surface inhomogeneities. © *1997 American Institute of Physics.*
[S1063-7850(97)00402-3]

Studies of the electronic properties of one-dimensional semiconducting quantum wires are currently attracting major interest. This is mainly because of the potential for using the unique properties of these structures directly in instruments. It is therefore highly topical to investigate electron transport in one-dimensional GaAs quantum wires in moderate and strong electric fields typical of the real operating conditions of semiconducting devices in micro- and nanoelectronics.

It is known that the Monte Carlo method (see Refs. 1 and 3, for instance) is one of the most promising methods of solving this problem fairly efficiently in bulk and quasi-two-dimensional semiconductor systems. However, it should be noted that this method has only been used to calculate the kinetic transport parameters in quasi-one-dimensional quantum wires in a very limited number of studies,[4–6] and as far as we are aware, the electron drift velocity v_{dr} in a quantum structure, where the electrical quantum limit applies, has only been calculated in Ref. 7, but this model only allowed for one mechanism for scattering of charge carriers, by polar optical phonons.

In this paper we present results of a Monte Carlo simulation of electron transport in the quantum well of a one-dimensional GaAs quantum wire having a square cross section. The electron drift velocity was calculated as a function of the electric field strength ε and the side length L of the cross section. The model took into account mechanisms for scattering by polar optical phonons with emission and absorption, scattering by impurity ions, and scattering by surface inhomogeneities. It was assumed that only the lowest size-quantization level was filled and nonparabolicity could be neglected. We used a single-particle Monte Carlo algorithm similar to that described in Ref. 7.

The total electron energy E in a quantum wire of square cross section with side length L in the approximation of an infinitely deep rectangular potential well may be expressed as[7,8]

$$E = \frac{\hbar^2 k_x^2}{2m^*} + \frac{\hbar^2 \pi^2}{m^* L}, \tag{1}$$

where m^* is the electron effective mass and $\hbar$ is the reduced Planck's constant. The first term on the right-hand side of Eq. (1) is the kinetic energy of an electron with the wave vector k_x in the direction of motion x and the second term is the energy of the bottom of the ''zeroth'' subband.

The intensities of scattering by polar optical phonons with emission and absorption were calculated according to the following formulas, respectively[8]

$$W_{ph}^{em}(k_x) = \frac{\alpha}{2} \frac{\omega}{\pi} (N_q + 1) \frac{I^{em}[q_+^{em}(k_x)] + I^{em}[q_-^{em}(k_x)]}{\sqrt{(\hbar k_x^2)/(2m^*\omega) - I}}, \tag{2}$$

$$W_{ph}^{abs}(k_x) = \frac{\alpha}{2} \frac{\omega}{\pi} N_q \frac{I^{abs}[q_+^{abs}(k_x)] + I^{abs}[q_-^{abs}(k_x)]}{\sqrt{(\hbar k_x^2)/(2m^*\omega) + I}}, \tag{3}$$

where α is the coupling constant of the electron–phonon interaction, ω is the frequency of a polar optical phonon, and N_q is the number of phonons at thermodynamic equilibrium. The explicit form of the integrals I^{em} and I^{abs} is given in Ref. 8. In formulas (2) and (3) ''em'' refers to a phonon emission process and ''abs'' refers to a phonon absorption process.

The intensity of scattering by a distant charged impurity was calculated using the formula[9]

$$W_l(k_x) = \frac{N_l\, m^* e^4}{4\pi^2 \hbar^3 \varepsilon^2 \varepsilon_0^2 k_x} K^2 \left(2 d k_x \sin\frac{\vartheta}{2} \right), \tag{4}$$

where N_l is the impurity concentration per unit length of the conductor, e is the electron charge, ε and ε_0 are the permittivities of GaAs and vacuum, K is the modified Bessel function of the second kind, d is the distance between the impurity center and the origin, positioned at the center of the square cross section of the wire, and ϑ is the scattering angle.

The final state of the electron after scattering by this mechanism was determined with the assumption that in the strictly one-dimensional case, the electron can only move forward or backward, so that the scattering angle ϑ between the initial k_x and final k_x' wave vectors is either 0° or 180°. To simplify the calculations we used a step-function approximation to the function $K(2dk_x)$ for $dk_x \leq 1$ and the approximation $K(2dk_x) = 0.5\sqrt{\pi/(dk_x)}\exp(-2dk_x)$ for $dk_x > 1$. It was assumed that $K(0)$ has a final value of 4.

The intensity of scattering by surface inhomogeneities was calculated from the formula[10]

$$W_{sr}(k_x) = \frac{2\pi^{9/2}\Lambda\Delta^2\hbar}{m^* L^6 k_x \exp\{k_x^2\Lambda^2\sin^2(\vartheta/2)\}}, \tag{5}$$
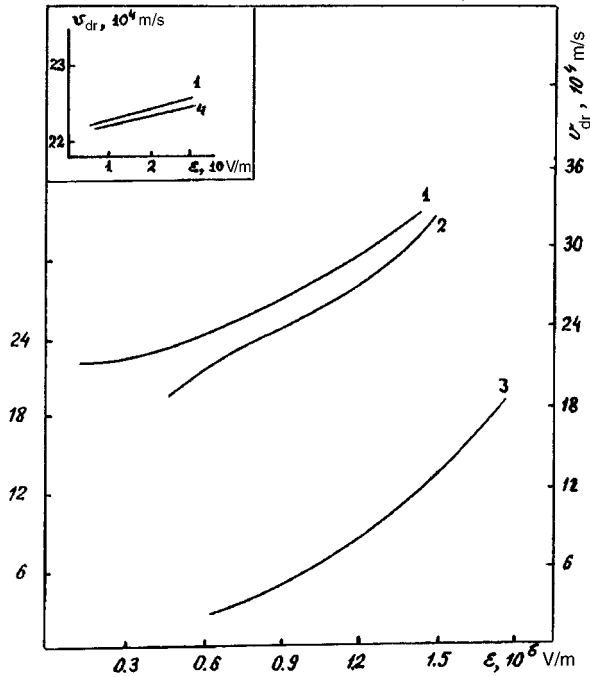
FIG. 1. Average electron drift velocity versus electric field strength: $d=10$ nm, $\Lambda=20$ nm, $\Delta=0.283$ nm, $N_i=10^{-7}$ m^{-1}, electron concentration $n_e=10^{-7}$ m^{-1}, and $L=3L_0=\sqrt{\hbar/(2m^*\omega)}$; data obtained for $L=L_0$ shown in inset.
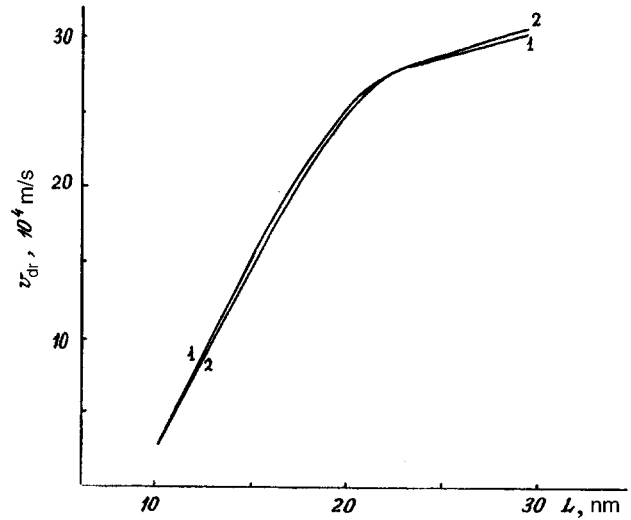

FIG. 2. Average electron drift velocity versus side length of wire cross section: $d=10$ nm, $\Lambda=20$ nm, $\Delta=0.283$ nm, $N_i=10^{-7}$ m^{-1}, electron concentration $n_e=10^{-7}$ m^{-1}, and $\varepsilon=10^6$ V/m.

where Λ and Δ are the correlation length and the amplitude of the inhomogeneities. Here, as for impurity scattering, the angle ϑ is 0° for forward scattering and 180° for backscattering.

Figure 1 gives the average electron drift velocity v_{dr} as a function of the electric field strength calculated assuming only one scattering mechanism — by polar optical phonons (curve 1), two mechanisms — by polar optical phonons and impurity ions (curve 2)—and all three scattering mechanisms (curve 3). For comparison with the results of Ref. 7, Fig 1 (inset) also gives the curve $v_{dr}(\varepsilon)$ calculated at the same temperature $T=30$ K and for $\varepsilon<3\times10^5$ V/m (curve 4). The fact that curves 1 and 4 are almost the same in the range of fields between 1×10^5 and 3×10^5 V/m indicates that the calculations performed for these conditions in Ref. 7 and in the present study are adequate.

From the behavior of the curves in Fig. 1 it may be concluded that heating of charge carriers accompanied by an appreciable increase in the electron drift velocity begins in fields greater than approximately 5×10^5 V/m. It is also easy to see that scattering by surface inhomogeneities significantly influences v_{dr} in this range.

Figure 2 shows the electron drift velocity as a function of the side length L of the square cross section of the wire for two temperatures, $T=4.2$ and 77 K (curves 1 and 2, respectively), calculated assuming all three types of scattering. It

can be seen that the drift velocity increases with increasing L. This can be explained by a considerable drop in the intensity of scattering by surface inhomogeneities and also by a decrease in the intensity of scattering by polar phonons. The behavior of the curves also indicates that under conditions when the electrical quantum limit is attained, the electron drift velocity is essentially independent of the crystal temperature.

The Monte Carlo method has thus been used to calculate the drift velocity of one-dimensional electrons in the quantum well of a GaAs quantum wire at the electrical quantum limit. The results suggest that in this structure the electrons begin to undergo significant heating at electric fields higher than 5×10^5 V/cm. It has also been shown that under the conditions of the model approximations and assumptions in fields exceeding 5×10^5 V/m, the drift velocity is mainly influenced by scattering by polar optical phonons and surface inhomogeneities.

[1] W. Fawcett, A. D. Boardman, and S. Swain, J. Phys. Chem. Solids **31**, 1963 (1970).
[2] K. Yokoyama and K. Hess, Phys. Rev. B **33**, 5595 (1986).
[3] V. M. Borzdov, V. M. Vrubel', O. G. Zhevnyak, and F. F. Komarov, Pis'ma Zh. Tekh. Fiz. **21**(7), 69 (1995) [Tech. Phys. Lett. **21**, 272 (1995)].
[4] S. Briggs and J. P. Leburton, Phys. Rev. B **38**, 8163 (1988).
[5] S. Briggs and J. P. Leburton, Phys. Rev. B **43**, 4785 (1991).
[6] R. Mickevicius, V. V. Mitin, K. W. Kim, and M. A. Stroscio, Semicond. Sci. Technol. B **7**, 299 (1992).
[7] A. Ghosal, D. Chattopadhyay, and A. Bhattacharyya, J. Appl. Phys. **59**, 2511 (1986).
[8] J. P. Leburton, J. Appl. Phys. **56**, 2851 (1984).
[9] H. Sakaki, Jpn. J. Appl. Phys. **19**, L735 (1980).
[10] J. Motohisa and H. Sakaki, Appl. Phys. Lett. **60**, 1315 (1992).

Translated by R. M. Durham